



# Investigations of the structural, dielectric, and piezoelectric properties of MAPbI<sub>3</sub> hybrid perovskites single crystals

Weiwei Li

## ► To cite this version:

Weiwei Li. Investigations of the structural, dielectric, and piezoelectric properties of MAPbI<sub>3</sub> hybrid perovskites single crystals. Materials. Le Mans Université; Institute of ceramics (Shanghai, Chine), 2021. English. NNT : 2021LEMA1017 . tel-03279586

**HAL Id: tel-03279586**

**<https://theses.hal.science/tel-03279586>**

Submitted on 6 Jul 2021

**HAL** is a multi-disciplinary open access archive for the deposit and dissemination of scientific research documents, whether they are published or not. The documents may come from teaching and research institutions in France or abroad, or from public or private research centers.

L'archive ouverte pluridisciplinaire **HAL**, est destinée au dépôt et à la diffusion de documents scientifiques de niveau recherche, publiés ou non, émanant des établissements d'enseignement et de recherche français ou étrangers, des laboratoires publics ou privés.

# THESE DE DOCTORAT DE

LE MANS UNIVERSITE  
COMUE UNIVERSITE BRETAGNE LOIRE

ECOLE DOCTORALE N° 596  
*Matière, Molécules, Matériaux*  
Spécialité : **PHYSIQUE**

**Weiwei LI**

**« Investigations of the structural, dielectric, and piezoelectric properties of MAPbI<sub>3</sub> hybrid perovskites single crystals »**

Thèse présentée et soutenue à Shanghai le 26 Mai 2021  
Unité de recherche : IMMM-UMR CNRS et SHANGHAI INSTITUTE OF CERAMICS  
Thèse N° : 2021LEMA1017

## Rapporteurs avant soutenance :

Benoit GUIFFARD  
Jingrong CHENG

Professeur, CNRS-IETR, Université de Nantes, France  
Professeure, Université de Shanghai, Chine

## Composition du Jury :

Président : Jingrong CHENG

Professeure, Université de Shanghai, Chine

Examineurs : Jinjin ZHAO  
Kin Wing KWOK  
Jens Dittmer  
Chul Hong Park

Professeure, Shijiazhuang Tiedao University, Chine  
Professeur, Université Polytechnique de Hong Kong  
Professeur, IMMM-CNRS Le Mans Université  
Professeur, Université Nationale de Pusan, Corée du Sud  
Professeur, Institut de Céramiques de Shanghai  
Professeur, IMMM-CNRS Le Mans Université

Dir. de thèse : Guorong LI  
Dir. de thèse : Abdel Hadi KASSIBA

**Title : Investigations of the structural, dielectric, and piezoelectric properties of MAPbI<sub>3</sub> hybrid perovskites single crystals**

**Keywords :** MAPbI<sub>3</sub>, Pre-transitional effects, Dielectric properties, Electrostriction, Piezoelectricity, Ferroelectricity, Photocatalysis

**Abstract :** The hybrid perovskite MAPbI<sub>3</sub> possesses excellent optoelectronic properties and their optimization and applications requires in depth understanding of the material structure and fundamental physical properties. This thesis investigates the structure and main properties of MAPbI<sub>3</sub> through the following approaches: (1) Study of the dielectric properties of single crystals to point out the relationship between ion migration and giant dielectric effects. Both methylamine MA<sup>+</sup> cations and iodide I<sup>-</sup> anions are mobile species which contribute to the dielectric constant strength. This effect was established and explained by the abnormal change of the dielectric constant of MAPbI<sub>3</sub> under illumination. Through the study of the thermal variation of the dielectric spectrum, the relationship between the orientation of MA<sup>+</sup> ions and the temperature is clarified as also was inferred from the influence of non-polar ions Cs<sup>+</sup> on the ion orientation of MA<sup>+</sup>. The evolution of the dielectric constant was also analyzed close to the critical temperatures of the phase transitions in MAPbI<sub>3</sub>.

This study rules out the involvement of ferroelectric-paraelectric phase at the tetragonal-cubic phase change. (2) The effects of AC and DC poling on the electrostriction and piezoelectric properties of MAPbI<sub>3</sub> were investigated and point out the role of poling in the strength of the phenomena. The investigations of electrostrictive and piezoelectric effects was conducted with and without poling using DC or AC. The different experiments point out the promising applications of MAPbI<sub>3</sub> in actuators, energy harvesting and integrated MEMS systems. (3) The ferroelectric properties of MAPbI<sub>3</sub> were studied by two different methods: ferroelectric hysteresis loop and PFM. For the structural features, high-resolution XRD was used to characterize the phase transition between the tetragonal and cubic phase in MAPbI<sub>3</sub>; (4) MAPbI<sub>3</sub> and MAPbI<sub>3</sub>/TiO<sub>2</sub> powders were prepared by the anti-solvent method, and the effect of MAPbI<sub>3</sub> on the photocatalytic reactions to oxidize Benzaldehyde and Benzyl alcohol.

**Titre: Etudes de propriétés structurales, diélectriques, et piézoélectrique de monocristaux pérovskites hybrides**

**Mots Clés :** MAPbI<sub>3</sub>, Effets pré-transitionnels, Propriétés diélectriques Electrostriction, Piézoélectricité, Ferroélectricité, Photocatalyse

**Résumé :** La pérovskite hybride MAPbI<sub>3</sub> possède d'excellentes propriétés optoélectroniques et leurs optimisations nécessitent une compréhension approfondie de la structure des matériaux et leurs propriétés physiques fondamentales (diélectriques, piézoélectriques, ferroélectriques, conductivité, transitions de phase structurales). Cette thèse s'inscrit dans ce contexte et comporte les contributions suivantes : (1) Étude des propriétés diélectriques des monocristaux MAPbI<sub>3</sub> pour corréler la migration des ions et les effets diélectriques avec des fortes valeurs. Ce comportement est lié aux cations MA<sup>+</sup> de méthylamine et anions iodure I<sup>-</sup> qui sont des espèces mobiles contribuant à la forte constante diélectrique. L'étude de la variation thermique du spectre diélectrique, la relation entre l'orientation des ions MA<sup>+</sup> et la température est clarifiée, comme on l'a également déduit de l'influence des ions Cs<sup>+</sup> sur l'orientation ionique de MA<sup>+</sup>. L'évolution de la constante diélectrique dans MAPbI<sub>3</sub> a aussi été analysée au voisinage des transitions de phases structurales. Cette étude exclut l'existence d'une transition de phase de type ferroélectrique- paraélectrique susceptible de se manifester à la transition de phase tétragonale-cubique.

(2) Les effets du poling électrique (AC, DC) sur les propriétés d'électrostriction et piézoélectrique de MAPbI<sub>3</sub> ont été étudiés incluant l'effet de la fréquence du signal du poling. Les résultats sur les paramètres d'électrostriction et piézoélectriques peuvent être optimisés pour des applications prometteuses de MAPbI<sub>3</sub> dans des actionneurs ou dans les systèmes intégrés MEMS. (3) Les propriétés ferroélectriques de MAPbI<sub>3</sub> ont été étudiées par deux méthodes différentes : boucles d'hystérésis ferroélectrique et la microscopie par force piézoélectrique (PFM). Pour les caractéristiques structurales, des études par diffraction des rayons X haute résolution ont été menées pour caractériser la transition de phase entre la phase tétragonale et cubique dans MAPbI<sub>3</sub>. Des effets pré-transitionnels ont été démontrés à l'approche de la transition tétragonale-cubique; (4) Enfin, les poudres MAPbI<sub>3</sub> et MAPbI<sub>3</sub>/TiO<sub>2</sub> ont été mises en œuvres dans des réactions photocatalytiques. L'objectif étant de tester l'efficacité de la photoactivité de ces systèmes dans les réactions photocatalytiques dédiées à l'oxydation de groupes organiques tels que le benzaldéhyde et l'alcool de Benzyl.

## **Acknowledgement**

My heartfelt thanks go out to my supervisors of Prof. Guorong Li and Prof. Abdelhadi Kassiba, who give me the opportunity for further study. I am appreciated for their outstanding scientific supervision, kindly support, and enthusiastic encouragement in the past years. It is my honor to be their student.

I would like to acknowledge Prof. Liaoying Zheng, Prof. Jiangtao Zeng, Prof. Huarong Zeng, Associate Prof. Zhenyong Man, Associate Prof. Kunyu Zhao, Associate Prof. Tian Tian, Mr. Xuezheng Ruan, Mr. Caiming Zhong, Ms. Xue Shi, Ms. Dan Wang, Ms. Guolan Zhou, Mr. Shengye Zhang for kindly assistance during my scientific study.

I sincerely appreciate Kunqi Xu, Dan Zhang, Qiwei Lou, Xiang Huang, Qianying Sun, Jian Zou, Xiao Luo, Jing Shang, Guli Pengjiang, Zhuo Yu, Wei Li, Xiang Xia, Siyu Huang, Bingjie Teng, Chunbo Li, Xi Chen, Haoxian Chen, Aihua Liang, Dingwei Liu, Lamei Ke, Ying Shi, Wentong Du, Weiwei Yang.

I would like to acknowledge Prof. Alain Bulou, Prof. Alain Gibaud, Frederic Amiar, Sandy, Geoffroy Martin who give me kindly help during France

Many thanks to my warm-hearted friends Yuwen Meng, Yuzhu Long, Shengyu Tang, Xiaoyang Yu, Drisya who give me kindly help during France.

My warm thanks to the administrative offices in the department of graduate student, I acknowledge Zhiwei Zhou, Caifei Lu, Xinhong Lu, Xueying Zhao.

Lastly, I sincerely appreciate my parents and brother for their selfless love and great confidence in me through all these years.



### List of Publications

1. Weiwei Li; Jiangtao Zeng; Liaoying Zheng; Huarong Zeng; Chunbo Li; Abdelhadi Kassiba; Chulhong Park; Guorong Li, Apparent ferroelectric-like and dielectric properties of  $\text{CH}_3\text{NH}_3\text{PbI}_3$  synthesized in ambient air. *Ferroelectrics* **2019**, 553 (1), 95-102.
2. Weiwei Li; Zhenyong Man; Jiangtao Zeng; Liaoying Zheng; Guorong Li; Abdelhadi Kassiba, Relationship of Giant Dielectric Constant and Ion Migration in  $\text{CH}_3\text{NH}_3\text{PbI}_3$  Single Crystal Using Dielectric Spectroscopy. *The Journal of Physical Chemistry C* **2020**, 124 (24), 13348-13355.
3. Weiwei Li; Zhenyong Man; Jiangtao Zeng; Liaoying Zheng; Huarong Zeng; Kunyu Zhao; Guorong Li; Abdelhadi Kassiba, Poling effect on the electrostrictive and piezoelectric response in  $\text{CH}_3\text{NH}_3\text{PbI}_3$  single crystals. *Appl Phys Lett* **2021**, 118 (15), 151905.
4. Xiang Huang; Weiwei Li; Jiangtao Zeng; Liaoying Zheng; Zhenyong Man; Guorong Li, The grain size effect in dielectric diffusion and electrical conduction of PZnTe-PZT ceramics. *Physica B: Condensed Matter* **2019**, 560, 16-22.



## **Participation in the conferences**

### **Oral communications:**

[1] Relationship of Giant Dielectric Constant and Ionic Migration in  $\text{CH}_3\text{NH}_3\text{PbI}_3$  Single Crystal Using Impedance Spectroscopy. 21<sup>st</sup> Graduate English Academic Exchange Conference Shanghai, 11/17/2020

[2] Poling effect on the electrostrictive and piezoelectric response in  $\text{CH}_3\text{NH}_3\text{PbI}_3$  single crystals. 2021 International Workshop on New Domain Technology of Ferroelectric Materials and Their Applications. Online zoom. 01/23/2021





**Abstract**

The hybrid perovskite MAPbI<sub>3</sub> possesses excellent optoelectronic properties and their optimization and applications require in depth understanding of the material structure and fundamental physical properties. This thesis investigates the structure and main properties of MAPbI<sub>3</sub> through the following approaches:

(1) Study of the dielectric properties of single crystals to point out the relationship between ion migration and giant dielectric effects. Both methylamine MA<sup>+</sup> cations and iodide I<sup>-</sup> anions are mobile species which contribute to the dielectric constant strength. This effect was established and explained by the abnormal change of the dielectric constant of MAPbI<sub>3</sub> under illumination. Through the study of the thermal variation of the dielectric spectrum, the relationship between the orientation of MA<sup>+</sup> ions and the temperature is clarified as also was inferred from the influence of non-polar ions Cs<sup>+</sup> on the ion orientation of MA<sup>+</sup>. The evolution of the dielectric constant was also analyzed close to the critical temperatures of the phase transitions in MAPbI<sub>3</sub>. This study rules out the involvement of ferroelectric-paraelectric phase at the tetragonal-cubic phase change.

(2) The effects of AC and DC poling on the electrostriction and piezoelectric properties of MAPbI<sub>3</sub> were investigated and point out the role of poling in the strength of the phenomena. The investigations of electrostrictive and piezoelectric effects was conducted with and without poling using DC or AC. The different experiments point out the promising applications of MAPbI<sub>3</sub> in actuators, energy harvesting and integrated MEMS systems.

(3) The ferroelectric properties of MAPbI<sub>3</sub> were studied by two different methods: ferroelectric hysteresis loop and PFM. For the structural features, high-resolution XRD was used to characterize the phase transition between the tetragonal and cubic phase in MAPbI<sub>3</sub>;

(4) MAPbI<sub>3</sub> and MAPbI<sub>3</sub>/TiO<sub>2</sub> powders were prepared by the anti-solvent method, and the effect of MAPbI<sub>3</sub> on the photocatalytic reactions to oxidize Benzaldehyde and Benzyl alcohol.

**Key Words:** MAPbI<sub>3</sub>, Pre-transitional effects, Dielectric proprieties, Electrostriction, Piezoelectricity, Ferroelectricity, Photocatalysis

## Résumé

La pérovskite hybride MAPbI<sub>3</sub> possède d'excellentes propriétés optoélectroniques et leurs optimisations nécessitent une compréhension approfondie de la structure des matériaux et leurs propriétés physiques fondamentales (diélectriques, piézoélectriques, ferroélectriques, conductivité, transitions de phase structurales). Cette thèse s'inscrit dans ce contexte et comporte les contributions suivantes:

(1) Étude des propriétés diélectriques des monocristaux MAPbI<sub>3</sub> pour corrélérer la migration des ions et les effets diélectriques avec des fortes valeurs. Ce comportement est lié aux cations MA<sup>+</sup> de méthylamine et anions iodure I<sup>-</sup> qui sont des espèces mobiles contribuant à la forte constante diélectrique. L'étude de la variation thermique du spectre diélectrique, la relation entre l'orientation des ions MA<sup>+</sup> et la température est clarifiée, comme on l'a également déduit de l'influence des ions Cs<sup>+</sup> sur l'orientation ionique de MA<sup>+</sup>. L'évolution de la constante diélectrique dans MAPbI<sub>3</sub> a aussi été analysée au voisinage des transitions de phases structurales. Cette étude exclut l'existence d'une transition de phase de type ferroélectrique- paraélectrique susceptible de se manifester à la transition de phase tétragonale-cubique.

(2) Les effets du poling électrique (AC, DC) sur les propriétés d'électrostriction et piezoelectrique de MAPbI<sub>3</sub> ont été étudiés incluant l'effet de la fréquence du signal du poling. Les résultats sur les paramètres d'électrostriction et piézoélectriques peuvent être optimisés pour des applications prometteuses de MAPbI<sub>3</sub> dans des actionneurs ou dans les systèmes intégrés MEMS.

(3) Les propriétés ferroélectriques de MAPbI<sub>3</sub> ont été étudiées par deux méthodes différentes : boucles d'hystérésis ferroélectrique et la microscopie par force piézoélectrique (PFM). Pour les caractéristiques structurales, des études par diffraction des rayons X haute résolution ont été menées pour caractériser la transition de phase entre la phase tétragonale et cubique dans MAPbI<sub>3</sub>. Des effets pré-transitionnels ont été démontrés à l'approche de la transition tétragonale-cubique;

(4) Enfin, les poudres MAPbI<sub>3</sub> et MAPbI<sub>3</sub>/TiO<sub>2</sub> ont été mises en œuvres dans des réactions photocatalytiques. L'objectif étant de tester l'efficacité de la photoactivité de

ces systèmes dans les réactions photocatalytiques dédiées à l'oxydation de groupes organiques tels que le benzaldéhyde et l'alcool de Benzyl.

**Mots Clés :** MAPbI<sub>3</sub>, Effets pré-transitionnels, Propriétés diélectriques, Electrostriction, Piezoélectricité, Ferroélectricité , Photocatalys

## Contents

Chapter 1 overview on MAPbI <sub>3</sub> : structure and properties .....	1
1.1 Introduction .....	1
1.2 The structure and the optical properties of MAPbI <sub>3</sub> .....	2
1.2.1 The structure of MAPbI <sub>3</sub> .....	2
1.2.2 Optical properties and the electronic structure of MAPbI <sub>3</sub> .....	4
1.3 Ion migration and its effect on performance in MAPbI <sub>3</sub> .....	5
1.3.1 Ion migration and defects in MAPbI <sub>3</sub> .....	5
1.3.2 The effect of ion migration and defects on properties .....	7
1.4 Research process on the dielectric properties of MAPbI <sub>3</sub> .....	9
1.5 Progress in the study of the electrostrictive and piezoelectric response of MAPbI <sub>3</sub> .....	14
1.5.1 Electristrictive effect of MAPbI <sub>3</sub> and its research progress .....	14
1.5.2 Piezoelectricity of MAPbI <sub>3</sub> and its research progress .....	18
1.6 Ferroelectric properties of MAPbI <sub>3</sub> and its research progress .....	20
1.7 Phase transition from tetragonal to cubic phase of MAPbI <sub>3</sub> .....	25
1.8 Application of MAPbI <sub>3</sub> in photocatalysis .....	26
Chapter 2 Experimental process and test equipment .....	29
2.1 Sample preparation .....	29
2.1.1 Raw materials .....	29
2.1.2 Process of preparing single crystals by inversion temperature crystallization method .....	29
2.1.3 Powder preparation .....	30
2.1.4 Films preparation .....	30
2.2 Characterization of sample structure and properties .....	31
2.2.1 Material phase analysis .....	31
2.2.2 Microstructure analysis .....	31
2.2.3 Raman spectroscopy .....	31
2.2.4 Electrical performance test .....	31
2.2.5 Piezoresponse force microscopy measurement .....	34

2.2.6 Optical properties measurement.....	35
2.2.7 Photocatalytic oxidation efficiency measurement.....	35
Chapter 3 Dielectric properties of MAPbI <sub>3</sub> .....	37
3.1 Introduction.....	37
3.2 Sample preparation and characterization .....	38
3.3 The relationship between the dielectric properties of MAPbI <sub>3</sub> single crystal and ion migration.....	38
3.3.1 XRD pattern of MAPbI <sub>3</sub> single crystals .....	38
3.3.2 The giant dielectric constant of MAPbI <sub>3</sub> single crystal.....	39
3.3.3 The reorientation of MA <sup>+</sup> .....	43
3.3.4 Ac conductivity of MAPbI <sub>3</sub> single crystals .....	44
3.3.5 The Influence of illumination on the Dielectric Properties of MAPbI <sub>3</sub> Single Crystals .....	49
3.3.6 Dielectric temperature spectrum of MAPbI <sub>3</sub> .....	51
3.4 Effect of Cs <sup>+</sup> doping on the dielectric properties of MAPbI <sub>3</sub> .....	53
3.4.1 Effect of Cs <sup>+</sup> doping on the structure of MAPbI <sub>3</sub> .....	53
3.4.2 Effect of Cs <sup>+</sup> doping on the optical properties of MAPbI <sub>3</sub> .....	54
3.4.3 Effect of Cs <sup>+</sup> doping on the dielectric properties of MAPbI <sub>3</sub> .....	55
3.5 Conclusion .....	56
Chapter 4 Tetragonal to cubic phase transition of MAPbI <sub>3</sub> .....	59
4.1. Introduction.....	59
4.2 tetragonal to cubic phase transition of MAPbI <sub>3</sub> .....	59
4.3 Pretransitional effect of MAPbI <sub>3</sub> single crystal.....	65
4.4 Raman spectroscopy analysis of tetragonal to cubic phase transition.....	67
4.5 Conclusions.....	68
Chapter 5 Poling effect on the electrostrictive and piezoelectric response of MAPbI <sub>3</sub> single crystals.....	71
5.1 Introduction.....	71
5.2 Sample preparation and characterization .....	73
5.3 The piezoelectricity of Quartz.....	73

5.4 Electrostriction and piezoelectricity of MAPbI <sub>3</sub> single crystals.....	74
5.5 Poling effect on the electrostrictive response in MAPbI <sub>3</sub> single crystals.....	76
5.6 Poling effect on the piezoelectric response in MAPbI <sub>3</sub> single crystals .....	77
5.7 Defects induced by poling.....	79
5.8 The effect of ac poling frequency on electrostrictive and piezoelectric response of MAPbI <sub>3</sub> single crystals.....	82
5.9 Conclusion .....	83
Chapter 6 Ferroelectric properties of MAPbI <sub>3</sub> .....	85
6.1 Introduction.....	85
6.2 Sample preparation and measurement.....	85
6.3 Ferroelectric properties of MAPbI <sub>3</sub> .....	86
6.3.1 The effect of excessive CH <sub>3</sub> NH <sub>3</sub> I on the phase of MAPbI <sub>3</sub> .....	86
6.3.2 Ferroelectric and dielectric properties of the MAPbI <sub>3</sub> pellets.....	86
6.3.3 Analysis of the surface morphology and ferroelectric properties of the MAPbI <sub>3</sub> film .....	88
6.3.4 Ferroelectric properties of MAPbI <sub>3</sub> crystal .....	90
6.4 Conclusion .....	91
Chapter 7 Exploration of MAPbI <sub>3</sub> Photocatalytic Properties .....	93
7.1 Introduction.....	93
7.2 Sample preparation and characterization .....	94
7.3 XRD pattern of MAPbI <sub>3</sub> /TiO <sub>2</sub> .....	94
7.4 Optical properties of MAPbI <sub>3</sub> /TiO <sub>2</sub> composite .....	95
7.5 Microstructure and EDS spectrum of MAPbI <sub>3</sub> /TiO <sub>2</sub> .....	96
7.6 Photocatalytic oxidation properties of MAPbI <sub>3</sub> /TiO <sub>2</sub> .....	97
7.7 Conclusions.....	100
Chapter 8 General Conclusion and Perspective.....	101
8.1. conclusion .....	101
8.2 Perspective .....	104
Bibliography .....	107
List of Figures .....	127



## Chapter 1 Overview on MAPbI<sub>3</sub>: structure and properties

### 1.1 Introduction

Energy has always been an important driving force for the development of human civilization, and the rapid development of science and technology have led to a sharp increase in the consumption of fossil energy leading to an energy crisis. People pay more attention to the environmental problems caused by the energy crisis and the burning of the fossil energy. It is imperative to expand renewable and environmentally friendly new energy sources. As a result, the development and research of renewable energy such as hydropower, wind power, solar energy, biomass energy, geothermal energy and tidal energy come into being. Among these new energy sources, solar energy is inexhaustible. The energy that reaches the earth every year is equivalent to the energy released by the burning of 130 trillion tons of coal. At the same time, solar energy is also the cleanest energy source, and its accessibility is very important to the sustainable development of society. Therefore, as an important energy supply for the mankind in the future, great hopes are placed on solar cells. The development of new low-cost, high-efficiency solar cells has become a research hotspot in recent years.

From the material's features, solar cells can be divided into the following categories: (1) The first-generation silicon-based solar cells, which mainly refer to solar cells based on monocrystalline silicon, polycrystalline silicon and amorphous silicon<sup>[1-3]</sup>; (2) The second-generation multi-element compounds thin-film solar cells, mainly including GaAs, InP, CIGS, CdTe solar cell<sup>[4-6]</sup>; (3) The third generation of solar cells, mainly including perovskite solar cells, dye-sensitized solar cells, organic solar cells, quantum dot solar cells<sup>[7-9]</sup>. Among them, the perovskite solar cells have attracted the attention of many researchers because of its simple production process and the low cost of the overall technology. Organic-inorganic hybrid perovskites (OIHP) were synthesized by Dieter Weber in 1978 for the first time<sup>[10-11]</sup>. Although there have been some studies on the OIHP since then, they have not attracted widespread attention. Until 2009, since Akihiro Kojima<sup>[12]</sup> first applied CH<sub>3</sub>NH<sub>3</sub>PbI<sub>3</sub> (MAPbI<sub>3</sub>) as an absorber layer to dye-sensitized solar cells, perovskite solar cells have attracted more attention. In

recent years, the efficiency of perovskite solar cells has reached 25.5% from the initial 3.8%<sup>[13]</sup>, showing a rapid development. The efficiency of tandem solar cells combining with silicon-based materials is even as high as 29.5%<sup>[14]</sup>.

In addition to the perovskite solar cells, hybrid perovskites are also widely used in photodetectors<sup>[15-16]</sup>, lasers<sup>[17-18]</sup>, LED<sup>[19-20]</sup> and photocatalytic hydrogen production<sup>[21]</sup>. The current research on hybrid perovskites is mainly divided into two aspects: (1) the improvement of the efficiency of photoelectric devices from the perspectives of composition, preparation process and device structure, (2) focusing on the structure and properties of the semiconducting hybrid perovskite and explaining the reason of the outstanding photoelectric properties related to the charge transport or in counterpart the structural instabilities. Elucidating the behavior of some key physical features such as dielectric, ferroelectric, electrostrictive, and piezoelectric properties, and point out the direction for future developments. The present work is devoted to some of these key directions.

## 1.2 The structure and the optical properties of MAPbI<sub>3</sub>

### 1.2.1 The structure of MAPbI<sub>3</sub>

MAPbI<sub>3</sub> has a typical perovskite structure as shown in Figure 1.1, where MA<sup>+</sup> is located at the vertex position, Pb<sup>2+</sup> stands at the body center position, and I<sup>-</sup> is located at the corners of octahedral environments surrounding the central Pb<sup>2+</sup> ion.

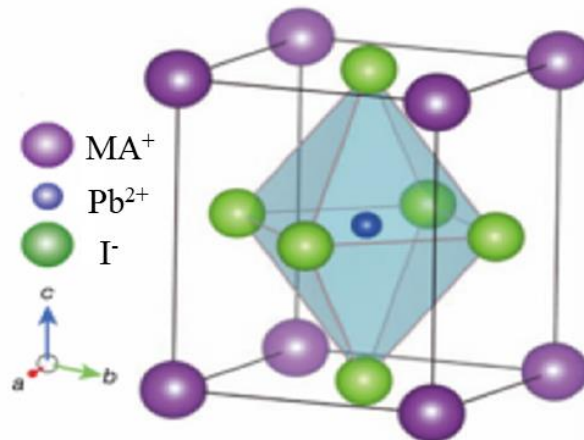


**Figure 1.1** The crystal structure of MAPbI<sub>3</sub>

At room temperature, the structure of MAPbI<sub>3</sub> is a tetragonal phase with the space group I4/mcm and the lattice parameter  $a=8.743 \text{ \AA}$ ,  $c=12.6708 \text{ \AA}$ <sup>[22]</sup>. Above 300 K, the structure is a cubic phase with the space group Pm-3m and the lattice parameter  $c=6.391 \text{ \AA}$ . Below 160 K, the structure became orthorhombic phase with the lattice parameters  $a=8.8363 \text{ \AA}$ ,  $b=12.5804 \text{ \AA}$ ,  $c=8.5551 \text{ \AA}$ <sup>[23]</sup>. Since MA<sup>+</sup> has a dipole moment with a symmetry of C<sub>3v</sub>, the orientation of MA<sup>+</sup> will have an influence on the crystal structure. The relationship between the orientation of MA<sup>+</sup> and the structure at different temperatures is shown in Figure 1.2. According to the results of neutron diffraction, it is impossible for MA<sup>+</sup> with a low symmetry to be placed in an octahedron with m-3m (O<sub>h</sub>) high symmetry without introducing disorder. Therefore, the MA<sup>+</sup> will have six equivalent orientations in the cubic phase. The C-N bond is along <100> direction. Since MA<sup>+</sup> has three-fold axes, the octahedron has four-fold axes. Therefore, MA<sup>+</sup> will exhibit four-fold disordered rotation along these axes at high temperature, and it will have 24 possible orientations with a complete disorder. For the tetragonal phase structure, the low symmetry of C<sub>3v</sub> also cannot meet the requirement of  $\bar{4}2/m$  (D<sub>2d</sub>). In this case, the MA<sup>+</sup> has eight possible orientations with a partial disorder. For the orthorhombic phase, since the symmetry of the crystal structure is further reduced, the MA<sup>+</sup> does not need to be disordered to satisfy the symmetry and shows the anti-parallel arrangement<sup>[24-25]</sup>.

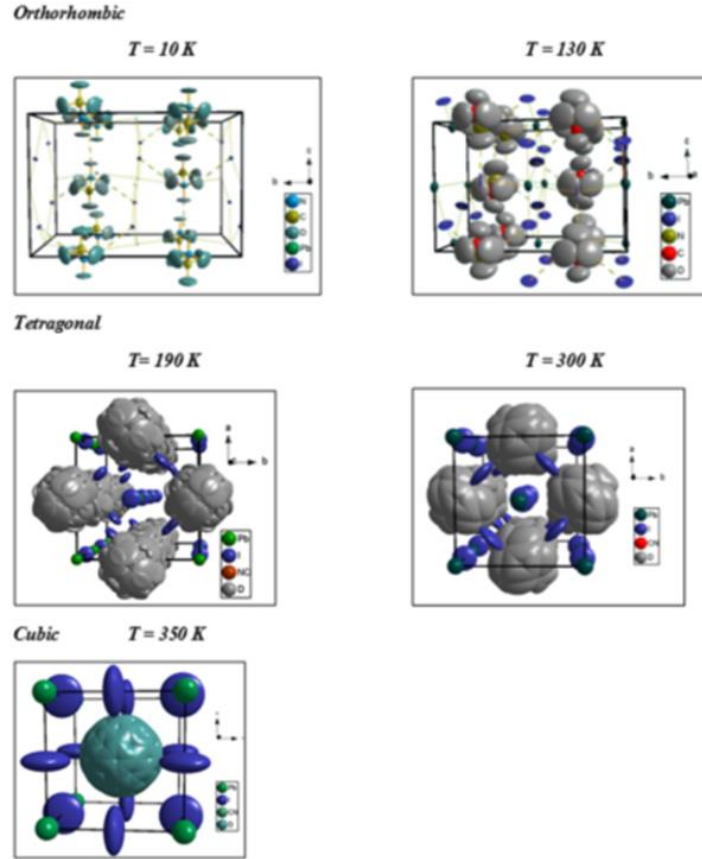


**Figure 1.2** Structures of MAPbI<sub>3</sub> at five temperatures based upon refinement of neutron powder diffraction data<sup>[24]</sup>

### 1.2.2 Optical properties and electronic structure of MAPbI<sub>3</sub>

MAPbI<sub>3</sub> is a direct band gap semiconductor with the band gap of about 1.55 eV<sup>[26]</sup>. Figure 1.3 shows the theoretical calculation results of the density of state (DOS) of MAPbI<sub>3</sub>. The results show that the band gap is attributed to the Pb 6s and I 5p orbitals. Although MA<sup>+</sup> does not directly contribute to the band gap, the orientation of MA<sup>+</sup> will have an influence on the DOS of MAPbI<sub>3</sub>.

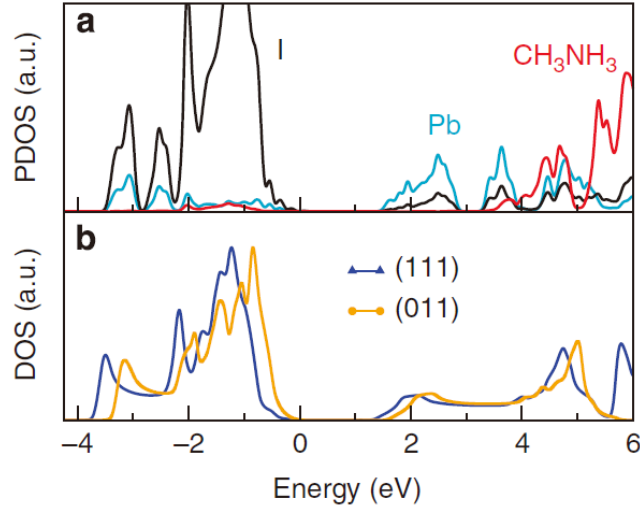


**Figure 1.3** Electronic properties of the cubic phase

MAPbI<sub>3</sub>. (a) Density of states (DOS) for the case of the (111)-oriented molecule (b) DOS as a function of the chemical potential for the molecule oriented along the (111) and (011) directions are displayed<sup>[27]</sup>.

The carrier lifetime of MAPbI<sub>3</sub> is about 0.1-1  $\mu$ s, the carrier mobility is as high as 100 cm<sup>2</sup>V<sup>-1</sup>s<sup>-1</sup>, the exciton activation energy is only 45 meV. The optical absorption of MAPbI<sub>3</sub> occurs from the near Infra-red, visible to ultraviolet light with the edge situated at about 800 nm and the light absorption coefficient can reach 10<sup>5</sup> cm<sup>-1</sup>. These excellent electronic and optical performances support the promising applications of MAPbI<sub>3</sub> in optoelectronic devices<sup>[28-29]</sup> or in photoactive processes.

### 1.3 Ion migration and its effect on performance in MAPbI<sub>3</sub>

#### 1.3.1 Ion migration and defects in MAPbI<sub>3</sub>

MAPbI<sub>3</sub> is not only a semiconductor, but also has the characteristics of ion conductors. These ionic motions affect the efficiency of perovskite solar cell<sup>[30-31]</sup>, and bring some difficulties to analyze the mechanism behind some key physical properties<sup>[32-33]</sup>. Although many experiments have confirmed the existence of ion migration<sup>[31, 34]</sup>, the induced effects need to be further studied as function of the nature of the moving ions. Thus, by using the ABO<sub>3</sub> perovskite type oxide as a reference, I<sup>-</sup> is easiest to migrate in MAPbI<sub>3</sub> due to the shortest distance from the nearest I<sup>-</sup> vacancy as shown in figure 1.4 and supported by theoretical calculations. Eames et al.<sup>[35]</sup> calculated

the activation energy of various ions of MAPbI<sub>3</sub>. Among them, I<sup>-</sup> migrating along the I<sup>-</sup> - I<sup>-</sup> edge of the octahedron of PbI<sub>6</sub> has the smallest activation energy about 0.58 eV. MA<sup>+</sup> ions in (100) plane migrate along the <100> direction with a relatively higher barrier at 0.84 eV. For Pb<sup>2+</sup>, the activation energy is as high as 2.31 eV limiting its motion in the host lattice. However, MA<sup>+</sup> groups were the first units to show a migration effect in MAPbI<sub>3</sub>. Using the photothermal induced resonance technique (PTIR), Yuan et al.<sup>[36]</sup> found that MA<sup>+</sup> are redistributed under an applied electric field. As shown in figure 1.4 (c), after 100 s of poling with a small electric field of 1.6 V/μm, MA<sup>+</sup> are depleted from the middle and anode region, and accumulated in the cathode region. The activation energy of ion migration can be derived from the conductivity change of MAPbI<sub>3</sub> at different temperatures. The estimated activation energy value is only 0.36 eV, which is slightly lower than the calculated one. However, Moritz H. Futscher et al.<sup>[37]</sup> studied the activation energy, diffusion coefficient and the concentration of mobile ions by transient capacitance measurements. They found that there were three changes in the capacitance values from low temperatures to high temperatures. The change at low temperature was attributed to the migration of I<sup>-</sup>, while the other two changes were due to the migration of MA<sup>+</sup>. The concentration of moving MA<sup>+</sup> groups is one order of magnitude higher than I<sup>-</sup>, but its diffusion coefficient is one order of magnitude less. For the diffusion process, the migration of ions under electric field is mediated by the movement of defects which indicates that the material has a high defect density. Theoretical calculations have shown that both Pb<sup>2+</sup> vacancies and MA<sup>+</sup> interstitial have small formation energy<sup>[38]</sup>. However, there is no experiment to confirm such statement. The reasons for the large number of defects in the perovskite films are as follow: (1) Rapid crystallization during the thermal evaporation of the films by the spin-coating<sup>[39-40]</sup>; (2) In most case, the ratio of precursors is not conform to the expected stoichiometric<sup>[41-42]</sup>. (3) Theoretical calculations show that the chemical bond in MAPbI<sub>3</sub> is weak and then lower decomposition energy (0.1 eV) will lead to a large number of defects<sup>[43]</sup>.

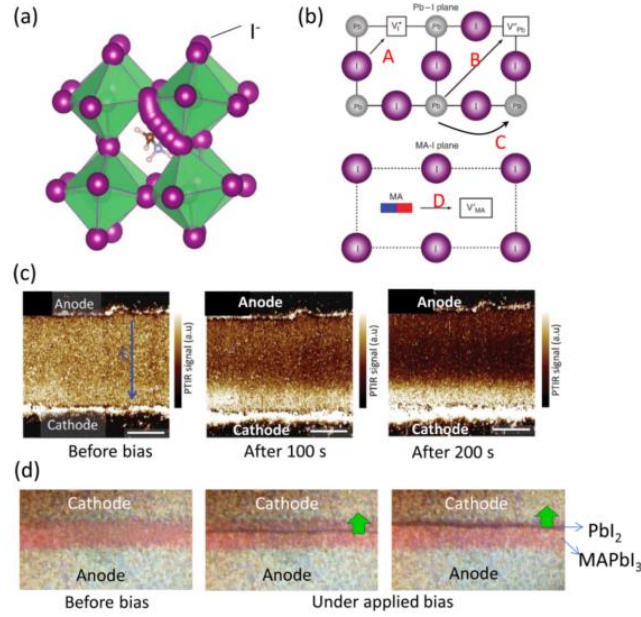


**Figure 1.4** (a) Migration path of I<sup>-</sup> ions along the I<sup>-</sup>-I<sup>-</sup> edge of the PbI<sub>6</sub> octahedron in the MAPbI<sub>3</sub> crystal calculated from density functional theory (DFT) method. (b) Illustration of the migration paths for I<sup>-</sup> ions (A), Pb<sup>2+</sup> ions (B, C), and MA<sup>+</sup> ions (D). (c) PTIR images of the distribution of MA<sup>+</sup> before and after electrical poling for 100 s and 200 s. (d) Optical images of the lateral MAPbI<sub>3</sub> perovskite solar cell with a mobile PbI<sub>2</sub> thread<sup>[44]</sup>

### 1.3.2 The effect of ion's migration and defects on physical features

Due to the existence of ion's migration and defects in MAPbI<sub>3</sub>, it is necessary to consider their effects on the properties of materials and the performance of photoelectric device. Figure 1.5 shows the current-voltage curves of perovskite solar cells under different scanning modes<sup>[43]</sup>. Snaith et al.<sup>[45]</sup> demonstrated that the efficiency of perovskite solar cells is different and presents an hysteresis between the forward bias to open circuit and the one from short circuit to the forward bias. The difference is also related to the scanning rate. The hysteresis phenomena in the perovskite solar cells remains open problem. Initially, It was thought that the hysteresis was related to the grain size and the lack of porous TiO<sub>2</sub> layers<sup>[46]</sup>. Walsh et al.<sup>[47]</sup> claimed that the hysteresis was related to the built-in electric field caused by polarization. Because the ferroelectric materials show similar hysteresis, some authors have suggested the ferroelectricity as an origin for the observed hysteresis<sup>[47-48]</sup>.

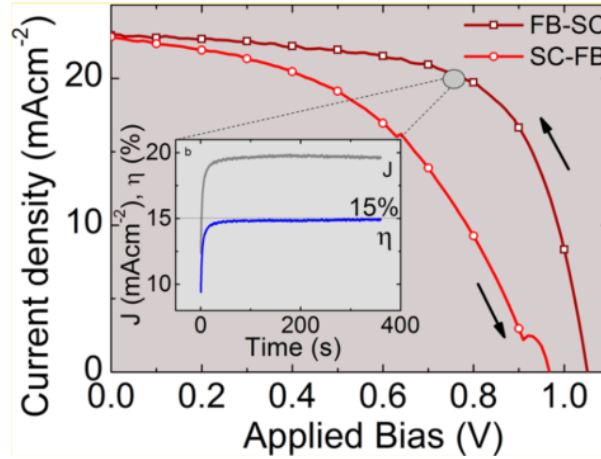


**Figure 1.5** Current–voltage curves of perovskite solar cells, FB-SC represents forward bias to short circuit and SC-FB represents short circuit to forward bias<sup>[43]</sup>

However, an in depth analyses have suggested that the hysteresis phenomena are closely related to ion migration while Meloni et al.<sup>[49]</sup> found that the hysteresis phenomena are a thermally activated process. The activation energy is consistent with the activation energy of ion migration calculated by the DFT theory. Therefore, ion migration is claimed to be the origin of the hysteresis as suggested by Cheng Li et al.<sup>[50]</sup> Electro-absorption spectroscopy shows that the hysteresis is caused by the change of carriers at the interface which also modify the electrical conductivity. Ion migration not only affects the efficiency of solar cells, but also affects the stability of materials. Hoke et al.<sup>[51]</sup> show that MAPbBr<sub>x</sub>I<sub>3-x</sub> films exhibit different phase segregation process under irradiation leading to the appearance of iodine-rich phase and iodine-poor phase. In this case, the phase with a small band gap will act as a recombination center trap and reduce the open circuit voltage, and finally reduce the efficiency of the solar cells. However, ion migration does not necessarily reduce the efficiency of solar cells. Xiao et al.<sup>[52]</sup> found that after electrical poling, ion migration will lead to the formation of p-i-n structure. The photocurrent of this device reached 20.1 mA/cm<sup>2</sup> under a small electric field less than 1 V/μm. This result indicates that ion's migration can modulate the efficiency of optoelectronic devices. Deng et al.<sup>[53]</sup> found that light can also induce a self-doping effect similar to the electrical poling. The study has shown that the open circuit voltage of the non-illuminated device was only 0.6 V, and the efficiency is about 4.3%. However, after irradiation, the open circuit voltage increased to 1.02 V, and the



efficiency reached 8.1%. This indicates that ion migration can also improve the performance of the perovskite solar cell in some cases. Ion migration not only has an influence to the performance of perovskite solar cell, but also has an influence of the properties of the material itself. Finally, the ion migration was intimately correlated the giant dielectric constant of MAPbI<sub>3</sub> at low frequency<sup>[54]</sup>, but there are few reports pointing out the clear relationship between the ion migration and the giant dielectric constant. It is also the case for the ferroelectric or piezoelectric effects which can be dependent on the ion's migration in MAPbI<sub>3</sub><sup>[55]</sup> <sup>[56]</sup>. Exhaustive investigations and analysis are needed for better understating of the key role of the ion's mobility in the physical features of such hybrid perovskites media.

#### **1.4 Dielectric properties of MAPbI<sub>3</sub>**

The dielectric properties of materials refer to the nature of the storage and loss of electrostatic energy under an applied electric field. These properties are usually expressed in terms of dielectric constant which reflects the ability of the material to store charge and the dielectric loss traducing the lost part of stored electrical energy. The dielectric constant is closely related to the frequency of the applied electric field, as shown in Figure 1.6. As the frequency decreases, the material responds more fully to the external electric field and the dielectric constant becomes larger. At different frequencies, dielectric response has different physical mechanisms. Thus, up to 10<sup>14</sup> Hz and above, the physical mechanism is related to the electronic displacement polarization. The effect is primarily a change in the shape of the electron clouds within atoms caused by the electric field and leading to induced dipole moments. The electronic displacement polarization which occurs in all materials, is independent on the temperature and has a very short completion time. As the frequency decreases, ionic displacement polarization occurs around 10<sup>12</sup> Hz to 10<sup>13</sup> Hz and is mainly due to the separation and movement in opposite direction of anions and cation in ionic crystals under the electric field. The ionic displacement polarization which is generally weak, occurs in ionic crystals and depends on the temperature and on the ion spacing. As the frequency is further reduced, the dipole moments of the molecules or defect dipoles in

the polar dielectric, which are originally randomly oriented, will be reoriented under the electric field. The resulting dipole moment is then finite and the mechanism is called orientation polarization which depend also on the electric field and on the thermal motions. The polarization relaxes during characteristic times typically  $10^{-2}$  to  $10^{-6}$  s or even longer. For some dielectric materials, there are some weakly bonded charged particles which will migrate under the applied electric field leading to the non-uniform charge distribution in the dielectric. This polarization is called thermal ion relaxation polarization which is closely related to the thermal motion and requires longer relaxation times  $10^{-2} \sim 10^{-10}$  s. Finally, another polarization mechanism concerns the space charge polarization, which occurs mainly in inhomogeneous dielectric materials. It arises from the accumulation of freely moving charges at the interface of different media and defects.

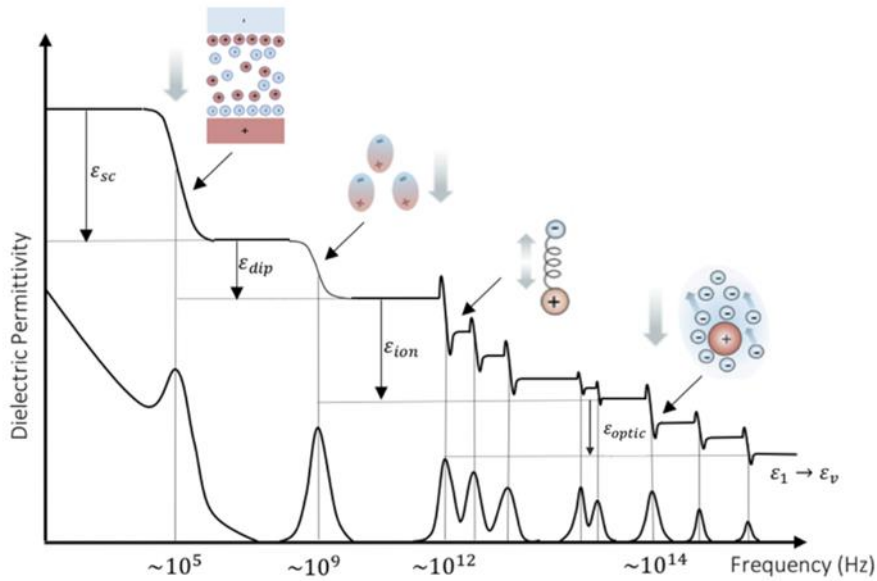


**Figure 1.6** Illustration of the frequency dependent dielectric spectrum<sup>[57]</sup>

Due to the existence of MA<sup>+</sup> groups with permanent dipole moments in MAPbI<sub>3</sub>, the reorientation of MA<sup>+</sup> under the electric field will change the dielectric properties of MAPbI<sub>3</sub>. Therefore in order to investigate the dynamics of the MA<sup>+</sup>, Yan-Fang Chen et al.<sup>[58]</sup> explain the temperature dependent dielectric constant using the Kirkwood–Fröhlich–Onsager theory. The results confirmed that in the orthorhombic phase MA<sup>+</sup> exhibit an anti-parallel orientation and the dielectric constant is temperature-

independent. However, with the temperature increase, the anti-parallel orientation is gradually disrupted in the tetragonal phase and the dielectric constant is temperature-dependent and will decrease significantly with the increase of temperature. The anti-parallel orientation of MA<sup>+</sup> in orthorhombic phase is consistent with the neutron diffraction results of Mark T. Weller<sup>[25]</sup>. Sharada Govinda et al<sup>[59]</sup> also studied the temperature characteristics of the dielectric constant of MAPbX<sub>3</sub> (X=Br, I) in the range of 1 kHz to 1 MHz with the results shown in figure 1.7. It was found that the dielectric constant of MAPbX<sub>3</sub> shows significant temperature-dependence which is related to the free rotation of MA<sup>+</sup> on the probe time scale. This interpretation is supported by the ab initio molecular dynamics simulations on MAPbI<sub>3</sub> showing that these dipoles are randomly oriented with a rotational relaxation time scale of ~7 ps at 300 K. Further, they probe the intriguing possibility of transient polarization of these dipoles following a photoexcitation process with important consequences on the photovoltaic efficiency. This approach was carried out by a photoexcitation pump and second harmonic generation as a probe with delay times spanning 100 fs–1.8 ns. The absence of a second harmonic signal at any delay time rules out the possibility of any transient ferroelectric state under photoexcitation. This result contradicts the conclusion that the reorientation of MA<sup>+</sup> will contribute to the ferroelectricity in MAPbI<sub>3</sub><sup>[60]</sup>.

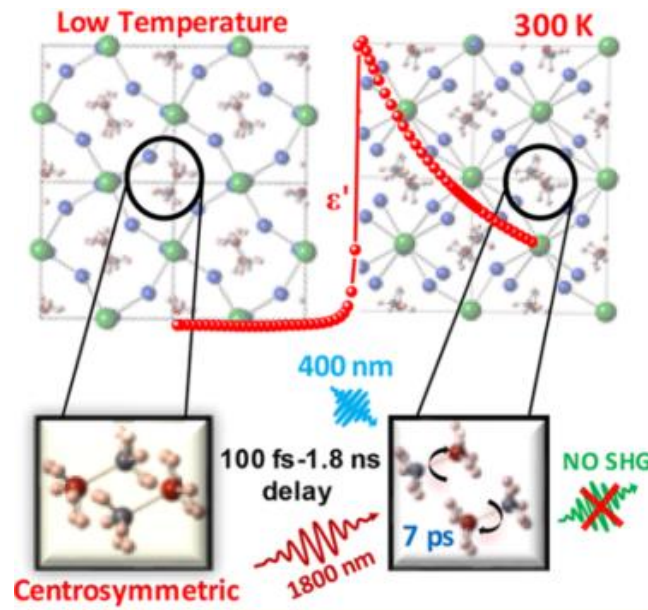


**Figure 1.7** The orientation state of MA<sup>+</sup> at different temperatures<sup>[59]</sup>

Although the temperature-dependence of the dielectric constant of MAPbI<sub>3</sub> has been well studied and clear conclusions have been drawn, some problems have been encountered in the study of the frequency-dependence of dielectric constant of MAPbI<sub>3</sub>. Emilio J. Juarez-Perez et al.<sup>[61]</sup> found a giant dielectric constant phenomenon in MAPbI<sub>3</sub> at low frequency with dielectric constant up to 1000. In addition, the dielectric constant further increases under illumination or by changing the injection at an applied bias as shown in figure 1.8. This study suggested that these anomalous dielectric properties are attributed to the structure fluctuations. Photoinduced carriers modify the local unit cell equilibrium and change the polarizability, assisted by the free rotation of MA<sup>+</sup>. Darryl P. Almond et al.<sup>[62]</sup> found similar phenomena in water-saturated porous samples of lead zirconate titanate (PZT), and thus they attributed this phenomenon to the changes in the conductivity and dielectric constant at low frequencies, rather than to some intrinsic properties of materials. However, Jarvist M. Frost et al.<sup>[63]</sup> point out that the giant dielectric constant at low frequencies of MAPbI<sub>3</sub> may be due to ion migration. Hoque et al.<sup>[64]</sup> suggested that the Maxwell-Wagner interfacial polarization is attributed to the anomalous dielectric properties. In this condition, the accumulation of charges occur at the grain boundaries or contact surface between electrode and samples. Shaikh et al.<sup>[65]</sup> reported the same effect on the dielectric properties under the illumination of MAPbBr<sub>3</sub> single crystal leading to a 23-fold increase in the dielectric constant at 150 Hz. Light-induced reorientation was suggested to be the origin of the anomalous dielectric properties. In addition, Sheikh et al.<sup>[66]</sup> found a dielectric relaxation in MAPbI<sub>3</sub> films which can be described by the cole-cole model. The impedance spectra and electric modulus suggested that this dielectric relaxation is related to the localized electron.

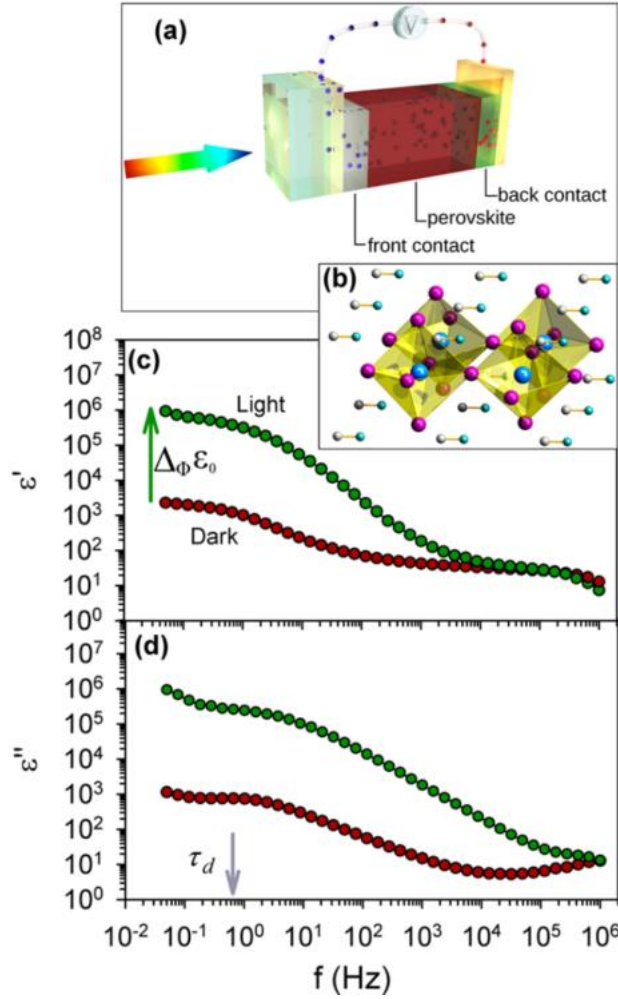


**Figure 1.8** (a) Scheme of the experimental devices; the arrow indicates light incident side. (b) Tetragonal perovskite, phase at room temperature. (c) Real and (d) imaginary part of dielectric permittivity as a function of frequency under dark and 1 sun illumination conditions, measured at room temperature and 0 V applied bias<sup>[61]</sup>

Anusca et al.<sup>[54]</sup> analyzed the dielectric constant of organic-inorganic hybrid with different compositions and in a broad frequency range (Figure 1.9). This study suggested that the rapid increase in the dielectric constant at low frequency; i.e. in the region A is due to the migration of ions. There is a slight increase in the dielectric constant in the region B, which results from the orientation polarization of MA<sup>+</sup>. In C region, the change of dielectric constant is related to the lattice vibration of the anions. As discussed before, the origin of the anomalous dielectric constant and the effect of illumination on the dielectric properties is still not clear and under debate. So further

investigation and analysis are essential and necessary to understand the anomalous dielectric properties of MAPbI<sub>3</sub>.

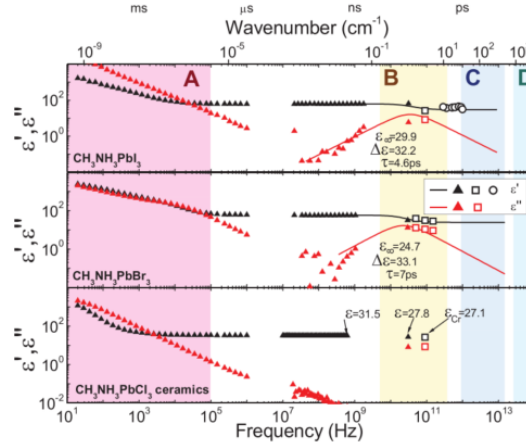


**Figure 1.9** The dielectric constant of the three MA-Pb-halides across a wide frequency spectrum<sup>[54]</sup>

## 1.5 Electrostrictive and piezoelectric response of MAPbI<sub>3</sub>

### 1.5.1 Electrostrictive effect of MAPbI<sub>3</sub> and its research progress

Electrostriction is a fundamental electromechanical coupling phenomenon in all dielectrics and insulators. It reflects the relationship between the strain induced by the electric field or the polarization and the electric field or polarization. The relationship can be described by the expression below:

$$S_{ij} = Q_{ijkl} P_k P_l \quad \dots(1.1)$$

$$S_{ij} = M_{ijkl} E_k E_l \quad \dots(1.2)$$

Where  $Q_{ijkl}$  and  $M_{ijkl}$  represent electrostrictive coefficients which is the fourth rank polar tensor observed in all materials. In general, the strains induced by the electrostrictive effect is smaller than those induced by the piezoelectric effect. Therefore, the application of electrostrictive materials is limited. However, the discovery of relaxor ferroelectrics with large electrostrictive coefficients such as Pb(Mg<sub>1/3</sub>Nb<sub>2/3</sub>)O<sub>3</sub>(PMN), Pb(Zn<sub>1/3</sub>Nb<sub>2/3</sub>)O<sub>3</sub>(PZN) attracted the attention of researchers in 1980s<sup>[67-68]</sup>. Relaxor ferroelectrics have a small hysteresis under electric field comparing with the piezoelectric materials which will have a high displacement accuracy. No residual strain, no aging effect, and no need to be poled make them more

useful for application in actuator and bistable optical devices. Subsequently, polymers with large strains induced by the electrostriction gained the widespread interest. Ultra-high electrostrictive strains were observed in these polymeric materials (>4% for polyvinylidene fluoride [PVDF] and >40% for silicone), giving them potential for use in actuator applications<sup>[69-70]</sup>.

The electrostriction is a measure of the polarization induced by ions displacement away from their natural equilibrium positions, giving rise to variations in the lattice parameters (strain). In centrosymmetric crystals, the induced shifts of equivalent ions almost cancel each other out, while the difference in the shifts because of potential anharmonicity generates strain. For an ion-pair system, the energy required to compress the particle at equilibrium is higher than the energy required to expand, so the electrostriction  $Q_{33}$  is generally positive in the length direction for ionic crystals. There are five main methods for measuring the electrostrictive coefficient<sup>[71]</sup>. The first method is based on the relationship between the strain, polarization, and the electric field. According to the equations 1.1 and 1.2, the electrostrictive coefficient can be calculated by the strain-polarization curve (S-P) or strain-electric field (S-E)<sup>[72]</sup>. The second method is measuring the change of the dielectric constant under applied stress based on the inverse electrostrictive effect<sup>[73]</sup>. The third method uses the calculation of the electrostrictive coefficient based on the piezoelectric coefficient which is mainly applied to the ferroelectrics. The fourth method is to calculate the electrostrictive coefficient from the variation of the lattice parameters<sup>[74]</sup>. The last method estimates the electrostrictive coefficient from the change of the dielectric constant under dc bias<sup>[75]</sup>. Like the electrostriction, Maxwell stress can also lead the strain which is also proportional to the square of the electric field or polarization<sup>[70]</sup>. It is difficult to separate this component from the strain induced by the electrostriction. When an electric field is applied to the surface of an insulator coated with electrodes, the electrostatic force due to the squeeze back and forth of the free charge is called Maxwell stress. The relationship between longitudinal strain ( $S_M$ ) induced by the Maxwell stress and electric field can be described by the expression below<sup>[76]</sup>:

$$S_M = -\frac{1}{2}s\varepsilon E^2 \quad \dots(1.3)$$

Where  $s$  represents the elastic compliance and  $\varepsilon$  is the dielectric constant. The difference between the Maxwell stress-induced strain and electrostrictive strain is that the former is caused by the changes in the charge on the electrode surface while the latter is caused by the potential anharmonicity. However, since the two have the same law with electric field or polarization, it is difficult to distinguish them. Therefore, when studying the electrostrictive response, the strain induced by the Maxwell strain must be taken into consideration.

Since the dielectric constant can reflect the intensity of the polarization, it is obvious that the dielectric constant of materials has a close relationship with the electrostrictive coefficient. It was reported in former works that for polymers and relaxor ferroelectrics the electrostrictive coefficient obey the empirical formula<sup>[77]</sup>:

$$Q = 2.37 \cdot \left(\frac{s}{\varepsilon_0 \varepsilon}\right)^{0.59} \quad \dots(1.4)$$

For linear dielectric, the relationship between polarization and electric field is:

$$P = \varepsilon_0(\varepsilon' - 1) E \quad \dots(1.5)$$

Substituting formula 1.5 into formula 1.1, the relationship between  $M$  and  $Q$  can be obtained as follows:

$$M = Q \cdot \varepsilon_0^2(\varepsilon' - 1)^2 \quad \dots(1.6)$$

Combining 1.4, for linear dielectric, the electrostrictive coefficient  $M$  is positively correlated with the dielectric constant. For ferroelectric materials, although the relationship between polarization and electric field is non-linear, the electrostrictive coefficient  $M$  should be also positively correlated with the dielectric constant. The electrostrictive coefficients of some materials also confirm this conclusion<sup>[77]</sup>. For example, the electrostrictive coefficient  $M$  85%Pb(Mg<sub>1/3</sub>Nb<sub>2/3</sub>)O<sub>3</sub>-15%PbTiO<sub>3</sub>(PMN-PT) with the dielectric constant exceeding 20000 reaches  $3 \times 10^{-16} \text{ m}^2\text{V}^{-2}$ . For SrTiO<sub>3</sub> with a small dielectric constant about 200, the electrostrictive coefficient  $M$  is less than  $10^{-18} \text{ m}^2\text{V}^{-2}$ . Although for classic electrostrictive materials such as polymer and relaxor ferroelectrics, the electrostrictive coefficient can be deduced by the dielectric constant. However, researchers have discovered that in materials with a dielectric constant of less



than 100 such as Gd-doped CeO<sub>2</sub> and (Y, Nb)-Stabilized  $\delta$ -Bi<sub>2</sub>O<sub>3</sub>, the electrostrictive coefficient is as high as  $10^{-17} \text{ m}^2\text{V}^{-2}$ . The large electrostrictive coefficient is attributed to the large concentration of anion vacancies showing a completely different phenomenon from classic electrostrictive materials<sup>[77-78]</sup>. Roman Korobko et al.<sup>[79]</sup> used the in-situ X-ray absorption fine structure to study the electrostriction of Gd-doped CeO<sub>2</sub> and found that the defects will lead to the distortion of the crystal structure under electric field as shown in figure 1.10. The distortion leads to the asymmetry of the charge distribution and the form of dipole moment, thereby improving the electrostriction of the materials.

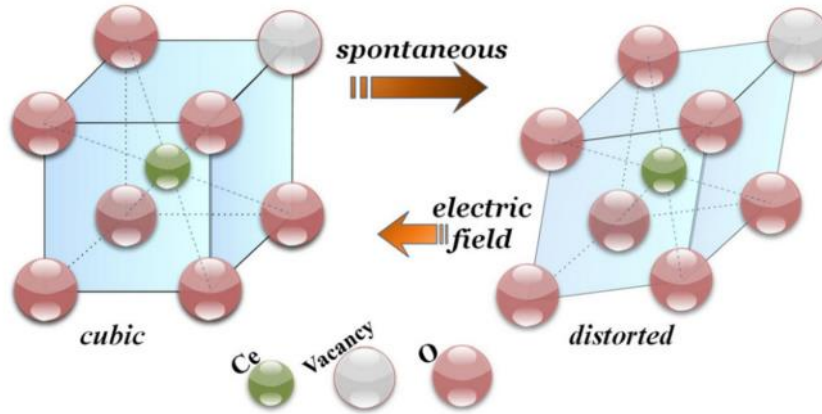


**Figure 1.10** Scheme of the electric field induced reorganization of a distorted Ce near neighbor coordination shell containing an oxygen vacancy<sup>[79]</sup>

At present, there is a lack of deep and extensive research on the electrostriction of MAPbI<sub>3</sub>. Jinsong Huang et al.<sup>[80]</sup> found a large electrostrictive response in MAPbI<sub>3</sub> single crystals. The strain can reach 1% at 3.7 V/ $\mu\text{m}$  at 10 Hz and the electrostrictive coefficient is as high as  $7.3 \times 10^{-16} \text{ m}^2\text{V}^{-2}$  and will increase as the frequency decreases. The schematic diagram and the experimental results were shown in figure 1.11. After excluding the Maxwell stress and MA<sup>+</sup> orientation, some studies show that this large electrostrictive coefficient may be due to the Frenkel defects induced under the electric field. However, Dong et al.<sup>[81]</sup> found that there is no obvious electrostriction observed in the MAPbI<sub>3</sub> single crystals after dc poling. There are contradictions between the two studies. If defects can contribute to the electrostriction, the electrostrictive coefficient

in the MAPbI<sub>3</sub> single crystals after dc poling should be larger than that in the samples without poling. Therefore, the electrostriction in MAPbI<sub>3</sub> single crystal need to be further studied and clarified.

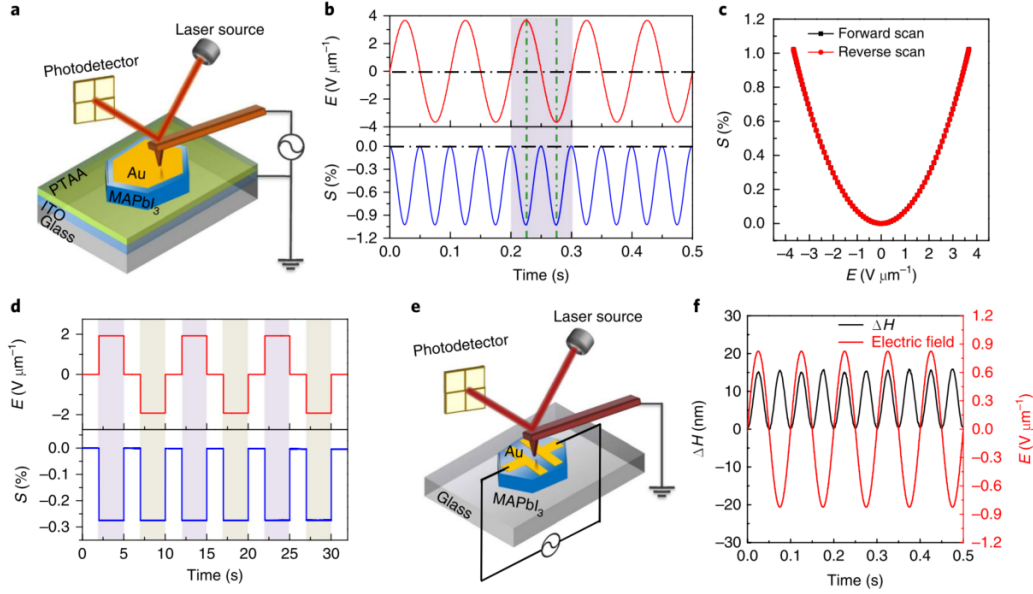


**Figure 1.11** Electrostrictive response of MAPbI<sub>3</sub> single crystal. (a) Schematic illustration of AFM measurement of strain induced by electric field. (b) Electrostrictive strain of a 40  $\mu\text{m}$  MAPbI<sub>3</sub> single crystal under a.c. bias at 10 Hz. (c) Relation between strain and electric field for the MAPbI<sub>3</sub> single crystal. Schematic illustration of setup (e) and experimental result (f) for out-of-plane lattice deformation under in-plane electric field.  $\Delta H$  is the detected thickness change by AFM<sup>[80]</sup>

### 1.5.2 Piezoelectricity of MAPbI<sub>3</sub> and its research progress

When a pressure acts on dielectrics, the induced strain will lead to a change in the intensity of polarization which result in the release of the surface charge of the material. The change in the surface charge of the material caused by the mechanical action is called the piezoelectric effect. On the contrary, the phenomenon that the material will produce a strain effect under electric field is called the inverse piezoelectric effect. For a centrosymmetric crystal, strain will not lead to a change in the intensity of polarization, therefor the material will not produce piezoelectric effect. Among the 32 kinds of point groups in nature, only 20 kinds of space groups exhibit a piezoelectric effect. From the experiment side, Piezo-response force microscopy (PFM) is widely used in the study

of ferroelectric and piezoelectric properties of MAPbI<sub>3</sub> films. As shown in figure 1.12, Coll et al.<sup>[82]</sup> investigated the piezoelectric properties of MAPbI<sub>3</sub> films by PFM. The piezoelectric coefficient  $d_{zz}$  was evaluated at 5 pm/V under dark conditions. However, the piezoelectric coefficient is as high as 25 pm/V under illumination and the coercive force will gradually decrease with time. This phenomenon is completely opposite to that previously found in the PZT films<sup>[83-84]</sup>. Indeed, the piezoelectric coefficient of PZT films will decrease due to the decrease of the polarization intensity under ultraviolet light. Therefore, the mechanism of the enhancement of the piezoelectric coefficient of MAPbI<sub>3</sub> films under illumination need to be further analyzed. However, Song et al.<sup>[85]</sup> reported that the piezoelectric coefficient of the MAPbI<sub>3</sub> films deposited on the substrates such as Au, ITO is at about only 0.3-0.4 pm/V. This contrasts with the value 4 pm/V in MAPbI<sub>3</sub> films prepared by epitaxial growth using the PZT films as substrates. The authors attributed this phenomenon to the MA<sup>+</sup> alignment induced by the non-equilibrium chemical potential on the surface of the PZT films. The piezoelectric coefficient of MAPbI<sub>3</sub> films measured by Kim<sup>[86]</sup> using PFM was about 5.12 pm/V. It was also shown that the samples after poling have a higher output voltage and current density. This indicated that poling can improve the piezoelectric coefficient. On the other hand, Ippili et al.<sup>[87]</sup> found that the piezoelectric coefficient will reach the value of  $17.0 \pm 0.6$  pm/V by doping Fe<sup>2+</sup>. Ding et al.<sup>[88]</sup> investigated the piezoelectric properties of FAPbBr<sub>3</sub> nanoparticles through PFM and its piezoelectric coefficient was as high as 25 pm/V. For PFM, as the conductive probe is in direct contact with the samples, the measured piezoelectric coefficient may be not consistent with the intrinsic piezoelectric coefficient<sup>[89]</sup>. For ion conductors, the material will produce a stress gradient under the electric field and the probe. This stress gradient will lead to flexoelectricity which will yield large piezo-response force microscopy signals<sup>[90]</sup>. To avoid the influence of some extrinsic factor, Zeng et al.<sup>[91]</sup> used PFM with the interferometric displacement sensor (IDS-PFM) to measure the piezoelectric coefficient of MAPbI<sub>3</sub> more accurately and compared it with quartz and V<sub>2</sub>O<sub>5</sub>. It is found that the piezoelectric signals of MAPbI<sub>3</sub> is significantly lower than that of quartz which indicates that the previously reported piezoelectric coefficient of MAPbI<sub>3</sub> may be not intrinsically involved.

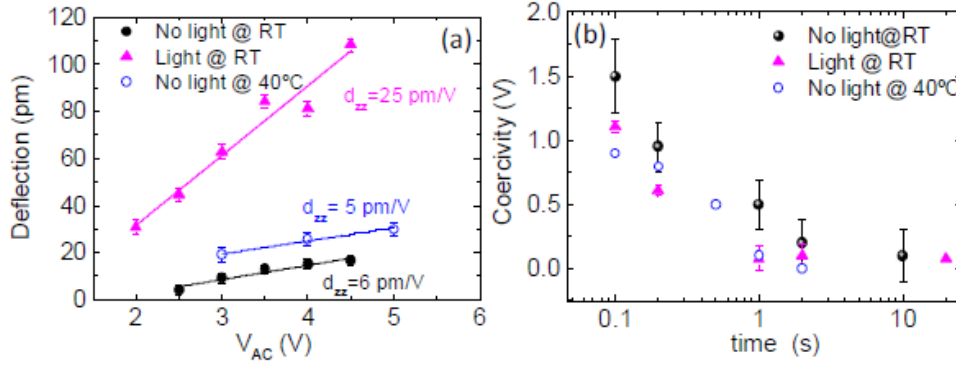


**Figure 1.12** (a) Deflection versus  $V_{AC}$  and (b) coercivity dependence with time for MAPbI<sub>3</sub> films in the dark at room temperature (RT) (black circles), under illumination (pink triangles) and in dark and at 40 °C (blue open circles)<sup>[82]</sup>

Compared with PFM, the laser interferometry has a higher accuracy in the measurement of displacement due to the not direct contact with samples. The measurement accuracy of the single-beam laser interferometry can reach  $10^{-3}$  nm<sup>[92]</sup>. The piezoelectric coefficient of MAPbI<sub>3</sub> single crystal which is poled for 5 min at 0.1 V  $\mu\text{m}^{-1}$  as measured by Dong et al.<sup>[81]</sup> using the laser interferometry was 2.7 pm/V. But it is striking that this study did not investigate the piezoelectric coefficient of MAPbI<sub>3</sub> single crystal without poling. For ferroelectric ceramics, poling will change the orientation of the ferroelectric domains, thereby the piezoelectric coefficient is enhanced<sup>[93]</sup>. Although the studies of Kim and Ippili et al. reported about the increase of the output voltage and current of the piezoelectric generator by poling, neither of them discussed the influence of the poling on the piezoelectric properties of the material. Kim et al.<sup>[94]</sup> found that the piezoelectric coefficient of CsPbBr<sub>3</sub> after poling was as high as 40 pm/V, and successfully applied it to energy harvesting and current sensors. The origin of this high-voltage electrical effect is believed to be due to changes in the crystal structure caused by the extension of the Pb-Br-Pb bond angle along the b-axis and the extension of Br-Pb-Pb along the ac plane.

## 1.6 Progress on the ferroelectric properties of MAPbI<sub>3</sub>

Many published works claimed that the reason that MAPbI<sub>3</sub> has so excellent photovoltaic performance lies in the ferroelectric properties of MAPbI<sub>3</sub>. The built-in

electric field formed by the spontaneous polarization in the ferroelectric material can promote the separation of electron and holes which can explain its high carrier lifetime, longer carrier diffusion length and high open circuit voltage in solar cells. However, the initial research on the crystal structure of MAPbI<sub>3</sub> did not support this conclusion. Earlier studies believed that the space group of the tetragonal MAPbI<sub>3</sub> at room temperature is centrosymmetric I4/mcm<sup>[95-96]</sup>. However, Mark T. Weller et al.<sup>[25]</sup> investigated the structure and ion orientation of MAPbI<sub>3</sub> by neutron diffraction. It was found that although the space group is I4/mcm, there are distortion of the structure, resulting in four possible orientations of organic ions. It indicated the possibility of a spontaneous polarization in MAPbI<sub>3</sub>. Stoumpos et al.<sup>[97]</sup> suggested that the space group of MAPbI<sub>3</sub> will lose symmetry due to the lattice distortion and become I4cm.

The spontaneous polarization is only a prerequisite but not a sufficient condition for the material to be ferroelectric. Only when the spontaneous polarization can be reversed with the applied electric field, the material is the ferroelectric. Rothmann, M. U et al.<sup>[98]</sup> used piezoelectric response force microscopy (PFM) to observe directly the existence of a domain structure in the MAPbI<sub>3</sub> films, and found that the ferroelectric domain can be switched under DC voltage. These two phenomena demonstrated that MAPbI<sub>3</sub> is a ferroelectric. Rakita et al.<sup>[28]</sup> demonstrated that the tetragonal MAPbI<sub>3</sub> single crystal at room temperature is a ferroelectric material from many aspects. Firstly, they confirmed the existence of the thermoelectric properties of the material caused by spontaneous polarization; secondly, they fitted the hysteresis loop by studying the change of the imaginary part of the dielectric constant of the material. Then they observed the morphology of ferroelectric domains by optical microscope. These effects indicate the involvement of ferroelectric features in this material. Although some reports claimed that the MAPbI<sub>3</sub> is ferroelectric based on the domain structure observed by PFM, it remains unclear that no ferroelectric hysteresis loop was observed in MAPbI<sub>3</sub><sup>[99-101]</sup>. Therefore, many authors claimed that there is no ferroelectricity in MAPbI<sub>3</sub>. Another evidence on the absence of a ferroelectricity may be related to the nonexistence of a second harmonic generation (SHG)<sup>[99, 102]</sup> in these systems. This absence of SHG indicates that the crystal structure is centrosymmetric and the material

cannot produce spontaneous polarization. The possible reason for these contradictory results may be explained by the existence of ferroelectricity but with very weak strength. From the investigations of Wang et al.<sup>[103]</sup> on the effect of the annealing temperature on the crystallinity and ferroelectric properties, it was deduced that the crystalline quality is highly improved for annealing at 90 °C and then the ferroelectricity of the material can be demonstrated. Kim et al.<sup>[104]</sup> found that the samples with larger grain have larger spontaneous polarization under electric field. After removing the applied electric field, the residual polarization of the samples with large grains is also larger than that with the smaller grains. According to the theoretical calculations, Zhao et al.<sup>[105]</sup> found that after replacing Pb with Ge in MAPbI<sub>3</sub>, the material has large polarization and good photoelectric properties. However, few reports have investigated the influence of the doping on the ferroelectricity of MAPbI<sub>3</sub>.

Although the ferroelectricity remains open debate, the results of *ab initio* calculation indicated that the tetragonal phase with spontaneous polarization is more stable than the tetragonal phase without spontaneous polarization at room temperature<sup>[100, 106-107]</sup>. The calculation results of Fan et al.<sup>[100]</sup> show that the polarization intensity of material about 8  $\mu\text{C}/\text{cm}^2$  is mainly due to the orientation of  $\text{MA}^+$  while the contribution of  $\text{Pb}^{2+}$  displacement from the octahedral center is weak. The mechanism of spontaneous polarization is different from the BaTiO<sub>3</sub> as supported by Stroppa et al.<sup>[108]</sup>. But the same work pointed out the origin of the polarization is not related to the orientation of  $\text{MA}^+$  groups but due to their position shifts relative to the surrounding PbI<sub>6</sub>. In addition, the hydrogen bond has a certain contribution to the polarization, and changing halogen atom to enhance the hydrogen bond may be a new way to enhance the ferroelectricity. However, the calculation made by Yan et al.<sup>[109]</sup> using density functional theory (DFT) and Bayley phase method show that the polarization is mainly due to the deviation of  $\text{Pb}^{2+}$  from the octahedron rather than organic ions. Thus, the mechanism of ferroelectricity of MAPbI<sub>3</sub> requires further development and investigations to prove the relevance of the theoretical simulation. In this context, the calculations of Berdiyorov et al.<sup>[110]</sup> using the DFT approach and Green function found that the electron transport of the material will be enhanced in the

presence of charged domain walls. This approach on the enhancement of physical features by modulating the domain structure has been developed on the BiFeO<sub>3</sub> films<sup>[111]</sup>. Similarly, we can use this approach to modify the properties of material by domain engineering. On the other hand, Feng et al.<sup>[112]</sup> found that according to the temperature-dependent density functional theory, the band gap of MAPbI<sub>3</sub> is 1.50 eV and the sharp drop of absorption coefficient near the absorption edge is attributed to the ferroelectricity. Sergey et al.<sup>[113]</sup> calculated the static conductivity of the charged domain wall in different states, and found that electrons and holes diffuse and accumulate in the domain wall. Due to this accumulation phenomenon, the conductivity at the domain wall is 3 to 4 orders of magnitude higher than in the normal state, this phenomenon can be used to explain the large carrier diffusion distance of MAPbI<sub>3</sub>. Conventional measurement methods such as hysteresis loop cannot effectively measure the ferroelectric properties of materials. Due to the advantages of PFM in the measurement of micro-area ferroelectric properties, Chen et al.<sup>[114]</sup> proved the existence of MAPbI<sub>3</sub> ferroelectricity through PFM measurements. Thus, they confirmed the role of ferroelectricity in organic-inorganic hybrid perovskite solar cells. The mechanism may lie in the ferroelectricity which can adjust the band gap on the surface of perovskite solar cells, and the poling will expand the depletion zone and promote the separation of holes and electrons. Röhm et al.<sup>[115]</sup> found domains of alternating polarization with a width of 90 nm in vertical and horizontal PFM imaging which was identified as polarized ferroelectric domains depicted in figure 1.13. These ferroelectric domains are highly ordered with different polarization directions and the ferroelectric domains are still clearly visible in the pc-PFM mode. Figure 1.13 (b) shows the surface morphology of the samples which exclude the influence of the surface morphology on the ferroelectric domains. As the surface potential of the sample is close and correlates with the sample composition, this indicates that there is no residual incomplete reaction precursor on the sample surface.

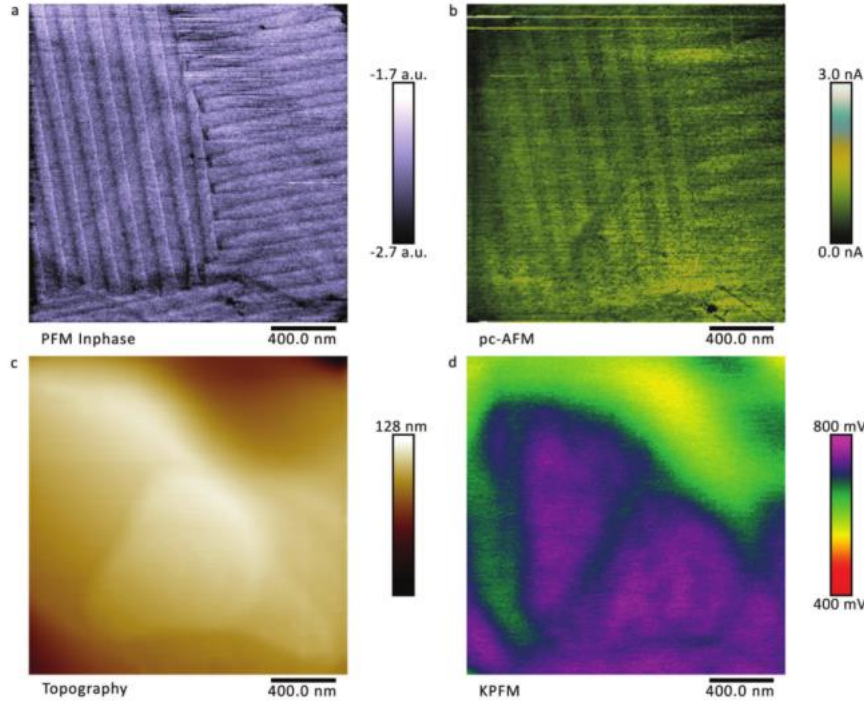


**Figure 1.13** High-resolution (a) PFM, (b) pc-AFM, (c) topography and (d) KPFM images<sup>[115]</sup>

In addition, Rothmann et al.<sup>[98]</sup> reports the involvement of twin domains in the MAPbI<sub>3</sub> films by transmission electron microscope. The twin domains will reappear and disappear during the transition from tetragonal phase to the cubic phase. Although twin domains are not a proof that the material is ferroelectric, a perovskite structure as BaTiO<sub>3</sub> shows also twin domains emanating from the ferroelectric domains<sup>[116]</sup>. However, Hermel et al.<sup>[117]</sup> also discovered the existence of striped domains through PFM but these striped domains are arranged in parallel or perpendicular to each other. This morphology is a characteristic of ferroelastic domains rather than ferroelectric ones. Although the existence of the striped domain structure has been confirmed by numerous experiments, the reasons for their appearance are still unresolved. Huang et al.<sup>[118]</sup> attributed the domain structure in the MAPbI<sub>3</sub> single crystal films to the alternating arrangement of polar regions and non-polar regions and Liu et al.<sup>[32]</sup> pointed out that the domain structure present in the material is caused by the difference in elastic coefficient between different domain structures, rather than due to the electromechanical coupling effect. This study proved that the observed domain structure is closely related to ions migration by SEM, helium ion microscope (HIM),



secondary ion mass spectrometry (HIM-SIMS), and nano-infrared spectroscopy (AFM-IR).

### 1.7 Phase transition from tetragonal to cubic phase of MAPbI<sub>3</sub>

There are three different phases of MAPbI<sub>3</sub> at different temperatures. Below 162 K, it is orthorhombic phase. Between 162 K and 327 K, it is tetragonal phase. Above 327 K, it is cubic phase. Since the phase transition between the tetragonal and cubic phases occurs near 327 K, the phase transition temperature is relatively low, which is within the operating temperature range of perovskite solar cells<sup>[119]</sup>, it has attracted the attention of many researchers. As shown in Figure 1.14, there is an entropy change and thermal effect during the MAPbI<sub>3</sub> tetragonal phase to cubic phase transition indicating that the phase transition is of first-order phase character. However, the results of neutron diffraction indicate that the phase transition is a second-order phase transition<sup>[25]</sup>. Yukihiro et al.<sup>[95]</sup> analyzed the data obtained by X-ray diffraction and found that the phase transition is close to critical point. As shown in Figure 1.15, The rotation of the PbI<sub>6</sub> octahedron is considered to be the order parameter of the cubic-tetragonal transition. Finally, the reason why the value of the exponent  $\beta$  is not 0.5 but about 0.25 can be explained in three ways. (1) The critical behavior appears as similar to SrTiO<sub>3</sub>, where the exponent is about 1/3), (2) The transition takes place accidentally near the tricritical point. Then the classical value of the exponent is 1/4, (3) Since the transition is a first order one, a small discontinuity effectively suppresses the exponent.

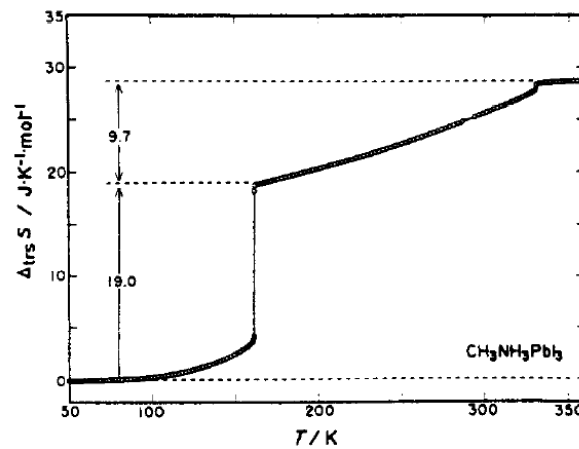
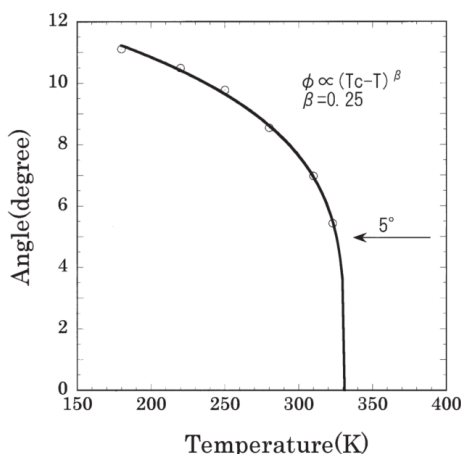


Figure 1.14 Transition entropy of MAPbI<sub>3</sub><sup>[120]</sup>



**Figure 1.15** The temperature dependence of the rotation angle of the PbI<sub>6</sub> octahedron in the tetragonal phase of MAPbI<sub>3</sub><sup>[95]</sup>

### 1.8 Application of MAPbI<sub>3</sub> in photocatalysis

Because MAPbI<sub>3</sub> is a semiconductor and has excellent photoelectric properties, it has a good light absorption coefficient in the visible light range, and its application in solar cells is very successful. The application of this material in photocatalytic reactions is worthy of interest due the involvement of efficient photoactivity in this compound. The principle of photocatalysis is shown in Figure 1.16. By irradiating the semiconducting sample by a suitable wavelength spectrum, electron and hole pairs are generated. However, if a part of the electron-hole pairs recombines, the efficiency of the photocatalytic reaction will be low. When the separated electrons and holes reach the surface of the semiconductor, they induce the formation of electron active centers such as superoxide and hydroxyl radicals. Redox reactions are then promoted by these radicals and can be exploited in environment preservation (water treatment) or in green energy through the hydrogen production from water splitting. At present, the most popular photocatalysts include the following types: (1) Nanometal oxides or sulfides, such as TiO<sub>2</sub> which is widely used as photocatalyst. The good chemical and thermal stability and relatively low price, and non-toxicity make this oxide quite attractive. The only limitation concerns the large band gap which can only absorb light in the ultraviolet range limiting the catalytic performance<sup>[121-122]</sup>; (2) Coupled Semiconductors catalyst, which mainly couples two different catalysts with different band gaps, were

also considered as a promising way to create synergetic effect between photocatalysts for better efficiency. Some examples are among CdS-TiO<sub>2</sub>, CdS-ZnO, etc.<sup>[123]. [124]</sup>, (3) Perovskite type Oxide catalysts such as BaTiO<sub>3</sub>, SrTiO<sub>3</sub>, etc., which mainly utilize the built-in electric field formed by the spontaneous polarization of ferroelectric materials which can effectively promote the effective separation of photo-generated electron pairs, thereby increasing the photocatalytic efficiency<sup>[125-126]</sup>.

MAPbI<sub>3</sub> material is sensitive to moisture and start easily decompose in aqueous solution<sup>[127-128]</sup>. However, most of the photocatalytic reactions occur in aqueous solution, its application in photocatalysis is limited. One solution is that MAPbI<sub>3</sub> does not directly contact the aqueous solution, by placing the photocatalyst outside of the electrolyte, and connecting it to the electrolyzer through a wire may decompose the water to produce H<sub>2</sub> and O<sub>2</sub><sup>[129-130]</sup>. Another solution is to integrate the perovskite with the catalytic hydrogen evolution device, and use encapsulation technology to isolate the electrolyte from MAPbI<sub>3</sub> to protect MAPbI<sub>3</sub> from degradation. Micaela Crespo-Quesada et al.<sup>[131]</sup> used InBiSn alloy as a MAPbI<sub>3</sub> protective layer to successfully realize hydrogen production. The structure is shown in Figure 1.17. First the perovskite solar cell is prepared, and its structure is shown in Figure 1.17(a); then a layer of InBiSn alloy is deposited on the Ag electrode as a protection, as shown in Figure 1.17(b). MAPbI<sub>3</sub> does not directly contact the aqueous solution. However, the structure is too complicated to be applied on a large scale. Park et al.<sup>[132]</sup> reported the H<sub>2</sub> evolution using MAPbI<sub>3</sub> as a photocatalyst in aqueous HI solution, but the observed H<sub>2</sub> evolution rate is far inferior to those obtained with traditional semiconductor photocatalytic materials<sup>[114]</sup>. To solve the problem, Wu et al.<sup>[21]</sup> made some improvements and successfully prepared a highly efficient and stable hydrogen evolution by combining MAPbI<sub>3</sub> and reduced graphene oxide (rGO). Powder samples of MAPbI<sub>3</sub>/rGO (100 mg) show a H<sub>2</sub> evolution rate of 93.9  $\mu\text{mol h}^{-1}$ , which is 67 times faster than that of pristine MAPbI<sub>3</sub>, under 120 mWcm<sup>-2</sup> visible-light ( $\lambda \geq 420$  nm) illumination, and the composite is highly stable showing no significant decrease in the catalytic activity after 200 h (i.e., 20 cycles) of repeated H<sub>2</sub> evolution experiments. Huang et al.<sup>[133]</sup> studied the composite material of FAPbBr<sub>3</sub> and TiO<sub>2</sub> in the catalytic oxidation of benzyl alcohol. They found

that the combination of FAPbBr<sub>3</sub> and TiO<sub>2</sub> can achieve high-efficiency catalysis of benzyl alcohol and has good selectivity. This result shows the good application prospect of organic-inorganic hybrid perovskite in photocatalysis.

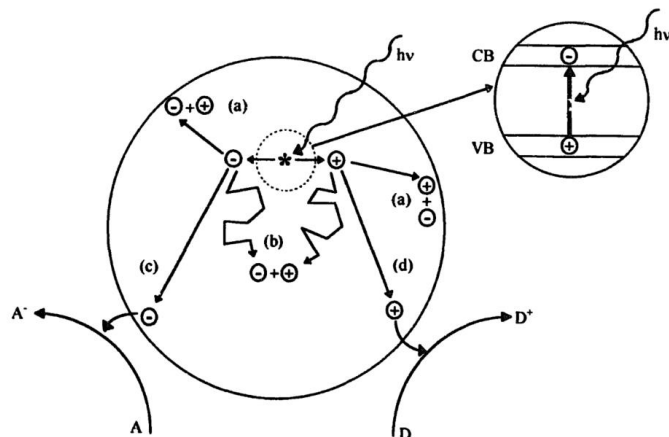


**Figure 1.16** Illustration of the major processes occurring on a semiconductor particle following electronic excitation. Electron-hole recombination can occur at the surface (reaction (a)) or in the bulk (reaction (b)) of the semiconductor. At the surface of the particle, photogenerated electrons can reduce an electron acceptor A (reaction (c)) and photogenerated holes can oxidize an electron donor D (reaction (d))<sup>[134]</sup>

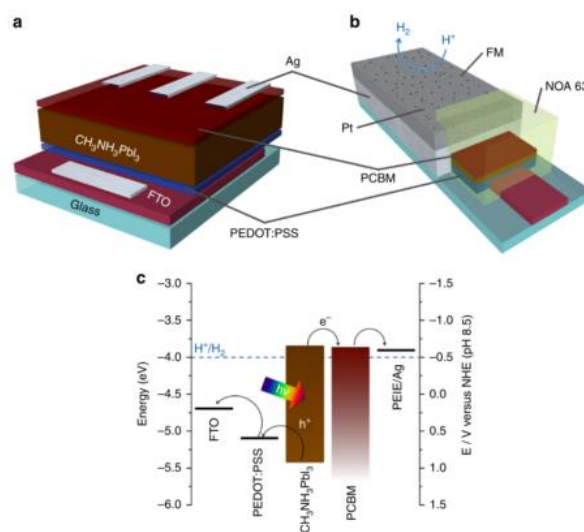


**Figure 1.17** Material and electronic configuration of the perovskite-based solar cells and photocathodes. (a) Schematic representation of the structure of the perovskite solar cell. (b) Scheme of the solar cell adapted as a photocathode for solar H<sub>2</sub> production. The structure remains the same. (c) Energy diagram of both devices<sup>[131]</sup>

## Chapter 2 Experimental process and test equipments

### 2.1 Sample preparation

#### 2.1.1 Raw materials

The relevant information of the raw materials involved in the experiments is shown in Table 2.1.

**Table 2.1** Raw materials used in the experimental process.

Raw materials	Molecular formula	Specification	Manufacturer
Methylamine Hydroiodide	$\text{CH}_3\text{NH}_3\text{I}$	99%	TCI
Lead (II) iodide	$\text{PbI}_2$	99.9%	Aladdin
Gamma-butyrolactone	$\text{C}_4\text{H}_6\text{O}_2$	$\geq 99\%$	Aladdin
N,N-Dimethylformamide	$\text{C}_3\text{H}_7\text{NO}$	$\geq 99.5$	Sinopharm Chemical ReagentCo
Titanium dioxide	$\text{TiO}_2$	99.48%	Sinopharm Chemical ReagentCo
Butyronitrile	$\text{CH}_3(\text{CH}_2)_2\text{CN}$	$\geq 99\%$	TCI
Caesium iodide	$\text{CsI}$	99.999%	Aladdin
			Sinopharm Chemical
Benzyl alcohol	$\text{C}_7\text{H}_8\text{O}$	99.5%	ReagentCo

#### 2.1.2 Process of preparing single crystals by inversion temperature crystallization method

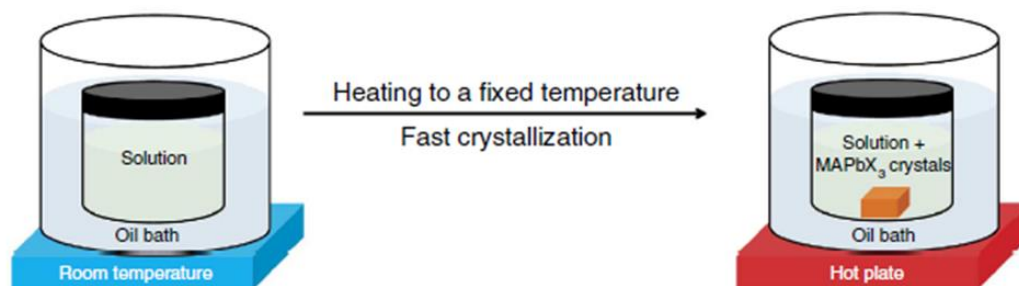


**Figure 2.1** Schematic representation of inverse temperature crystallization<sup>[135]</sup>

Using the inverse temperature crystallization method, high-quality bulk hybrid perovskite single crystals were prepared.  $\text{CH}_3\text{NH}_3\text{I}$  (1.2717 g) and  $\text{PbI}_2$  (3.6881 g) were dissolved in 8 mL of  $\gamma$ -butyrolactone (GBL) solution with constant stirring at 60 °C for 12 h, and then the solution was put in an oven at 130 °C. The crystallization process for the single-crystal growth develops slowly with time, leading to faceted monocrystals with a size of  $1 \times 0.5 \times 0.5 \text{ cm}^3$ .

### **2.1.3 Powder preparation**

There are two main methods to prepare the power of  $\text{MAPbI}_3$ : solvent evaporation method and anti-solvent method. The solvent evaporation method is to dissolve a certain amount of  $\text{CH}_3\text{NH}_3\text{I}$  and  $\text{PbI}_2$  in N,N-dimethylformamide (DMF) and stir it at 60 °C for 12 h to fully dissolve, and then transfer the solution to an oven at 150 °C for drying to get  $\text{MAPbI}_3$  powder. The solution preparation of the anti-solvent method is the same as the solvent evaporation method. The only difference is that the anti-solvent method drops the fully stirred solution into the toluene solution drop by drop. Since  $\text{MAPbI}_3$  is insoluble in the toluene solution, the powder will deposit on the bottom of the solution. Then the powder is separated from the solution by a centrifuge, rinsed with toluene for many times and then dried to prepare the  $\text{MAPbI}_3$  powder. The Cs-doped  $\text{MAPbI}_3$  is prepared by solvent evaporation method.  $\text{MAPbI}_3/\text{TiO}_2$  is prepared by the anti-solvent method.

### **2.1.4 Films preparation**

Dissolve a certain amount of  $\text{CH}_3\text{NH}_3\text{I}$  and  $\text{PbI}_2$  in DMF and stir it at a constant temperature of 60 °C for 3 hours to fully dissolve the solution, use a 0.22  $\mu\text{m}$  filter to filter the solution. Use pipette to measure a certain amount of solution and drop by drop onto the F-doped  $\text{SnO}_2(\text{FTO})$  on the homogenizer. Finally, the FTO glass spin-coated with  $\text{MAPbI}_3$  solution was annealed at 90 °C for 30 min to obtain films. The FTO glass was first ultrasonically cleaned with deionized water for 10 minutes, followed by ultrasonic cleaning with acetone and alcohol for 10 minutes, and finally with deionized water ultrasonic cleaning for 10 minutes, and then the FTO glass was blown dry with a hair dryer.

## 2.2 Characterization of sample structure and properties

### 2.2.1 Material phase analysis

The material phase analysis uses the Empyrean XRD of the PANalytical Company, the target is a copper, the test voltage is 40 kV, the current is 30 mA, and the scanning method is 2 Theta-Omega scanning. X-ray powder Rietveld refinement uses MAUD software.

### 2.2.2 Microstructure analysis

The microscopic morphology analysis and composition analysis of the samples in this study used a scanning electron microscope (SEM, JEOL JSM6510 LV, Japan) equipped with an X-ray energy spectrometer (EDS, X-MaxN, Oxford, UK).

### 2.2.3 Raman spectroscopy

Raman spectroscopy test adopts Lab-Ram HR800 Raman spectrometer equipped with Linkam THMSE 600 heating and cooling device. The analysis range is  $50\text{ cm}^{-1}$ ~ $300\text{ cm}^{-1}$ , and the temperature measurement range is  $20\text{ }^{\circ}\text{C}$ - $120\text{ }^{\circ}\text{C}$ .

### 2.2.4 Electrical performance test

#### (1) Dielectric properties test

In this study, the dielectric properties were measured by the German Novocontrol broadband dielectric spectrometer, and the liquid nitrogen temperature control system was used. The test temperature range is  $-160\text{ }^{\circ}\text{C}$ ~ $300\text{ }^{\circ}\text{C}$ , and the frequency range is  $10^{-2}\text{ Hz}$ - $10^6\text{ Hz}$ . Figure 2.2 shows the schematic diagram of dielectric measurement. The sample is placed between the upper and lower electrode plates to form a capacitor structure. A voltage  $U_0$  with a frequency of  $\omega/2\pi$  is applied to the sample. At the same time, the sample will generate a current  $I_0$  with the same frequency. Due to the capacitance effect, there will be a phase difference  $\varphi$  between the current and the voltage, as shown in Figure 2.3. The relationship between the voltage  $U_0$  and the current  $I_0$  depends on the electrical properties (dielectric constant and conductivity) and the geometry of the samples. The relationship between the voltage and current can be expressed by the following formula:

$$U(t) = U_0 \cos(\omega t) = \text{Re}(U^* \exp(i\omega t)) \quad \dots(2.1)$$

$$I(t) = I \cos(\omega t + \varphi) = \text{Re}(I^* \exp(i\omega t)) \quad \dots(2.2)$$

Where  $U_0=U^*$ , and  $I^* = I' + iI''$ ;  $I_0 = \sqrt{I'^2 + I''^2}$ ;  $\tan(\varphi) = \frac{I''}{I'}$

For samples with linear electrical response, the impedance can be calculated by the following formula:

$$Z^* = Z' + iZ'' = \frac{U^*}{I^*} \quad \dots(2.3)$$

The dielectric constant can be calculated by impedance:

$$\varepsilon^*(\omega) = \varepsilon' - i\varepsilon'' = \frac{-i}{\omega Z^*(\omega)} \frac{1}{C_0} \quad \dots(2.4)$$

where  $C_0$  represents the capacitance without samples. The relationship between conductivity and dielectric constant can be expressed by the following formula:

$$\sigma^* = \sigma' - i\sigma'' = i2\pi f \varepsilon_0 (\varepsilon^* - 1) \quad \dots(2.5)$$

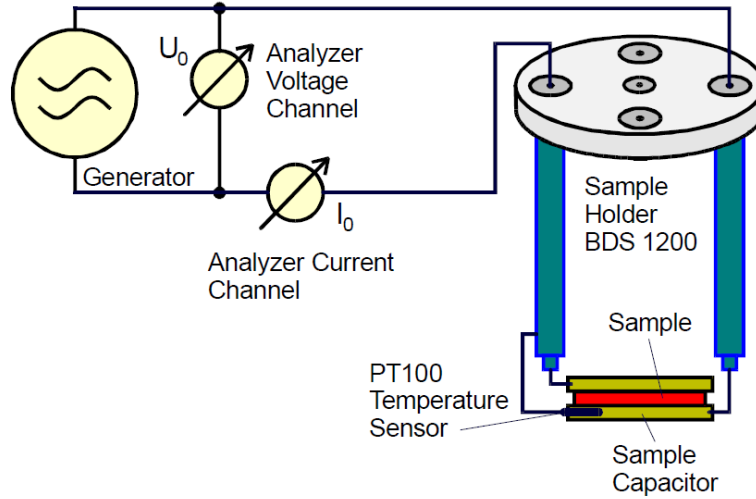


**Figure 2.2** Principle of a dielectric measurement



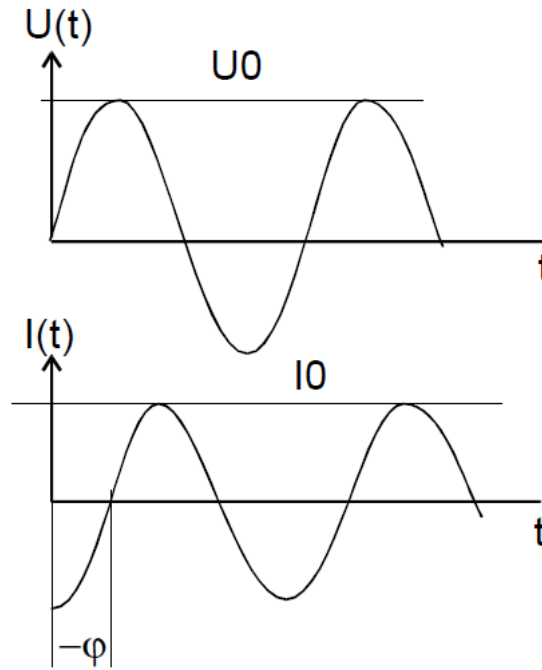


**Figure 2.3** Amplitude and phase relations between voltage and current of a sample for electric measurements

### (2) Electrostrictive and piezoelectric response measurement

The measurement of electrostrictive and piezoelectric response is mainly carried out by laser Doppler interferometer. The strain induced by electrostriction and piezoelectricity can be measured by vibration measuring instrument. When an AC voltage is applied to the sample, the vibration generated by the sample can be collected by the German Polytec mechanical vibrometer, and then decoded by the decoder to obtain the strain amplitude, and then the electrostrictive and piezoelectric response of the material can be calculated.

### (3) Hysteresis loops measurement

The electric hysteresis loop of the material is analyzed by the German aixACCT TF-2000E measurement system, which is equipped with a heating device and a laser strain test system. The maximum test voltage is 4 kV and the test temperature is between room temperature and 200 °C. In order to protect the sample cell, the sample is immersed in silicone oil during the test. The hysteresis loop measurement adopts the improved Sawyer-Tower circuit, and its test principles diagram is shown in Figure 2.4.

Sawyer-Tower uses the reference capacitance to measure the charge change on the sample. Since the voltage drop of the reference capacitor is proportional to the polarization charge, when the voltage of the reference capacitor rises, the voltage on the sample will drop. Therefore, in order to ensure the accuracy of the voltage applied to the sample, the reference capacitance is much larger than the sample's capacitance.

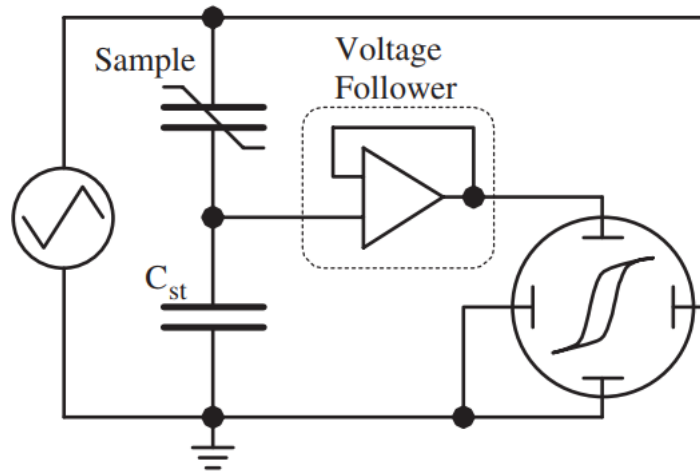


**Figure 2.4** The schematic diagram of hysteresis loop<sup>[136]</sup>

### 2.2.5 Piezo-response force microscopy measurement

The piezoelectric force microscope test uses the Japanese Hitachi company model AFM5300 atomic force microscope. The testing principle is shown in Figure 2.5. After applying an oscillating voltage to the sample, the probe in direct contact with the sample will test the bending degree  $D_{dc}$  of the cantilever due to the existence of electromechanical effects. When the polarization direction of the sample is consistent with the applied voltage direction, due to the existence of the inverse piezoelectric effect, the bending degree  $D_{dc}$  of the cantilever is a positive value, and when the polarization direction is opposite to the applied voltage, it is a negative value.

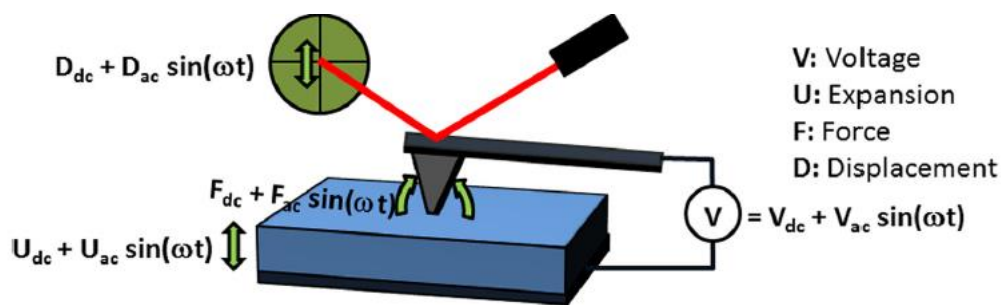


**Figure 2.5** Schematic of the setup for piezo-response force microscopy<sup>[137]</sup>

### 2.2.6 Optical properties measurement

The absorption spectrum of the material is tested using Japan's Hitachi U410 UV-Vis spectrophotometer, the test wavelength range is 200 nm-2000 nm, and the sample can be bulk, powder or liquid. The instrument is composed of a light source, a monochromator, an absorption cell, a detector, and a signal display system. The test principle is that the electrons in the material absorb photons and make energy level transitions. Because different materials have different absorption ranges and absorption strengths, each material has its own unique optical absorption spectrum, which can be qualitatively and quantitatively analyzed.

### 2.2.7 Photocatalytic oxidation efficiency measurement

Dissolve 1 uL of benzyl alcohol in 10 ml of toluene solution to prepare a 1 mmol/L solution, and then add 10 mg of MAPbI<sub>3</sub>/TiO<sub>2</sub> powder to the solution for ultrasonic dispersion. The resulting solution was placed under a 500 W xenon lamp to illuminate the photocatalytic oxidation reaction. After 1 h of illumination, draw 1 ml of the solution with a syringe and filter, and use a gas chromatograph to analyze the content of benzyl alcohol and benzaldehyde. The inlet temperature of the gas chromatograph is 200 °C, the FID (flame ionization detector) temperature is 250 °C, and the chromatographic column is an SE-54 capillary column.



## Chapter 3 Dielectric properties of MAPbI<sub>3</sub>

### 3.1 Introduction

In the last few years, hybrid perovskites with the chemical formula CH<sub>3</sub>NH<sub>3</sub>PbI<sub>3</sub>(MAPbI<sub>3</sub>) have attracted more attention owing to their outstanding optoelectronic properties, notably as absorber layers in perovskite solar cells. Suitable band gap, long charge carrier diffusion length, large light absorption, and low electron–hole recombination contribute to the excellent performances of MAPbI<sub>3</sub>-based solar cells. Despite exhaustive reports devoted to hybrid perovskites, several mechanisms are not fully elucidated to account for remarkable behaviors due to ferroelectric, dielectric, or electro-optical properties.

In particular, the hysteresis response that affects the photocurrent density–voltage (J–V) in perovskite solar cells was attributed to different mechanisms such as ferroelectricity<sup>[138]</sup>, charge trapping<sup>[139]</sup>, and ion migration<sup>[140]</sup>. However, controversial assignments were reported in favor of ferroelectric domains<sup>[115]</sup>, while recent reports claimed the relevance of ion migration<sup>[141]</sup>. In this frame, the giant dielectric constant induced at low frequencies in the MAPbI<sub>3</sub> films under light irradiation was attributed to structural fluctuations, which correlate with photoinduced change in electrical conductivity and dielectric losses<sup>[61]</sup>. However, several works suggested that abnormal dielectric phenomena are related to ion migration<sup>[63, 142]</sup>. In addition, the dielectric relaxation shown in MAPbI<sub>3</sub> films was considered as a bulk effect arising from the semiconducting grains and the Maxwell-Wagner-type interfacial polarization<sup>[66]</sup>. In fact, ion-migration processes alter the dielectric properties in ion conductors<sup>[143-144]</sup>, but few reports have pointed out a clear correlation between the ion migration and huge changes in the dielectric properties in hybrid perovskites. Thus, the present work is devoted to experimental characterizations and exhaustive analysis of the dielectric properties and electrical conductivity in MAPbI<sub>3</sub> single crystals. The mechanisms behind the frequency and temperature dependence of dielectric functions were considered including ion migration and the reorientation of MA<sup>+</sup>. Modified Cole-Cole and Debye

relaxation models (DRMs) were used for the adjustment of dielectric features, while modified ac conductivity power law was relevant to account for ion migration. In addition, by studying the dielectric temperature spectrum of MAPbI<sub>3</sub>, the orientation of MA<sup>+</sup> in different phases and the influence of non-polar particles Cs<sup>+</sup> on its orientation are analyzed.

### 3.2 Sample preparation and characterization

Using the inverse temperature crystallization method<sup>[135]</sup>, high-quality bulk hybrid perovskite single crystals were prepared. 1.2717 g CH<sub>3</sub>NH<sub>3</sub>I and 3.6881 g PbI<sub>2</sub> were dissolved in 8 mL  $\gamma$ -butyrolactone (GBL) solution with constant stirring at 333 K for 12 h, and then the solution was put in the oven at 403 K. The crystallization process for the single crystal growth develops slowly with time leading to faceted monocrystals with size as 1×0.5×0.5 cm<sup>3</sup>. The parallel (1 0 0) faces of the single crystal were coated with sliver thin layer. Dielectric measurements were carried out by using Novocontrol Broadband dielectric spectrometer operating in the frequency range [0.01 Hz, 1 MHz] and at different temperatures [-193 K, 303 K]. The samples were placed between the electrodes of the dielectric setup with an applied AV voltage of 1 V amplitude. Cs<sup>+</sup>-doped MAPbI<sub>3</sub> powder was prepared by solvent evaporation method, the powder was pressed into a wafer and annealed, and then Ag electrodes were coated to test the dielectric properties.

### 3.3 The relationship between the dielectric properties of MAPbI<sub>3</sub> single crystal and ion migration

#### 3.3.1 XRD pattern of MAPbI<sub>3</sub> single crystals

The XRD pattern of MAPbI<sub>3</sub> single crystals is shown in Figure 3.1, and the inset is a photograph of the single crystal. It can be seen that there are two diffraction peaks at 19.9° and 40.5° corresponding to the (200) and (400) crystal planes, which indicates that the growth direction of the single crystal is mainly along the (001) direction.

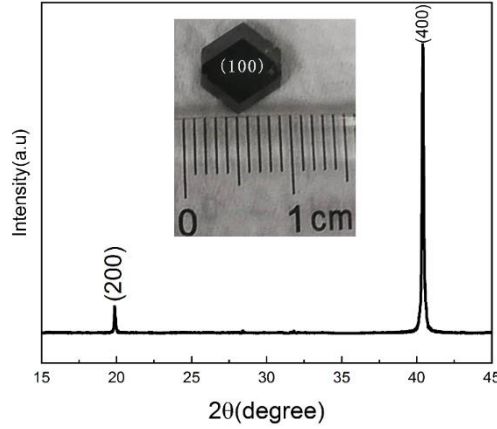


**Figure 3.1** The XRD pattern with the inset of photograph of MAPbI<sub>3</sub> single crystal

### 3.3.2 The giant dielectric constant of MAPbI<sub>3</sub> single crystal

Figure 3.2 (a) and (b) report the frequency-dependence of the real ( $\epsilon'$ ) and imaginary part of dielectric constant ( $\epsilon''$ ) measured at different temperatures. The curves of ( $\epsilon'$ ) show a step-like frequency dependence which reaches anomalously large values especially in the low frequency range at 303 K. The measured large dielectric constant in the single crystal agrees with previous reports<sup>[64, 145]</sup> attributing its origin to Maxwell-Wagner type interfacial polarization. However, as no grain boundaries are involved in a single crystal, the Maxwell-Wagner type interfacial polarization model is no longer relevant to explain this phenomenon in the present case. Similar behaviors related to large  $\epsilon'$  were also reported in the ionic conductors ZrO<sub>2</sub>-Y<sub>2</sub>O<sub>3</sub><sup>[146]</sup> and Sm-doped CeO<sub>2</sub><sup>[147]</sup> and the effects were attributed to the migration and the hopping of the mobile ions.

A suitable approach to describe the frequency-dependence of  $\epsilon'$  at different temperatures with the step-like variation is developed based on the phenomenological dielectric model Cole-Cole as follows:

$$\epsilon^* = \epsilon_{\infty} + \frac{\epsilon_s - \epsilon_{\infty}}{1 + (i\omega\tau_1)^{1-\alpha}} \quad \dots(3.1)$$

where  $\epsilon_{\infty}$  and  $\epsilon_s$  are the high-frequencies value of relative permittivity and static relative permittivity, respectively,  $\omega$  is the angular frequencies,  $\tau_1$  refers to the dielectric relaxation time and  $\alpha$  traduces the involvement of a distribution of the relaxation times. In particular,  $\alpha = 0$  stands for an ideal Debye relaxation, whereas  $0 < \alpha < 1$  refers to a distribution of relaxation times in the process.<sup>[148]</sup> At

high temperatures, the electrode/space charge should be considered to explain the sharp increase of dielectric constant at low frequencies. Thus, equation (3.1) was modified as follows by a frequency power law<sup>[144, 149]</sup> :

$$\varepsilon^* = \varepsilon_\infty + \frac{\varepsilon_s - \varepsilon_\infty}{1 + (i\omega\tau_1)^{1-\alpha}} - \frac{i\sigma^*}{\varepsilon_0\omega^s} \quad \dots(3.2)$$

where  $\sigma^*$  ( $\sigma^* = \sigma_1 + i\sigma_2$ ) is the complex conductivity resulting from free charge carries  $\sigma_1$  and spaces charge  $\sigma_2$ ; the exponent “s” is related to the carrier polarization mechanism which is usually between 0 and 1.

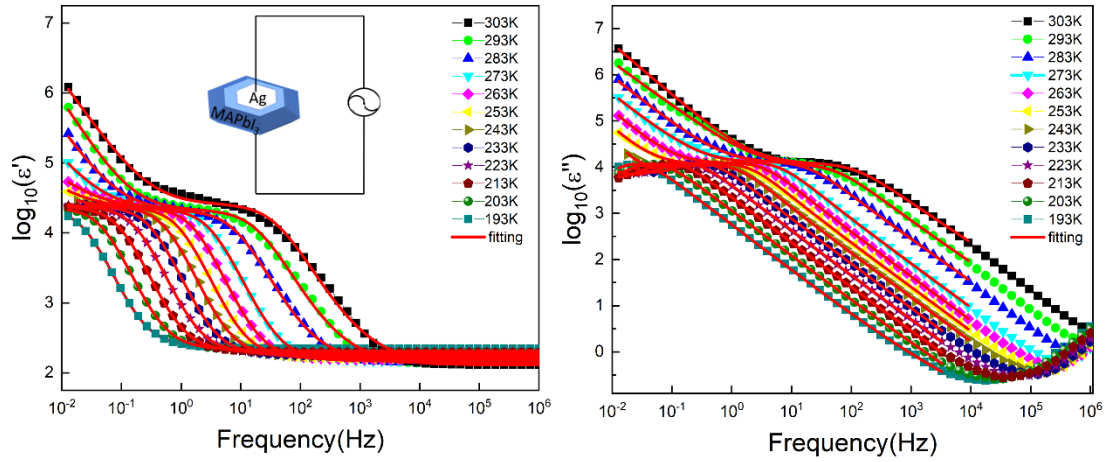


**Figure 3.2.** Real part(a) and imaginary part (b) of dielectric constant as a function of frequencies recorded at various temperatures. The continuous red line corresponds to the best fits from the modified Cole-Cole equation. The inset diagram represents schematically the dielectric setup configuration

As illustrated in Figure 3.2(a) and (b), the frequency dependence of the real and imaginary part dielectric functions is well accounted for by Debye relaxation model (DRM). The fitting parameters of the model  $\varepsilon_s$ ,  $\varepsilon_\infty$ ,  $s$ ,  $\alpha$ ,  $\sigma_1$ ,  $\sigma_2$ ,  $\tau_1$ , are summarized in Table 3.1 versus the temperatures. The parameter  $\alpha = 0$  in the temperature range 193-273 K is indicative of the relevance of a pure DRM to account satisfactorily for the dielectric behavior in MAPbI<sub>3</sub> monocrystals with the involvement of a single relaxation time. Nevertheless, for  $273 \leq T \leq 303$  K, a small increase of the parameter  $\alpha$  is required in the DRM to reproduce the measured dielectric functions. This small departure from pure DRM above 273 K is indicative of a slight dispersion of the relaxation times which



can be induced by a thermal stimulation of ionic mobility such as methylamine MA<sup>+</sup> groups cations or vacancies creation.

**Table 3.1.** Dielectric parameters at various temperatures calculated using equation (3.2)

T(K)	$\epsilon_s$	$\epsilon_\infty$	s	$\alpha$	$\sigma_1(10^{-10}\text{S}/\text{m})$	$\sigma_2(10^{-10}\text{S}/\text{m})$	$\tau_1(\text{s})$
303	16692	130	1	0.078	17608	6737	0.00238
293	17558	135	1	0.073	12122	2866	0.00664
283	18296	140	1	0.057	4650	1332	0.0170
273	20329	146	1	0.014	1926	533	0.0487
263	21426	152	0.892	0.002	1233	300	0.0957
253	21592	158	0.862	0	629	186	0.166
243	22102	166	0.843	0	291	98.0	0.285
233	22255	174	0.829	0	152	61.3	0.503
223	22085	184	0.805	0	81.5	37.4	0.894
213	21790	194	0.813	0	42.7	24.5	1.65
203	22080	206	0.622	0	27.5	10.4	3.23
193	21189	220	0.609	0	19.3	7.51	6.46

The dielectric relaxation time of the Debye model is reported in the temperature range [193 K, 303 K] (Table 3.1). We may notice the corresponding values from few seconds at low temperature to milliseconds at room temperature. A such range of values is indicative of a relaxation process associated to space charge distribution at the interfaces of single crystal-electrodes. The thermal variation of  $\tau_1$  reported in Figure 3.3(a) follows an Arrhenius law such as  $\tau(T)=\tau_0\exp(E_a/kT)$  where  $\tau_0$ ,  $E_a$ ,  $k$  represent respectively a proportionality constant, an activation energy and the Boltzmann constant. A crossover occurs in the thermal variation where the activation energy increases abruptly at 273 K from 0.25(5) eV to 0.70(5) eV. This behavior is consistent with the results of the parameter  $\alpha$  of the relaxation model and with the static dielectric constant  $\epsilon_s$  (Figure 3.3(b)). Indeed,  $\epsilon_s$  shows a nearly stationary value in the temperature range  $193 \leq T \leq 273$  K where the pure Debye model is relevant with a single relaxation process. This contrasts with the behavior in the temperature range  $273 \leq T \leq 303$  K where a dramatic decrease occurs due to the activated motions of MA<sup>+</sup> ions<sup>[58-59]</sup> which alter the space charge density. The similar thermal behaviors marked by changes on the activation energy is also evidenced for the electrical conductivity deduced from

dielectric measurements and their simulations. Thus, the real part of the conductivity ( $\sigma_1$ ) is related to the free charges involved in the crystal. Both electronic and ionic transport coexist and their thermal activation manifests through the increase of  $\sigma_1$  with increasing the sample temperature as illustrated in Figure 3.3(c). The plot of  $\ln(T \cdot \sigma_1)$  versus the inverse temperature ( $1/T$ ) shows two linear variation regimes according to the Arrhenius law with an activation energy  $E_a=0.28(5)$  eV for  $190 \leq T \leq 273$  K and  $E_a=0.57(5)$  eV for  $273 \leq T \leq 303$  K. These high values of the activation energies are indicative of the involvement of ionic transport favored by the formation defects which ensure lattice stability and local charge balance. In MAPbI<sub>3</sub>, in contrast to Pb<sup>2+</sup> ions with high activation energy, methyl amine cation MA<sup>+</sup> and iodide anion I<sup>-</sup> are the main charge carrier species which may diffuse in the lattice to induce electrical conductivities with moderate activation energies.<sup>[44]</sup> The crossover regime for the activation energy which take place around 273 K is relevant to the conduction relaxation being dominated by iodide anion I<sup>-</sup> at low temperatures and by the contribution of MA<sup>+</sup> cations to the ionic transport at high temperatures. Such aspects will be also discussed on the frequency dependent conductivity in forthcoming section.

The imaginary part of the conductivity ( $\sigma_2$ ) is inferred from the space charge which also increases with rising the temperature (Figure 3.3 (d)). This behavior suggests that more ions are accumulated at the electrodes at high temperatures. The characteristic activation energies for the ionic transport were also found in the thermal evolution of  $\sigma_2$ . This indicates the close correlation between ionic transport and the space charge density which occurs at the interfaces of crystal-electrodes.

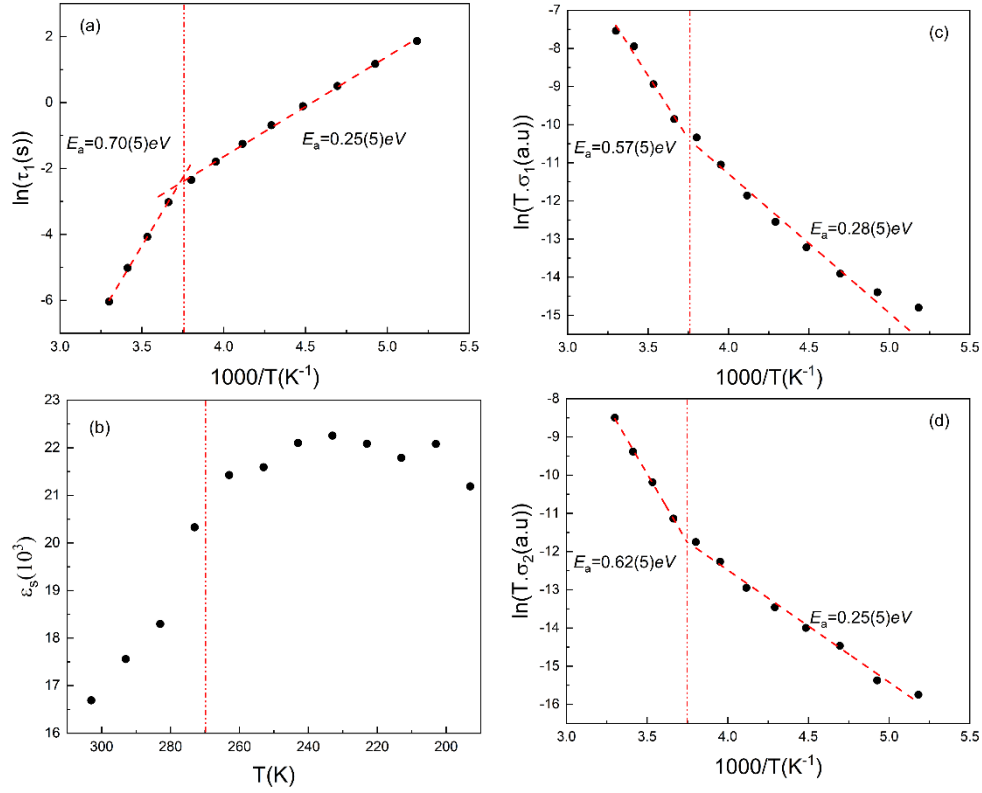


**Figure 3.3** (a) Logarithmic variation of the Debye model versus  $1000/T$ . (b) static dielectric constant  $\epsilon_s$ . (c) real part  $\sigma_1$  and (d) the imaginary part  $\sigma_2$  of the electrical conductivity thermally activated in MAPbI<sub>3</sub> single crystal.

### 3.3.3 The reorientation of MA<sup>+</sup>

Due to the giant dielectric constant at low frequencies dominated by the space charge contribution, the representation of the real and imaginary dielectric constants  $\epsilon'$  and  $\epsilon''$  at high frequencies is relevant to characterize the contribution from MA<sup>+</sup> dipolar reorientations. Figure 3.4(a) reports the experimental data along with the simulation curves based on modified Debye model. Thus,  $\epsilon'$  is almost stationary up to 1 MHz and exhibits a net decrease at higher frequencies as accounted for by a Debye like relaxation model. The dielectric relaxation in this frequency range originates from dipolar species which can be assigned in our compound to the reorientation of the organic cations MA<sup>+</sup> with permanent dipole moments.<sup>[54, 150]</sup> The latter exhibit disordered orientations in the 12-fold cuboctahedral coordination of the MA<sup>+</sup> site at room temperature and tend to be ordered as the temperature decreases. For the imaginary part of the dielectric constant  $\epsilon''$ , the frequency dependence reported at 193 K in Figure 3.4(a) agrees with the dipolar relaxation of organic cation MA<sup>+</sup> as discussed

for  $\varepsilon'$ . However, in contrast to the simulation trend,  $\varepsilon''$  shows an upward variation with decreasing the frequency indicating the occurrence of space charge relaxation process as discussed in previous report<sup>[57]</sup>. Figure 3.4(b) reports the temperature evolution of  $\varepsilon''(\omega)$  with the position of the minimum being gradually shifted to higher frequencies with increasing the temperature as it can be expected from the thermal increase of the relaxation frequency related to reorientation of MA<sup>+</sup> dipoles.

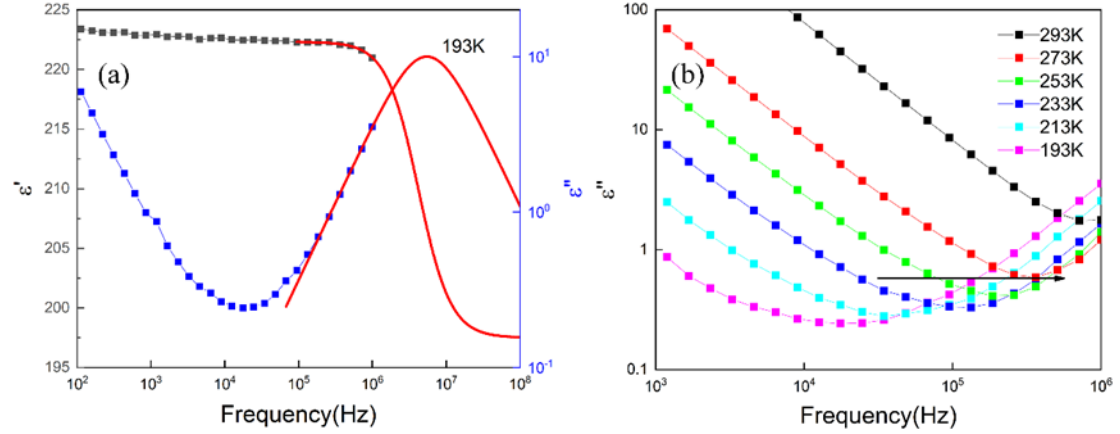


**Figure 3.4.** (a) The real part and imaginary part of dielectric constant as a function of frequency recorded at 193 K with the experimental measurements represented by square symbols (black, blue) and the continuous red lines associated with the simulation model of Debye relaxation. (b) The imaginary part of dielectric constant of high frequencies recorded at different temperature

### 3.3.4 Ac conductivity of MAPbI<sub>3</sub> single crystals

Dielectric relaxation and ac conductivity are sensitive to the motion of charge species.<sup>[151]</sup> Thus, the study of ac conductivity behavior may provide more information on the ionic transport mechanism. The complex conductivity is defined from the dielectric function according to the relation<sup>[152]</sup>:

$$\sigma^* = i2\pi f \varepsilon_0 (\varepsilon^* - 1) \quad \dots(3.3)$$

Figure 3.5(a) and (b) show the real ( $\sigma'$ ) and imaginary ( $\sigma''$ ) parts of the complex conductivity at the temperature range of 193-303 K. As shown in the frequency dependence of  $\sigma'$ , three regimes are clearly involved as function of the frequency range. In the intermediate range (a), a stationary conductivity is involved and can be assigned to a dc conductivity. The low frequency range (b) is marked by the effects from charge

space density at the interface crystal electrodes where the conductivity decreases sharply with decreasing the frequencies due to the ion hopping between neighboring vacant sites.<sup>[144]</sup> The high frequency range (c) shows a dispersion region where the ac conductivity increases rapidly with the increase of frequencies due to the charge carrier hopping.<sup>[153]</sup> When the temperature changes to low (high) values, a gradual frequency shift is noticed on the overall conductivity curves toward high (low) frequencies. As can be seen in Figure 3.5(b), a peak valley at a certain frequency  $\omega_{on}$  is assigned to the involvement of a space charge density at the electrodes. In parallel, a frequency  $\omega_{max}$  is associated to the position of the peak in  $\sigma''$  where the electrode polarization saturates. To further understand the singular thermal and frequency dependence, we consider the model developed by Khamzin et al.<sup>[154]</sup> which takes into account the contribution of the electrode polarization at low frequencies and high temperatures. In this model, the complex conductivity at low frequencies region is written as follows:

$$\sigma^*(\omega) = \sigma_0 + \frac{\sigma_{dc} - \sigma_0}{1 + (i\omega\tau_2)^{-\beta}} \quad \dots(3.4)$$

where  $\sigma_0$  represents a contribution of the conductivity at a constant electric field and differs from the value of  $\sigma_{dc}$  when the electrode polarization is involved. The relaxation time  $\tau_2$  depends on the process of charge accumulation on the electrode polarization. For the high frequency behavior of the ac conductivity, the modified Almond-West formalism<sup>[143]</sup> was used with the following equation:

$$\sigma' = \sigma_{dc} \left[ 1 + \left( \frac{\omega}{\omega_c} \right)^n \right] + A\omega^m \quad \dots(3.5)$$

where  $\sigma_{dc}$ ,  $\omega_c$ ,  $n$ ,  $m$  represent the dc conductivity, a crossover frequency, and a power law exponent, respectively; the parameter A is a weakly temperature dependent. Based on the equation (3.4) and (3.5), the complex conductivity in the whole frequency region can be expressed as:

$$\sigma'(\omega) = \sigma_0 + \frac{(\sigma_{dc} - \sigma_0)(1 + (\omega\tau_2)^{-\beta} \cos(\frac{\pi}{2}\beta))}{1 + 2(\omega\tau_2)^{-\beta} \cos(\frac{\pi}{2}\beta) + (\omega\tau_2)^{-2\beta}} + \sigma_{dc} \left( \frac{\omega}{\omega_c} \right)^n + A\omega^m \quad \dots(3.6)$$

$$\sigma''(\omega) = \frac{(\sigma_{dc} - \sigma_0)(\omega\tau_2)^{-\beta} \sin(\frac{\pi}{2}\beta)}{1 + 2(\omega\tau_2)^{-\beta} \cos(\frac{\pi}{2}\beta) + (\omega\tau_2)^{-2\beta}} + B\omega^p \quad \dots(3.7)$$

Based on the above model, the simulations of the real and imaginary parts of the complex conductivity spectra are shown in the Figure 3.5(a) and (b). It worth noting

that a good agreement is obtained between the simulation and the experimental conductivity data in the range of 0.01 Hz-1 MHz at low temperatures. However, the increase of the temperature induces a small deviation on the simulation at low frequencies which may originate from the enhancement of the ion migration such as MA<sup>+</sup> cations which requires higher activation energy. The simulation parameters  $\sigma_{dc}$ ,  $\sigma_0$ ,  $\tau$ ,  $\omega_c$ ,  $\beta$ ,  $n$  are summarized in Table 3.2 at different temperatures. At low temperatures, the parameter  $\beta$  fixed to 1 and decreases with increasing the temperature in agreement with the simulation results of the dielectric constants. The crossover frequency  $\omega_c$  from dc to dispersive conductivity region represents the hopping frequency of the charge carriers being thermally activated. The power law exponent  $n$  is larger than unit as also reported in single crystals K<sub>3</sub>H(SeO<sub>4</sub>)<sub>2</sub>, LiFePO<sub>4</sub>, CaCu<sub>3</sub>Ti<sub>4</sub>O<sub>12</sub><sup>[155-157]</sup> where strong Coulomb interactions are involved between the mobile ions and the localized electron states. As  $A\omega^m$  term may originate from the libration of MA<sup>+</sup> at high frequencies, its frequency dependence correlate with that of the  $\varepsilon''(\omega)$  peak.

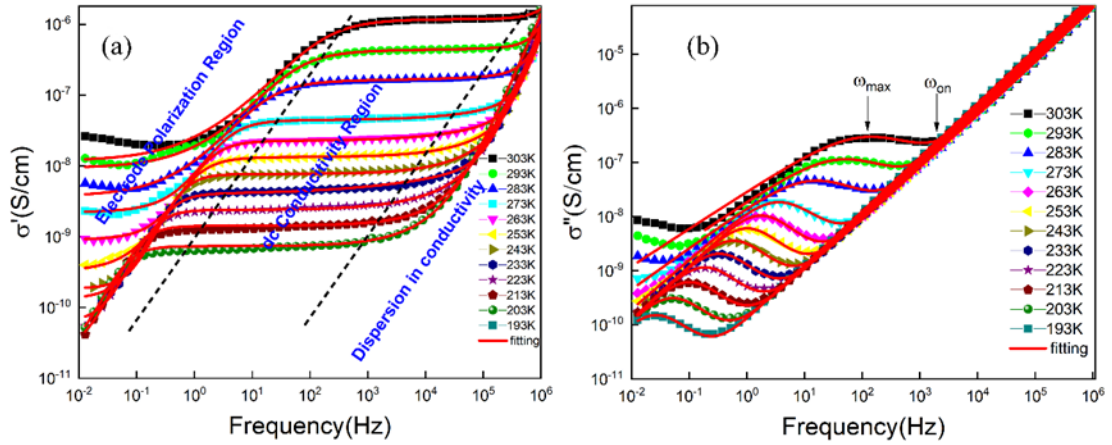


**Figure 3.5** (a) Real and (b) imaginary parts of the complex conductivity spectra at different temperatures in the frequency range 0.01 Hz–1 MHz for MAPbI<sub>3</sub> single crystal. The red solid lines are the best fits to the Eqs. (3.6) and (3.7)

**Table 3.2.** Simulated parameters  $\sigma_{dc}$ ,  $\sigma_0$ ,  $\tau$ ,  $\omega_c$ ,  $\beta$ ,  $n$  used for the adjustment of conductivity components versus temperature and frequency according to equations (3.6) and (3.7).

T(K)	$\sigma_{dc}$ (S/cm)	$\sigma_0$ (S/cm)	$\tau$	$\omega_c$	$\beta$	$n$
303	$1.19 \times 10^{-6}$	$1.23 \times 10^{-8}$	0.001	1448	0.72	3.09
293	$4.30 \times 10^{-7}$	$9.33 \times 10^{-9}$	0.0031	952	0.75	2.52
283	$1.61 \times 10^{-7}$	$3.73 \times 10^{-9}$	0.0096	632	0.76	2.54
273	$4.44 \times 10^{-8}$	$2.20 \times 10^{-9}$	0.0459	377	0.89	2.60
263	$2.25 \times 10^{-8}$	$8.94 \times 10^{-10}$	0.0932	254	0.93	2.45
253	$1.38 \times 10^{-8}$	$4.71 \times 10^{-10}$	0.176	195	1	2.45
243	$8.13 \times 10^{-9}$	$2.11 \times 10^{-10}$	0.284	144	1	2.40
233	$4.70 \times 10^{-9}$	$1.10 \times 10^{-10}$	0.472	76.2	1	2.11
223	$2.61 \times 10^{-9}$	$4.85 \times 10^{-11}$	0.851	49.2	1	1.88
213	$1.42 \times 10^{-9}$	$2.56 \times 10^{-11}$	1.50	24.7	1	2.01
203	$7.36 \times 10^{-10}$	$2.36 \times 10^{-11}$	2.66	21.5	1	2.06
193	$3.66 \times 10^{-10}$	$4.33 \times 10^{-11}$	4.23	16.3	1	1.55

The parameter  $\sigma_0$  represents the electronic conductivity which increases with rising the temperature as it may occur in semiconducting systems. however,  $\sigma_0$  is two orders of magnitude smaller than  $\sigma_{dc}$  which contains contributions from both electronic and ionic conductivity as well. The analysis of the results reported in Table 3.2 indicates that the ionic conductivity represents the main contribution to the dc conductivity. The thermal variation of the dc conductivity with the inverse temperature (Figure 3.6(a)) follows the Arrhenius behavior with the activation energies determined from the negative slope of the plot of  $\ln(T \cdot \sigma_{dc})$  vs.  $1000/T$ . In agreement with the above analysis performed from the Debye model applied to dielectric constants, the plot of Figure 3.6(b) evidences two variation regimes with activation energies of 0.27(5) eV at low temperatures and 0.80(5) eV at high temperatures. Thus, the observed behavior of dc conductivity in MAPbI<sub>3</sub> is similar to that of the ionic conduction in the halides perovskite-type with the formulae CsPbCl<sub>3</sub> or CsPbBr<sub>3</sub><sup>[158-159]</sup> as also reported in polycrystalline hybrid perovskite films<sup>[34]</sup>.

The analysis of the electrical conductivity at low temperatures suggests that the activation energy is just enough to allow the migration of I<sup>-</sup> ions which have a low activation energy comparing with MA<sup>+</sup> ions<sup>[160]</sup>. At high temperatures, the activation energy is large enough to activate the migration of MA<sup>+</sup> ions. The transient capacitance measurements also disclosed the different ionic migration at different temperatures<sup>[37]</sup>. The activation energy at high temperature in the present work study is consistent with the calculated activation energy of MA<sup>+</sup> about 0.84 eV<sup>[35]</sup>. As the ac conductivity in our study is involved along [100], it is reasonable that the migration of MA<sup>+</sup> correlates with the giant dielectric constant at high temperatures. Figure 3.6 (b) shows the inverse temperature dependence of the relaxation time ( $\tau_2$ ). It should be noted that it has a similar behavior as  $\sigma_{dc}$ , the activation energy is a slightly higher than  $\sigma_{dc}$  and shows the same tendency. It suggests that ionic conduction and the relaxation process should be ascribed to ionic movements.

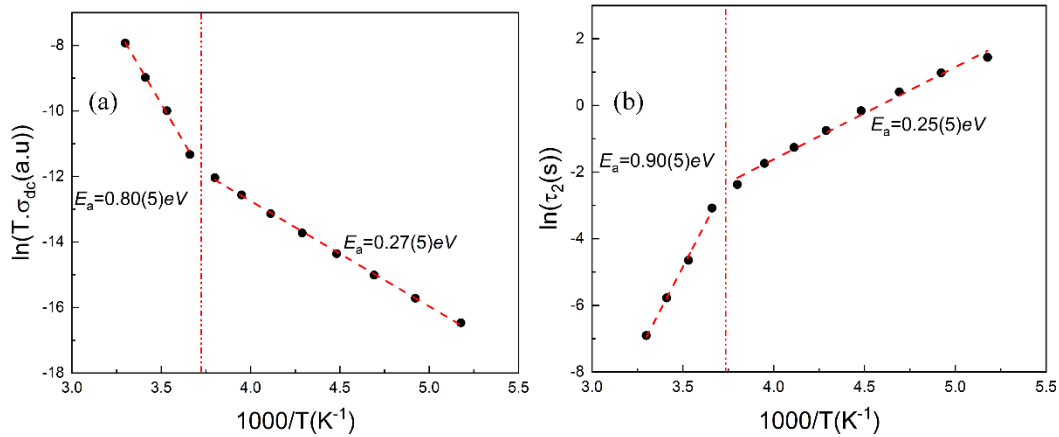


**Figure 3.6** Representation of  $\ln(T \cdot \sigma_{dc})$  vs.  $1000/T$  (a) and relaxation time  $\tau_2$ . (b) in MAPbI<sub>3</sub> single crystal as deduced from dielectric spectroscopy measurements

To better point out the correlation between the dielectric behavior and conductivity, we focus on the frequency dependence of the real part of the dielectric function and the real part of conductivity at two representative temperatures (193 K, 283 K). As depicted in Figure 3.7(a), at the temperature 193 K, the decrease of the dielectric constant in the frequency range (I) is induced by the migration of I<sup>-</sup> ions following an ideal Debye relaxation model. In the frequency range (II), the hopping of the charge carriers has



little influence on the dielectric constant. Figure 3.7(b) shows also the ac conductivity behavior in the region (I) which indicates the ionic migration of MA<sup>+</sup> leading to the sharp decrease of the dielectric constant. For higher temperature 283 K, the decrease of the dielectric constant in the region of (II) follows the modified Cole-Cole model. Based on the above discussion, the change of the model Debye-like at 193 K to modified Cole-Cole at 283 K is due to the enhanced ionic transport resulting from the additional MA<sup>+</sup> ion migration. In the region of (III), the hopping of charge carrier has no contribution to the dielectric constant.

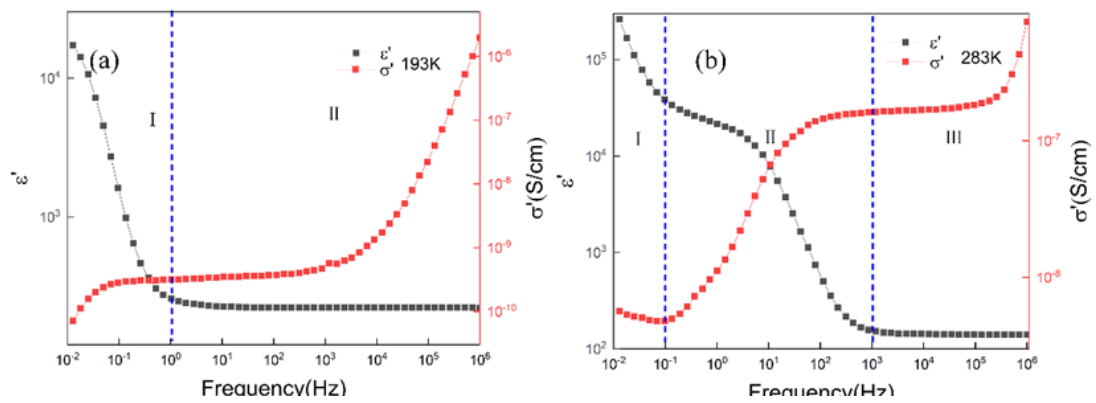


**Figure 3.7** Dielectric constant and ac conductivity as a function of frequency at the temperature (a) 193 K and (b) 283 K

### 3.3.5 The Influence of illumination on the Dielectric Properties of MAPbI<sub>3</sub> Single Crystals

In previous section, it was found that MAPbI<sub>3</sub> single crystal has a giant dielectric effect, and elaborated on the relationship between ion migration and dielectric properties of MAPbI<sub>3</sub>. Emilio et al.<sup>[61]</sup> found that illumination can induce a giant dielectric effect in MAPbI<sub>3</sub> films, and attributed it to structural fluctuations. However, Jie Xing et al.<sup>[34]</sup> found that illumination can significantly change the activation energy of ion migration and lead to greater ion conductivity. Based on the previous discussion, it is reasonable to believe that the change in dielectric constant under illumination is due to the change in ion migration under light. In order to confirm this hypothesis, this work studied the influence of illumination on the dielectric properties of MAPbI<sub>3</sub> single crystal. Figure 3.8 (a) and (b) show the real part and imaginary part of the dielectric

constant with frequency under illumination and dark conditions. It can be seen that the dielectric constant under illumination in the range of  $10^2$  Hz- $10^5$  Hz is larger than the dielectric constant under dark, and it is very close in the range of 10 Hz- $10^2$  Hz, and the dielectric constant under illumination below 10 Hz is also larger than the dielectric constant under dark. The imaginary part of the dielectric constant as a function of frequency shows similar characteristics as the real part of dielectric constant. To explain this phenomenon, the data was fitted based on the previous formula (3.2), the red line is the fitting result, and the fitting parameters are shown in Table 3.3. There is almost no change in  $\epsilon_\infty$  under illumination, which indicates that illumination has no effect on the orientation of  $\text{MA}^+$ . However, both  $\sigma_1$  and  $\sigma_2$  increase significantly under illumination, from  $3.37 \times 10^{-7}$  S/m to  $5.44 \times 10^{-7}$  S/m and  $1.07 \times 10^{-6}$  S/m to  $1.84 \times 10^{-6}$  S/m respectively, which indicates that illumination can not only increase the carrier concentration, but also increase the concentration of localized charges accumulated on the electrode surface. The reason for the increase in localized charges is that illumination can reduce the activation energy of and increase the rate of ion migration. This phenomenon is consistent with the reported in the literature<sup>[34, 161]</sup>. The increase of  $\alpha$  under illumination also indicates that illumination will increase the chaos of the system. The decrease of the relaxation time  $\tau_1$  under illumination indicates that light will promote the ion migration of MAPbI<sub>3</sub>.

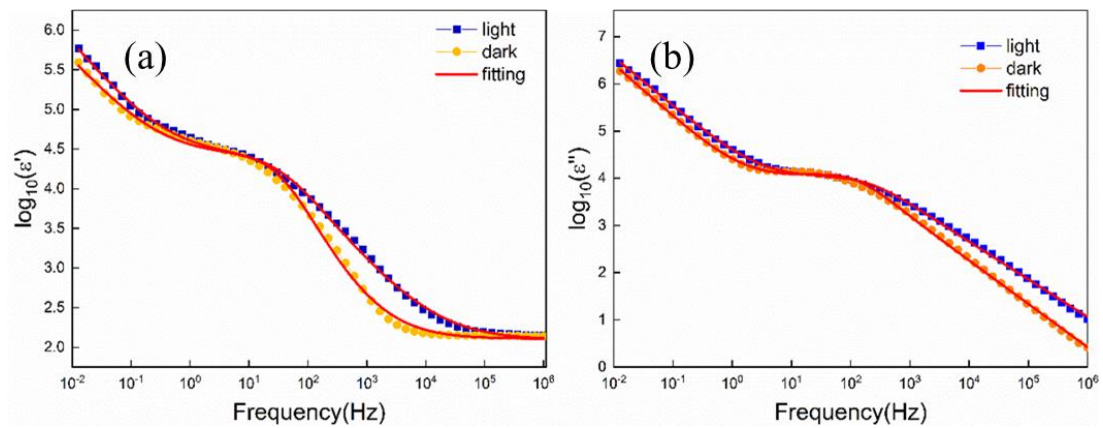


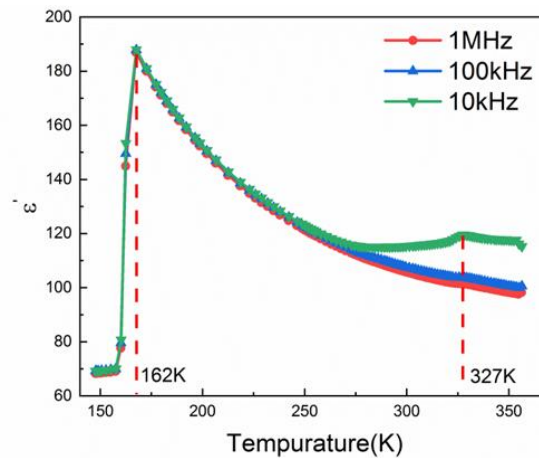
**Figure 3.8** (a) Real and (b) imaginary parts of the dielectric constant under light and dark condition, the continuous red line corresponds to the best fits from equation (3.2)

**Table 3.3** Simulated parameters under light and dark condition according to equation (3.2)

	$\epsilon_s$	$\epsilon_\infty$	s	$\alpha$	$\sigma_1(10^{-7}\text{S/m})$	$\sigma_2(10^{-6}\text{S/m})$	$\tau_1(\text{s})$
dark	27223	138	1	0.115	3.73	1.07	0.0047
light	28765	140	1	0.253	5.44	1.84	0.0039

### 3.3.6 Dielectric temperature spectrum of MAPbI<sub>3</sub>

Since MA<sup>+</sup> is a polar particle with a dipole moment, the orientation change of dipole moment with temperature will be reflected in the change of the dielectric temperature spectrum of the material. Therefore, to study the orientation of MA<sup>+</sup> in the MAPbI<sub>3</sub> crystal, dielectric temperature spectrum of MAPbI<sub>3</sub> has been studied at different frequencies, the results are shown in Figure 3.9. It can be seen that there is a dielectric peak near 162 K, which corresponds to the phase transition from the orthorhombic phase to the tetragonal phase. The phase transition temperature is consistent with the previously reported phase transition temperature [25, 162]. In the tetragonal phase, the dielectric constant decreases with increasing temperature, which indicates that the dipole is disordered. However, in the orthorhombic phase, the dielectric constant is unchanged with frequency, which may be due to the anti-parallel arrangement of MA<sup>+</sup>. The slight change in the dielectric constant at 327 K corresponds to the phase transition from tetragonal to cubic phase, but there is no obvious dielectric peak, which indicates that the phase transition from tetragonal to cubic phase is not the phase transition from ferroelectric to paraelectric phase.

**Figure 3.9** Temperature dependence of dielectric constant of MAPbI<sub>3</sub> at different frequency

Based on the above discussion, the Kirkwood–Fröhlich–Onsager theory can be used to analyze the temperature characteristics of the dielectric constant. This theory was first used to describe the relationship between the dipole moment and the dielectric constant in polar liquids. The Kirkwood–Fröhlich–Onsager formula is as follows<sup>[58]</sup>:

$$\frac{(\epsilon_r - \epsilon_{r\infty})(2(\epsilon_r + \epsilon_{r\infty}))}{\epsilon_r(\epsilon_{r\infty} + 2)^2} = \frac{1}{9\epsilon_0} g \frac{N\mu^2}{k(T - T_c)} \quad \dots(3.8)$$

Where  $\epsilon_r$  is the dielectric constant at low frequencies,  $\epsilon_{r\infty}$  is the dielectric constant at high frequencies,  $g$  is the Kirkwood correlation coefficient,  $N$  is the dipole density,  $\mu$  is the dipole moment, and  $k$  is the Boltzmann constant,  $T$  is the absolute temperature, and  $T_c$  is the Curie-Weiss temperature. The phenomenon that dielectric constant is proportional to  $1/(T - T_c)$  is common in perovskite materials<sup>[163]</sup>. The correlation coefficient  $g$  is closely related to the interaction between the independent dipoles in the system. It can be expressed by the following formula:

$$g = \frac{\langle \sum_i \mu_i \sum_j \mu_j \rangle}{N\mu^2} = 1 + \frac{\langle \sum_i \sum_{i < j} \mu_i \mu_j \rangle}{N\mu^2} \quad \dots(3.9)$$

where  $\mu_i$  represents the dipole moment of the independent dipoles. When  $g$  is larger than unit, the dipoles are arranged in parallel, when the value is less than unit, the dipoles are arranged in anti-parallel. Figure 3.10 shows the fitting result of the dielectric constant of MAPbI<sub>3</sub> single crystal at 1 MHz in the tetragonal phase according to the Kirkwood–Fröhlich–Onsager formula, where  $T_c$  is 34.4 K and  $\epsilon_{r\infty}$  is 32.4. According to previous literature reports, the dipole density  $N$  is  $4.01 \times 10^{27} \text{ m}^{-3}$ <sup>[164]</sup>. The dipole moment of MA<sup>+</sup> ions calculated by DFT is  $6.68 \times 10^{-30} \text{ Cm}$ <sup>[163, 165]</sup>. The fitted  $gN\mu^2/9\epsilon_0k = (9.51 \pm 0.05) \text{ K}$ , the  $g$  value can be calculated to be 0.06, which is much lower than the 0.11 obtained in the films reported in the previous article<sup>[58]</sup>, when  $g < 1$  indicates that the MA<sup>+</sup> in MAPbI<sub>3</sub> is in an anti-parallel. This result is consistent with the previous theoretical calculation results<sup>[60, 166-167]</sup>.

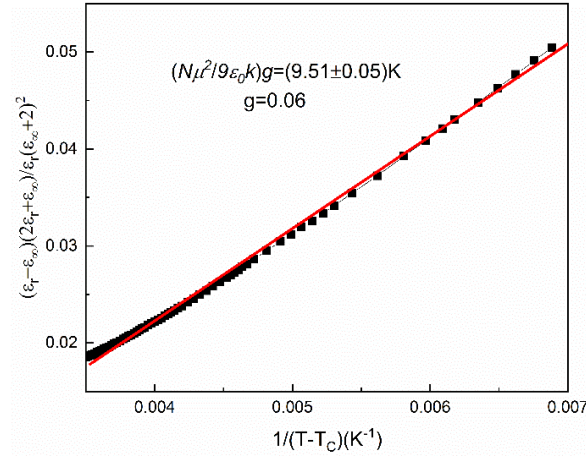


**Figure 3.10** Fitting of the MAPbI<sub>3</sub> single crystal dielectric constant to Kirkwood–Fröhlich–Onsager equation over the temperature range for the tetragonal phase

### 3.4 Effect of Cs<sup>+</sup> doping on the dielectric properties of MAPbI<sub>3</sub>

Since MAPbI<sub>3</sub> is easily decomposed under the influence of moisture, Cs<sup>+</sup> is often used as a doping element to improve the stability of MAPbI<sub>3</sub>. Hyosung Choi et al.<sup>[168]</sup> found that Cs<sup>+</sup> doping can increase the efficiency of perovskite solar cell by 40%, and appropriate amount of Cs<sup>+</sup> doping can increase the light absorption coefficient and change the band gap of MAPbI<sub>3</sub>. Ankur Taya et al.<sup>[169]</sup> investigated the crystal structure, electronic structure, and optical properties of Cs<sup>+</sup> doped MAPbI<sub>3</sub> through first-principles calculations. Studies have found that Cs<sup>+</sup> doping will reduce the hydrogen bonds in MAPbI<sub>3</sub>, and the reduction of hydrogen bonds will increase the tilt angle of the octahedron, thereby improving the stability of the system and increasing the band gap of MAPbI<sub>3</sub>. However, Cs<sup>+</sup> is a non-polar particle, and the replacement of MA<sup>+</sup> will inevitably affect the dielectric properties of MAPbI<sub>3</sub> and the movement of MA<sup>+</sup>. In order to study the effect of Cs<sup>+</sup> doping on the dielectric properties of MA<sup>+</sup>, we prepared Cs<sup>+</sup> doped powders by solvent evaporation method, and pressed the powders into pellets, which were then annealed in an oven and coated with electrodes to measure their dielectric properties.

#### 3.4.1 Effect of Cs<sup>+</sup> doping on the structure of MAPbI<sub>3</sub>

Figure 3.11 shows the XRD pattern of Cs<sup>+</sup> doped MAPbI<sub>3</sub> powder. When the doping amount is 5% and 10%, no impurity peak appears. When the doping amount is

15%, an impurity peak appears, which belongs to CsPbI<sub>3</sub><sup>[168]</sup>. From the enlarged view of the (002) peak, it can be seen that with the increase of the doping amount, the (002) peak shifts to a low angle, which indicates that the lattice parameter *c* increases with the increase of the doping amount.

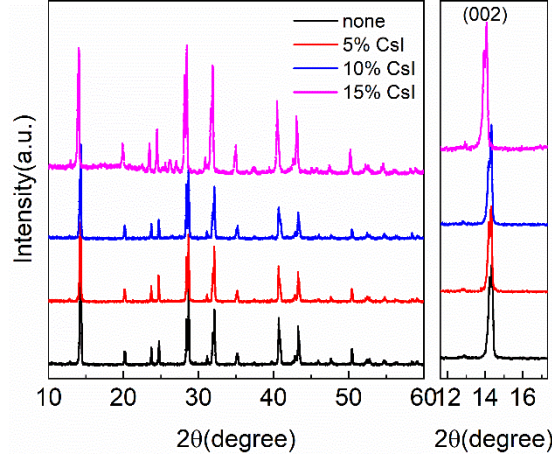


**Figure 3.11** XRD patterns of Cs<sup>+</sup> doped MAPbI<sub>3</sub>

### 3.4.2 Effect of Cs<sup>+</sup> doping on the optical properties of MAPbI<sub>3</sub>

Figure 3.12 shows the absorption spectra and corresponding band gap of Cs<sup>+</sup> doped MAPbI<sub>3</sub>. It can be seen that with the increase of Cs<sup>+</sup> doping, its absorption spectrum does not change significantly, but the absorption edge shifts slightly to the right. For semiconductor materials, the relationship between absorption coefficient and optical band gap can be expressed in the formula:<sup>[170-171]</sup>

$$\alpha(h\nu) = A(h\nu - E_g)^m \quad \dots(3.10)$$

Where  $\alpha$  is the light absorption coefficient,  $h$  is the Planck constant,  $\nu$  is the frequency of light,  $A$  is the proportionality constant, and  $E_g$  is the optical band gap of the semiconductor. For direct band gap materials,  $m=1/2$ , for indirect band gap materials,  $m=2$ . MAPbI<sub>3</sub> is the direct band gap,  $m=1/2$ <sup>[27, 172]</sup>. Figure 3.12(b) shows the  $(\alpha h\nu)^2$  as a function of wavelength according to formula (3.10). The intercept corresponding to the tangent in the figure is the band gap of MAPbI<sub>3</sub>. The band gap of Cs<sup>+</sup> doped MAPbI<sub>3</sub> is shown in Figure 3.13. As the doping amount of Cs<sup>+</sup> increases, the band gap gradually increases, which is consistent with the results reported in the literature<sup>[169]</sup>.

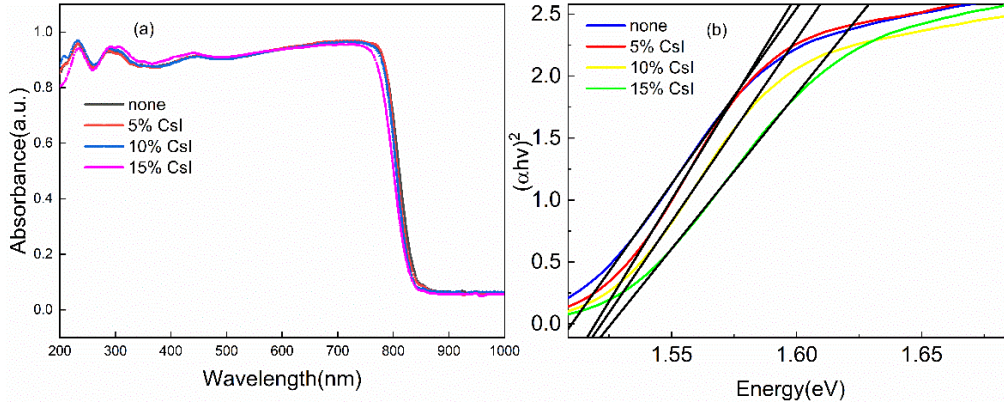


**Figure 3.12** (a) Absorbance spectra and (b) band gap of the Cs<sup>+</sup> doped MAPbI<sub>3</sub>

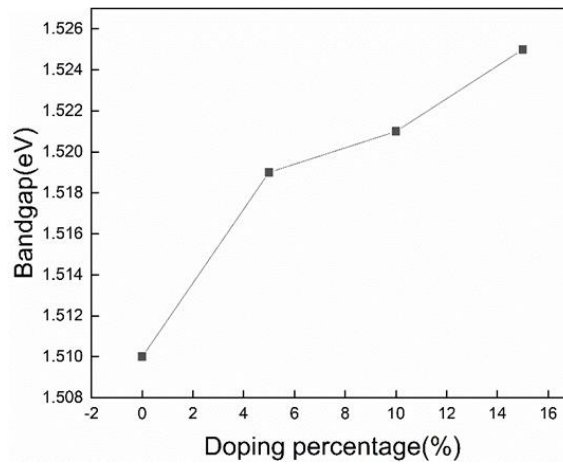


**Figure 3.13** The band gap of Cs<sup>+</sup> doped MAPbI<sub>3</sub>

### 3.4.3 Effect of Cs<sup>+</sup> doping on the dielectric properties of MAPbI<sub>3</sub>

Figure 3.14 shows the dielectric temperature spectrum of Cs<sup>+</sup> doped MAPbI<sub>3</sub> at 1 MHz (Because there are impurity phases when the Cs<sup>+</sup> doping amount is 15%, the effect of this doping on properties is not discussed). Pure MAPbI<sub>3</sub> has a sharper dielectric peak at 163 K. When the Cs<sup>+</sup> doping amount is 5%, the dielectric peak appears near 180 K, and the peak shape is relatively smooth. When the doping amount is 10%, the dielectric peak appears near 183 K. Since this peak corresponds to the phase transition from the orthorhombic phase to the tetragonal phase of MAPbI<sub>3</sub>, the increase of the phase transition temperature indicates that the stability of MAPbI<sub>3</sub> has been further improved after the doping of Cs<sup>+</sup>. In order to study the effect of Cs<sup>+</sup> doping on the orientation of MA<sup>+</sup>, the fitting results obtained by Kirkwood–Fröhlich–Onsager theory are shown in Figure 3.15. The  $g$  value is 0.144 for pure MAPbI<sub>3</sub>, which is higher than that of single



crystals. This may be due to the defects inside the pellets, the anti-parallel arrangement of MA<sup>+</sup> is destroyed. When doped with 5% and 10% Cs, the corresponding  $g$  values are 0.082 and 0.083. Compared with the undoped samples, the  $g$  values are smaller, which shows that Cs<sup>+</sup> doping can enhance the anti-parallel arrangement of MA<sup>+</sup>.

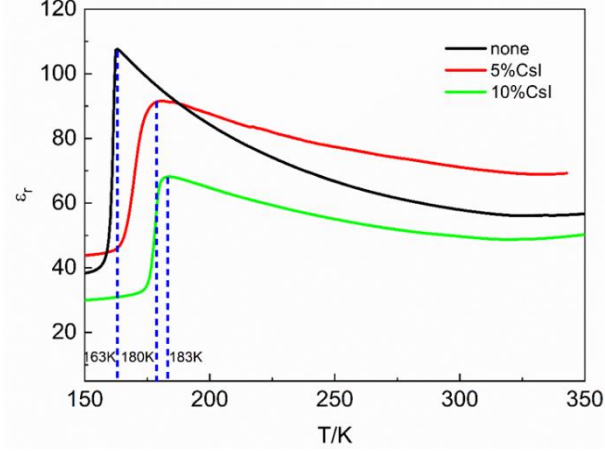


**Figure 3.14** Temperature dependent dielectric constant of the Cs<sup>+</sup> doped MAPbI<sub>3</sub>

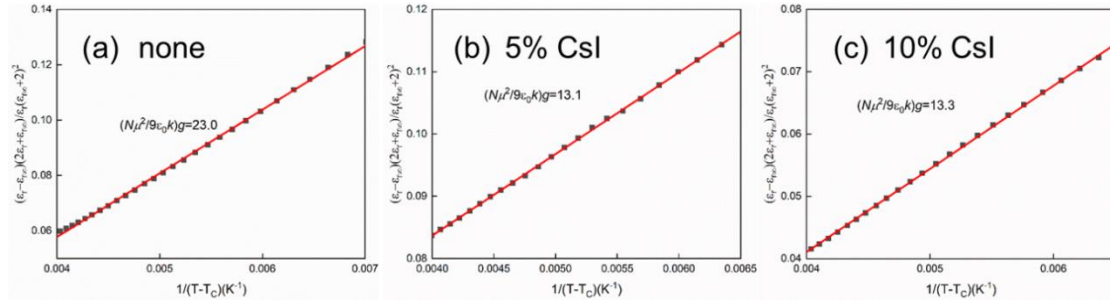


**Figure 3.15** Fitting of the Cs<sup>+</sup> doped MAPbI<sub>3</sub> dielectric constant to Kirkwood–Fröhlich–Onsager equation

### 3.5 Conclusion

The dielectric behavior and electrical conductivity of MAPbI<sub>3</sub> single crystal were investigated as function of the frequency in the range [0.01 Hz, 1 MHz] and for the temperatures  $193 \leq T \leq 303$  K. The giant dielectric constant realized at low frequencies and at high temperatures is induced by the ionic migration which may involve both methylamine MA<sup>+</sup> cations and iodide I<sup>-</sup> anions. Additional vacancies are thermally created at high temperatures and the long-range movements of ions will favor their



accumulation leading to the space charge density at the interface between the crystal (001) and the Ag electrodes. At intermediate frequencies, hopping of ions is characterized by Debye-like relaxation while at high frequencies the dipole relaxation of MA<sup>+</sup> has small contribution to the dielectric constant. The present results are used to explain the abnormal dielectric properties which were pointed out in MAPbI<sub>3</sub> films with the giant dielectric constant under the light and give exhaustive insights on the process of ionic transport in the hybrid perovskite structure.

The dielectric temperature spectrum of the MAPbI<sub>3</sub> crystal shows that the material has a dielectric peak at 162 K. The peak corresponds to the phase transition from the orthorhombic phase to the tetragonal phase. The dielectric constant changes slightly at 327 K, which indicates that the phase transition from the tetragonal phase to the cubic phase is not the phase transition of ferroelectric phase to paraelectric phase. According to the Kirkwood–Fröhlich–Onsager theory, the fitting results show that MA<sup>+</sup> is in anti-parallel arrangement in the orthorhombic phase, and the dielectric constant does not change with temperature. In the tetragonal phase, the anti-parallel arrangement of MA<sup>+</sup> gradually breaks and shows obvious temperature characteristics. After Cs<sup>+</sup> doping, the optical band gap of MAPbI<sub>3</sub> is changed. According to dielectric temperature spectrum of Cs<sup>+</sup> doped MAPbI<sub>3</sub>, it can be found that Cs<sup>+</sup> doping significantly improves the temperature stability of MAPbI<sub>3</sub> and promotes the anti-parallel arrangement of MA<sup>+</sup> at the same time.



## Chapter 4 Tetragonal to cubic phase transition of MAPbI<sub>3</sub>

### 4.1. Introduction

Although many reports were devoted to the basic properties of methylammonium lead iodide perovskite (MAPbI<sub>3</sub>), there are still many open problems remaining unsolved. There are three different phases for MAPbI<sub>3</sub> at different temperature, below 162 K it is orthorhombic structure; above 327 K it is cubic structure; between 162 K and 327 K, it is tetragonal structure. Due to the low temperature of phase transition of MAPbI<sub>3</sub> which is at the working temperature of perovskite solar cell, several investigations were dealing with the phase transition of tetragonal to cubic phase. According to the thermal evolution of the order parameter,<sup>[120]</sup> the phase transition is considered as the first order. However, from neutron powder diffraction experiments, it was shown that a second order character hold for this phase transition.<sup>[25]</sup> Using the single crystal X-ray diffraction, the critical behavior was investigated. Single crystal X-ray diffraction and neutron powder diffraction were used to investigate the space group of MAPbI<sub>3</sub> to confirm whether it is centrosymmetric. But the results are contradictory in the way that the space group of  $I4/mcm$ <sup>[25]</sup> (centrosymmetric),  $I4cm$ <sup>[97]</sup> (non-centrosymmetric) and  $I422$ <sup>[173]</sup> were reported at the room temperature. Raman spectroscopy is very useful for studying the phase transition and lattice dynamics. Although, the high power of laser beam will generate some burning effect on MAPbI<sub>3</sub>,<sup>[174]</sup> the Raman spectroscopy is useful for the structural features and their evolution at the phase transition.

Herein, investigations of X-ray powder diffraction (XRD) and Raman spectroscopy were carried out to understand the structure change of MAPbI<sub>3</sub> at the phase transition of tetragonal to cubic phase. The XRD pattern of single crystal and ground powder of single crystal are studied. The refinement of XRD pattern of tetragonal to cubic phase were investigated to deeply understand the structure change.

### 4.2 Tetragonal to cubic phase transition of MAPbI<sub>3</sub>

Using high-resolution X-ray diffractometer, the diffraction pattern of MAPbI<sub>3</sub>

powder in the tetragonal phase (30 °C) and cubic phase (70 °C) are shown in Figure 4.1. According to the calculated X-ray diffraction parameters shown in Table 4.1 and 4.2, it can be judged that the diffraction peaks at 23.43° and 24.43° at 30 °C correspond to the (211) crystal plane and (202) crystal plane of the tetragonal phase, respectively. At 70 °C, the tetragonal phase transforms into cubic phase, the characteristic peak (211) of the tetragonal phase disappears, and the peak of the tetragonal phase (202) transforms into a (111) peak of cubic phase.

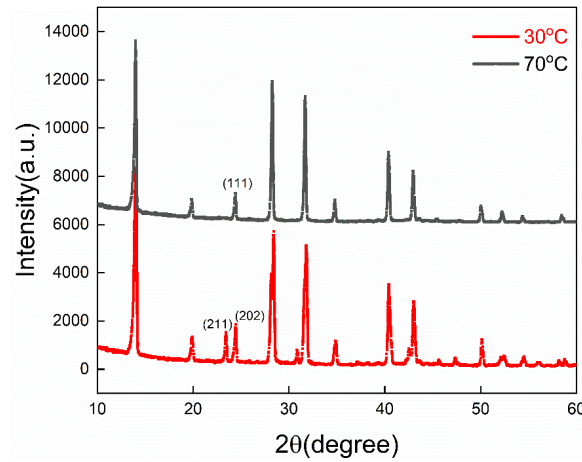


**Figure 4.1** Powder X-ray diffraction pattern of MAPbI<sub>3</sub> for tetragonal phase (30 °C) and cubic phase (70 °C)

**Table 4.1** Calculated X-ray diffraction parameters of tetragonal MAPbI<sub>3</sub>

Index	2θ(°)	d-spacing(Å)	Relative (%)	Multiplicity
002	13.94	6.34	56	2
110	14.15	6.25	100	4
112	19.92	4.45	9	8
200	20.07	4.42	11	4
211	23.55	3.77	23	16
202	24.52	3.63	14	8
004	28.09	3.17	42	2
220	28.54	3.12	59	4
213	30.93	2.88	10	16
114	31.59	2.83	29	8
222	31.89	2.80	22	8
310	31.99	2.79	45	8

**Continued Table 4.1** Calculated X-ray diffraction parameters of tetragonal MAPbI<sub>3</sub>

Index	2 $\theta$ (°)	d-spacing(Å)	Relative (%)	Multiplicity
204	34.77	2.57	6	8
312	35.04	2.55	12	16
321	37.32	2.40	2	16
224	40.47	2.23	37	8
400	40.80	2.21	13	4
215	42.27	2.14	3	16
323	42.58	2.12	1	16
006	42.70	2.11	2	2
411	42.74	2.11	9	16
314	43.08	2.09	34	16
402	43.31	2.08	5	8
330	43.51	2.08	1	4
116	45.20	2.00	1	8
420	45.87	1.97	4	8
413	47.50	1.91	6	16
404	50.27	1.81	12	8
325	51.79	1.76	1	16
226	52.16	1.75	3	8
431	52.19	1.75	2	16
334	52.49	1.74	2	8
510	52.76	1.73	4	8
316	54.33	1.68	2	16
424	54.66	1.67	5	16
512	54.85	1.67	1	16
217	55.71	1.64	1	16
415	56.10	1.63	2	16
433	56.35	1.63	1	16
008	58.07	1.58	3	2
440	59.07	1.56	3	4

**Table 4.2** Calculated X-ray diffraction parameters of cubic MAPbI<sub>3</sub>

Index	2 $\theta$ (°)	d-spacing(Å)	Relative (%)	Multiplicity
100	14.02	6.31	100	4
110	19.92	4.46	3	4
111	24.46	3.64	14	8
200	28.25	3.15	62	4
210	31.67	2.82	27	8
211	34.78	2.57	10	16
220	40.38	2.23	16	4
221	42.95	2.10	10	8
300	43.06	2.10	1	4
310	45.40	1.99	0.7	8
311	47.87	1.90	0.1	16
222	50.00	1.76	11	8
320	52.21	1.75	2	8
321	54.34	1.68	2	16
400	58.44	1.57	3	4

Since the (211) peak is the characteristic peak of the tetragonal phase, the diffraction peak in the range of 23°-32° changes with the temperature as shown in Figure 4.2(a), and the (211) peak gradually weakens and disappears as the temperature rises. In order to study the changes of the MAPbI<sub>3</sub> lattice parameters during the phase transition, the XRD results were refined using the software MAUD according to the Rietveld method. The refined results at 30 °C are shown in Figure 4.2(b). The refined lattice parameters change with temperature as shown in Figure 4.3. The lattice parameter *a* gradually increases with the temperature, and there is a sudden change around 59 °C, and then gradually increases again with the temperature rise. The lattice parameter *c* gradually decreases as the temperature rises, and there will also a sudden change around 59 °C, and then a decrease again. However, after 59 °C, there are still some differences between the refined lattice parameters *a* and *c*, which indicates that

even if the temperature is higher than the phase transition temperature, there is still lattice distortion. The lattice parameter changes with temperature during the heating and cooling process as shown in Figure 4.4. There is no difference in the lattice parameter during the heating and cooling process, which indicates that there is no thermal hysteresis during the phase transition, and the phase transition is second order.

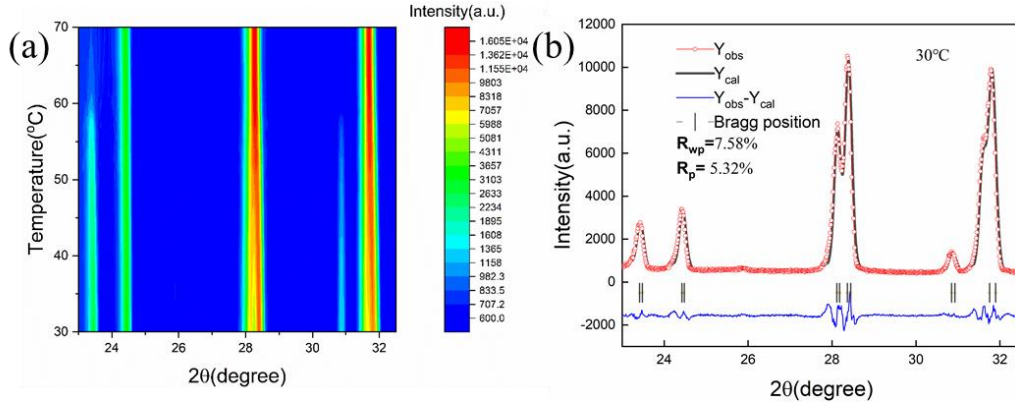


**Figure 4.2** (a) Color map of XRD as a function of temperature and (b) Rietveld refinements at 30 °C for MAPbI<sub>3</sub>

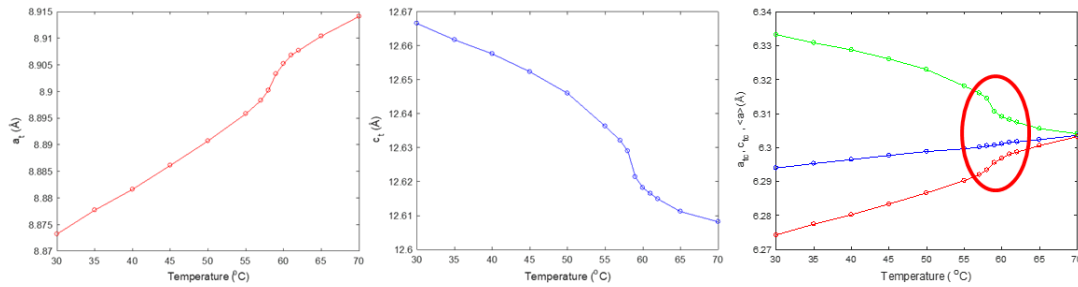


**Figure 4.3** Evolution of lattice parameters versus temperature

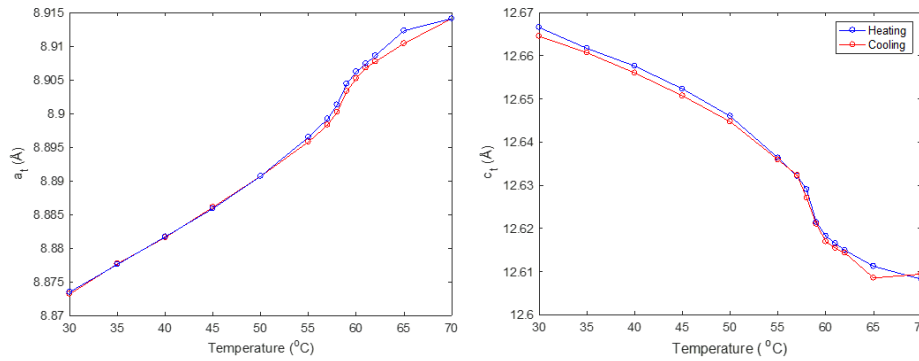


**Figure 4.4** Evolution of lattice parameters versus temperature during the cooling and heating process

The change from the tetragonal phase to the cubic phase is mainly due to the rotation of the PbI<sub>6</sub> octahedra. There is a small angle between the Pb atom at the center of the octahedra and the I atom at the common vertex in the tetragonal phase. As the temperature increases, PbI<sub>6</sub> octahedra rotates, and the Pb atom at the center of the two octahedrons in the cubic phase is collinear with the I atom at the common vertex, and the angle will be zero. According to the calculation of the structure factor, the intensity of the tetragonal (211) peak is closely related to the rotation of the octahedra and the position  $x$  of the iodine atom. The relationship between the two can be expressed by the following formula:

$$I = K(\cos(2\pi x) - \cos(6\pi x))^2 \quad \dots(4.1)$$

Where  $x=0.25+u$ ,  $u$  represents the deviation of the iodine atom from the cubic phase position in the tetragonal phase. The shift of the iodine atoms from the cubic phase positions can be calculated according to the change of the (211) peak intensity with temperature. The value of  $u$  can be calculated according to rotation angle of PbI<sub>6</sub> octahedra, and the change of the rotation angle with temperature is shown in Figure 4.5. The rotation angle plays the role of order parameter for the phase transition and then its temperature variation can be expressed by the following formula<sup>[95]</sup>:

$$\phi \propto (T_c - T)^\beta \quad \dots(4.2)$$

where  $T_c$  represents the phase transition temperature. The fitted  $T_c$  is 61.6 °C, and the index  $\beta$  is 0.26. The octahedral rotation angle can be used as the order parameter from the tetragonal phase to the cubic phase. When the phase transition is a second-order phase transition, the index  $\beta$  is 0.5 which is different from the fitting result. The possible reasons are as follows: 1. The phase change is in a critical state similar to SrTiO<sub>3</sub>, and its index is 1/3; 2. The phase change occurs at the tricritical point and the index is 1/4; 3. The phase change seems then with the character of a first-order phase transition.



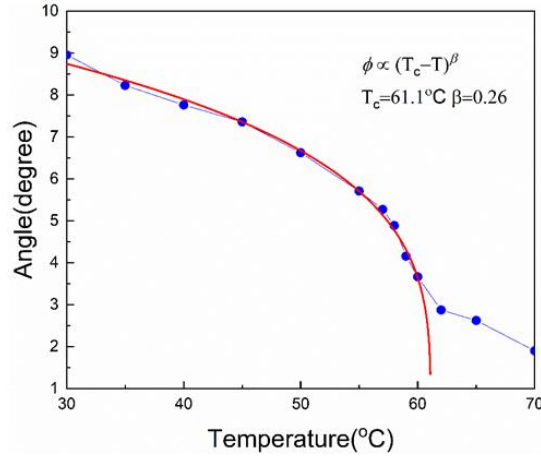
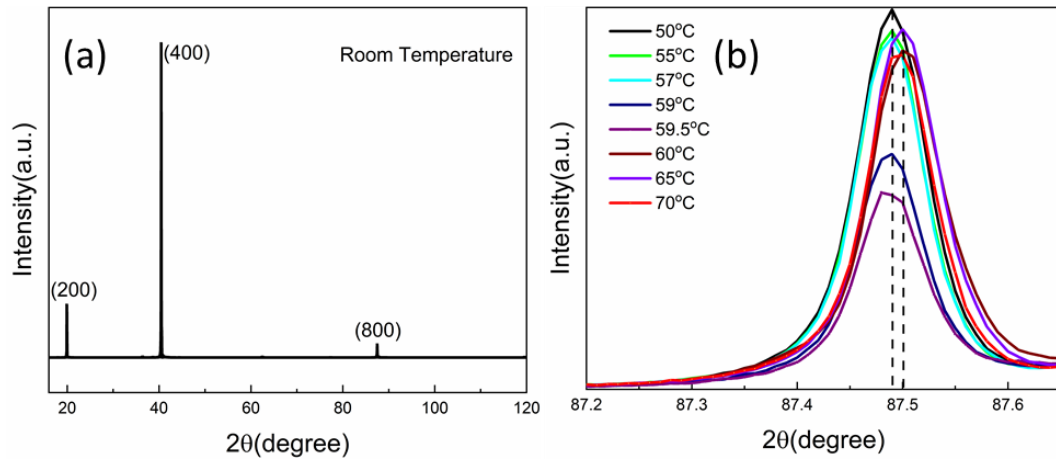


**Figure 4.5** The temperature dependence of the rotation angle of the octahedra

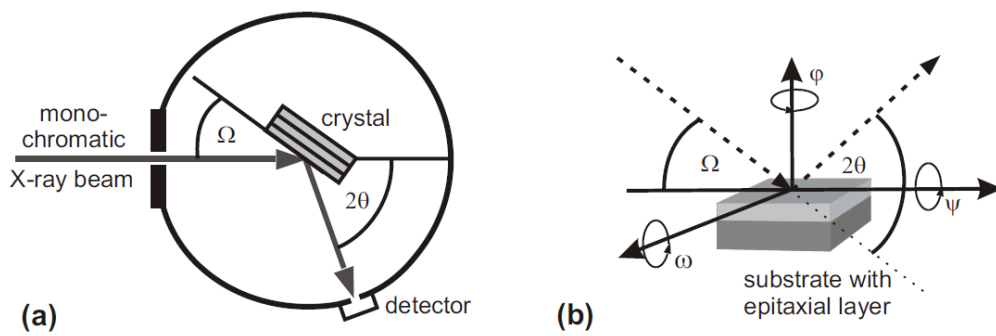
### 4.3 Pretransitional effect of MAPbI<sub>3</sub> single crystal

Figure 4.6 (a) and (b) show the XRD diffraction pattern of (100) plane of MAPbI<sub>3</sub> single crystal at room temperature and the variation of (800) plane diffraction intensity with temperature, respectively. From Figure 4.6(b), it can be seen that the position of the diffraction peaks on the (800) plane at 50 °C-57 °C is unchanged, and the intensity of the diffraction peaks around 59 °C and 59.5 °C decreases significantly. At 60 °C, there is a sudden change in the position of the peak, which indicates that the lattice parameters have changed significantly at 60 °C. When the temperature is further increased, the position of the MAPbI<sub>3</sub> diffraction peak don't show any noticeable change and suggest that the lattice parameters do not change with the temperature. however, no consistent explanation has been found for this phenomenon. For most materials, due to the existence of thermal expansion effect, the lattice parameter will increase with increasing the temperature. In order to further investigate the specific changes in the phase transition process, the  $\Omega$  scan mode was examined. Figure 4.7 shows a schematic diagram of a high-resolution X-ray diffractometer and various rotation modes.  $\Omega$  scan refers to the mode in which the sample rotates along the  $\omega$  axis. In this scan mode, the different crystal plane orientations that may exist on the surface of the sample can be effectively distinguished. Figure 4.8 shows the diffraction intensity of the (437) plane at different temperatures in the omega scan mode. It can be seen that only one diffraction peak appears at 58 °C-59 °C. However, there are three diffraction

peaks at 60 °C and 60.5 °C which merges into one again in the range 60.5-62 °C. This phenomenon is called pretransitional effect<sup>[175]</sup>. Figure 4.9 is a two-dimensional schematic diagram of the tetragonal phase crystal lattice and the cubic phase crystal lattice. For single crystal materials, when the temperature is lower than the phase transition temperature, the lattice parameter  $c$  of the tetragonal phase will be formed along the  $\langle 100 \rangle$  direction of any cubic phase. Different domain structure will be formed. And there will be three different diffraction peaks. This phenomenon was also confirmed by Mathias Uller Rothmann<sup>[98]</sup> by high-resolution TEM.



**Figure 4.6** MAPbI<sub>3</sub> single crystal (a) XRD pattern of (100) plane at room temperature. (b) the intensity of (800) plane at different temperature



**Figure 4.7** (a) HRXRD diffractometer. (b) Illustration of the Euler angles and the angles  $\Omega$  and  $2\theta$

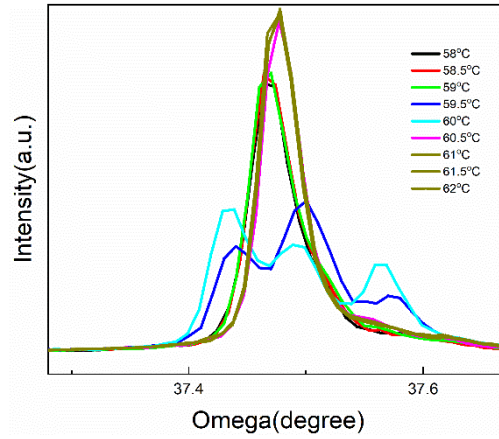


**Figure 4.8** Diffraction intensity of (437) plane at different temperature under omega scan

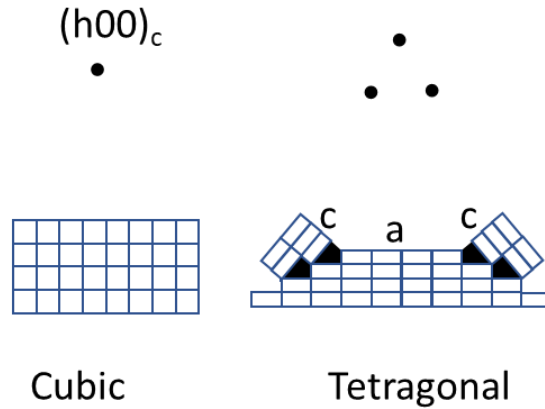


**Figure 4.9** (a) A two-dimensional representation of the cubic-phase lattice. (b) A two-dimensional representation of the tetragonal-phase lattice

#### 4.4 Raman spectroscopy analysis of tetragonal to cubic phase transition

Raman spectroscopy is a sensitive technique to the lattice dynamics and phase transition. In order to deeply understand the phase transition of tetragonal to cubic phase, the Raman Spectroscopy was used with the excitation wavelength of 532 nm to record the spectra at the temperature between 20 °C ~120 °C (figure 4.10). The Raman spectra at 20 °C ~50 °C and 60 °C ~120 °C originate from the tetragonal and cubic phase, respectively. The two peaks located at 95 cm<sup>-1</sup> and 110 cm<sup>-1</sup> at 20 °C are related to the degradation of MAPbI<sub>3</sub> resulting from the tremendous amount of heat released by the laser<sup>[174, 176]</sup>. The intensity of the Raman band is related quantitatively to the amount, distribution and degree of crystallization of the material<sup>[177]</sup>. The intensity of the two

bands located at 95 cm<sup>-1</sup> and 110 cm<sup>-1</sup> decreases sharply at 40 °C compared to that at 20 °C which indicates there is reversible degradation of MAPbI<sub>3</sub><sup>[178]</sup>. Although there are a lot of publications investigating the Raman spectroscopy<sup>[179-181]</sup>, it is the first time that the peaks located at around 80 cm<sup>-1</sup> and 137 cm<sup>-1</sup> are found which is evidently related to the tetragonal to cubic phase transition. The intensity of peaks increases first with the increase of temperature between 40 °C and 54 °C, and after 54 °C the intensity of peaks decreases with the increase of temperature. It has the similar tendency as the intensity change of XRD peaks with the increase of temperature. According to the results of lattice dynamic calculations using the density functional theory (DFT)<sup>[179]</sup>, Raman bands below 200 cm<sup>-1</sup> is mainly related to the lattice vibration, whereas the bands above 400 cm<sup>-1</sup> are attributed to intramolecular vibrations of MA. However, according to calculation results by Ivanovska<sup>[182]</sup>, the peaks located at around 80 cm<sup>-1</sup> and 137 cm<sup>-1</sup> should be assigned to the vibration of organic groups which may affect the phase transition.

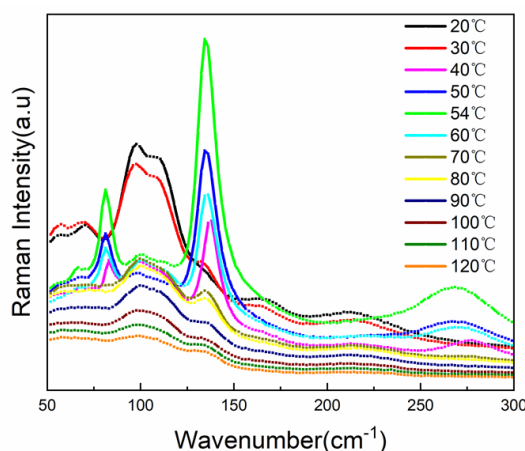


**Figure 4.10** Raman Spectroscopy of single crystal at different temperature

## 4.5 Conclusions

The XRD study of the tetragonal phase to the cubic phase shows that the phase transition from the tetragonal phase to the cubic phase of MAPbI<sub>3</sub> occurs at around 59 °C. There is no obvious difference in the lattice parameters between the heating process and the cooling process indicating that it is the second-order phase transition. (211) as the characteristic peak of the tetragonal phase, its strength gradually decreases

with the increase of temperature, and its strength is related to the rotation angle of the octahedra. The change of rotation angle with temperature indicates that the phase transition is not purely a second-order phase transition. By studying the  $\Omega$  scan mode, it is found that the single crystal has a pre-phase transition effect near 59 °C. The Raman results show that there are two vibration peaks of organic groups near the phase transition, indicating that the organic groups may have an influence on the phase transition.



## Chapter 5 Poling effect on the electrostrictive and piezoelectric response of MAPbI<sub>3</sub> single crystals

### 5.1 Introduction

Organic-inorganic hybrid perovskites (OIHPs) are attractive materials with promising properties in the context of a green energy provided by photovoltaic devices. Beyond, the excellent performance in perovskites solar cells, methylammonium lead triiodide perovskites (MAPbI<sub>3</sub>) exhibit also large electrostrictive coefficients ( $M$ ) in the order of  $-730 \text{ nm}^2\text{V}^{-2}$  which are potentially promising for applications in actuators and micro-electromechanical system<sup>[80]</sup>. The electrostrictive response in each sample depends on its deformation under an applied electrical field. It represents a fundamental electromechanical coupling between the deformation and the square of the applied electric field in contrast to the inverse piezoelectric phenomenon which is a first order effect. For most materials, the electrostrictive response is smaller than the piezoelectric response and the electrostriction coefficients depend on the relative dielectric permittivity and inversely on the Young modulus. Thus, important electrostrictive effects occur in relaxor ferroelectrics and polymers with large dielectric constants<sup>[67, 70, 77]</sup>. For materials with dielectric constant  $\epsilon \approx 20$ , typical electrostriction strain coefficients are about  $M > -1 \text{ nm}^2\text{V}^{-2}$ <sup>[77]</sup>. The situation is quite different in MAPbI<sub>3</sub> with a dielectric constant around 150 and a large electrostriction coefficient up to  $-49.3 \text{ nm}^2\text{V}^{-2}$  compared to the relaxor ferroelectrics or polymers. A similar behavior of a large electrostriction was reported in (Y, Nb)-Stabilized  $\delta$ -Bi<sub>2</sub>O<sub>3</sub> and Gd-Doped Ceria with the origin supposed to occur from defects such as anion vacancies<sup>[77]</sup>. In similar conditions, due to the ion migration in MAPbI<sub>3</sub>, the ion drift under the electric field may generate the formation of defects such as  $V_I'$ ,  $V_{Pb}^\bullet$  or  $V_{MA}^\bullet$  which are characterized by low formation energies<sup>[38, 44, 52]</sup>. As the electrical poling contributes to the selective mobility of  $MA^+$ ,  $I^-$  and  $Pb^{2+}$  ions in MAPbI<sub>3</sub> samples, we expect that the electrostrictive response may be also enhanced by this process as it was discussed in our former reported contribution on the dielectric parameters<sup>[183]</sup>. The present chapter

is devoted to the investigations of the electrostrictive and piezoelectric responses in MAPbI<sub>3</sub> crystals after the ac poling and dc poling. An in-depth analysis of the obtained results was carried out with the aim to correlate the poling effect with the electrically induced defects and the resulting electrostriction and piezoelectricity responses. The theoretical development of the electrostriction effect along with the instrumentation required for evaluating the relevant coefficients were introduced in the chapter 2. A complement of these may be outlined briefly for anisotropic media (crystals) where the electrostriction effect is represented by 4<sup>th</sup> order tensor where the electrostrictive coefficients are labelled as  $Q_{ijkl}$  with  $i,j,k,l=x,y,z$  ; i.e. the cartesian coordinates. The relation between the strain component  $S_{ij}$  and the polarization  $P_k$  is written as follows:

$$S_{ij} = Q_{ijkl}P_kP_l \quad \dots(5.1)$$

Introducing the relation between the strain and the electric field, we obtain the following expression in terms of electric field components  $E_{i=x,y,z}$ :

$$S_{ij} = M_{ijkl}E_kE_l \quad \dots(5.2)$$

As also stated in the non-tensorial formalism, the coefficients  $M_{ijkl}$  depends on the electrostrictive coefficient  $Q_{ijkl}$  and the dielectric constant of the crystalline media. The electrostriction is thus traduced by a second order coupling and can be developed in all crystals irrespective to their symmetry<sup>[184]</sup>. However, it is generally observed that the induced strain from electrostriction effect is less important than the piezoelectric effect. Moreover, it was reported in former contributions that the high dielectric responses in ferroelectric relaxors induce important electrostrictive strains compared to classical ferroelectrics. This behavior was demonstrated in the samples Pb(Mg<sub>1/3</sub>Nb<sub>2/3</sub>)O<sub>3</sub>(PMN), Pb(Zn<sub>1/3</sub>Nb<sub>2/3</sub>)O<sub>3</sub>(PZN), and 0.9Pb(Mg<sub>1/3</sub>Nb<sub>2/3</sub>)O<sub>3</sub>-0.1PbTiO<sub>3</sub>(PMN-PT)<sup>[71]</sup>. In these compounds, the electrostrictive effect holds without poling with the relaxors being more performant than classical ferroelectrics. On the other hand, the piezoelectric and the electrostrictive effects are dependent on the spontaneous polarization and their respective coefficients  $d_{mij}$  and  $Q_{ijkl}$  are related to each other as follow:<sup>[71]</sup>

$$d_{mij} = \frac{\partial S_{ij}}{\partial E_m} = Q_{ijkl}P_k \frac{\partial P_l}{\partial E_m} + Q_{ijkl}P_l \frac{\partial P_k}{\partial E_m} \quad \dots(5.3)$$

Which can be also written in terms of the dielectric coefficients  $\epsilon_{lm}$  and  $\epsilon_{km}$



$$d_{mij} = Q_{ijkl}P_k\varepsilon_{lm} + Q_{ijkl}P_l\varepsilon_{km} \quad \dots(5.4)$$

In the case of perovskites crystals, the electrostrictive tensor is defined by three independent parameters that are  $Q_{1111}$ ,  $Q_{1122}$  and  $Q_{2323}$ . Thus, depending on the direction of electrical field application, the strain can be measured and allows estimating the relevant experimental electrostrictive parameters as developed in the forthcoming sections.

## 5.2 Sample preparation and characterization

The single crystal is prepared by the inversion crystallization method, and the specific process was discussed in Chapter 2. The crystal surface (100) was coated with silver electrode. The AC poling is realized by a ferroelectric analyzer (TF2000), and the current-voltage curve during the poling process is measured at the same time, and the poling electric field is 0.2 V/ $\mu\text{m}$ . The voltage of ac poling as a function of time is shown in Figure 5.1(a). The DC poling is realized by a constant current source, and its voltage as a function of time is shown in Figure 5.1(b), and the poling electric field is 0.2 V/ $\mu\text{m}$ . The dielectric properties are tested by novocontrol broadband dielectric spectrometer. Electrostriction and piezoelectric effects are measured using laser Doppler interferometer.

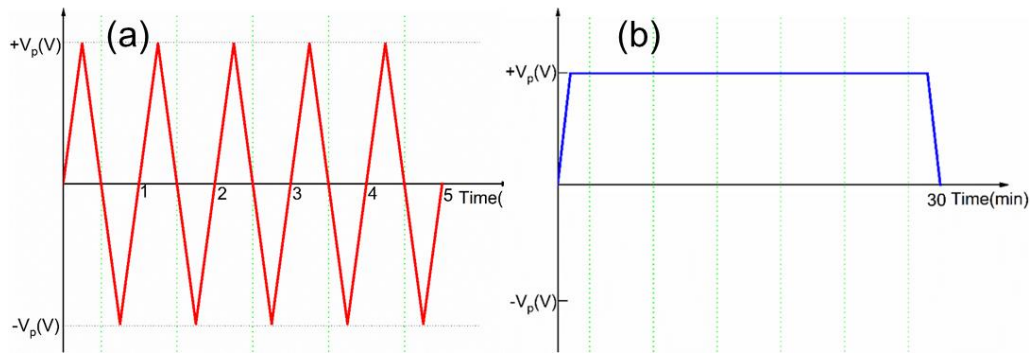


**Figure 5.1** The schematic diagram of the (a) AC poling and (b) DC poling

## 5.3 The piezoelectricity of Quartz

The principle of the measurements is illustrated in Figure 5.2(a) where the crystal faces are metallized for the application of bias voltage. A laser beam is then directed on one metallized face and its reflected part is measured by a photodetector. However,

using this scheme, where only the oscillations of only one face of the sample are detected, the strain level of the sample can be obtained only by assuming the motions of the undetected face of the sample resulting from the strain change<sup>[185]</sup>. To ensure the accuracy of the measurements, the performance of the system can be evaluated by measuring the piezoelectric displacement of a quartz sample. The corresponding piezoelectric coefficient  $d_{11}$  is well defined value irrespective to the measurement frequency. Figure 5.2(b) shows the field induced displacement vs the applied voltage (4 kHz) for an x-cut quartz measured using lock-in detection. The measured  $d_{11}$  value is 2.31 pm/V which is consistent with the result measured by other groups<sup>[184]</sup>. The frequency scan for the quartz sample is shown in Figure 5.2(c). The  $d_{11}$  value is constant in the range of 1 kHz to 5 kHz. The above results indicate that the measurement scheme is reliable and accurate.

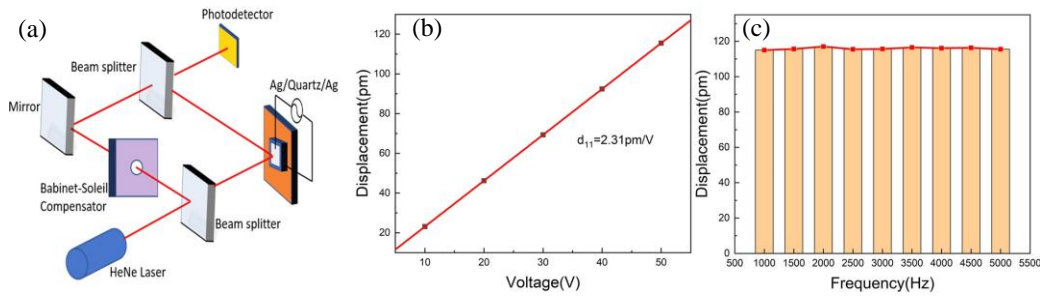


**Figure 5.2** (a) Laser interferometry process and the measured displacement as function of the applied voltage (b) and the excitation frequency (c) in a quartz single crystal.

#### 5.4 Electrostriction and piezoelectricity of MAPbI<sub>3</sub> single crystals

In order to improve the signal-to-noise ratio of the test, the electrostriction and piezoelectric properties are measured at 4 kHz. Figure 5.3(a) shows the displacement time-domain signal at 4 kHz. It can be seen that it is a superposition of two sine waves, indicating that electrostriction and piezoelectric effects exist simultaneously. The time domain signal can be transformed into a frequency domain signal by Fourier transform (FFT), and the result is shown in Figure 5.3(b).

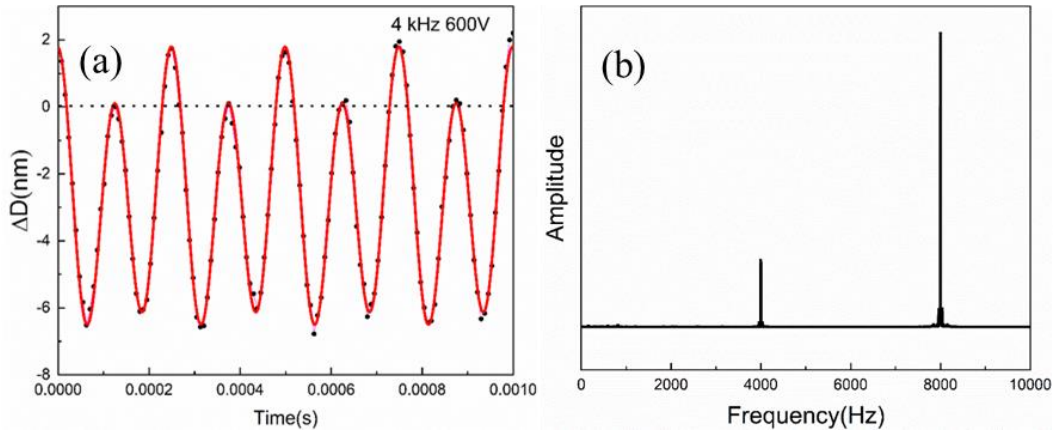


**Figure 5.3** (a) Time-domain and (b) frequency-domain displacement signal under 600 V VPP for the sample

As illustrated in Figure 5.4(a), the modulated signal seems to contain a superposition of two harmonic waves resulting from the piezoelectric (first order) and to electrostriction effect (second order). The lock-in amplifier discriminates between the electrostrictive effect and the piezoelectric effect. The electrostrictive displacement modulated at the second harmonic is shown in Figure 5.4(b) where a small phase difference exists between electrostrictive effect and applied voltage. The phase shift can be attributed to the defect relaxation as considered in the reference<sup>[186]</sup>. The piezoelectric displacement and electrostriction strain are represented in Figure 5.4(c) as function of the applied electric field. The results highlight the simultaneous involvement of both piezoelectricity and electrostriction effects in MAPbI<sub>3</sub> single crystal in agreement with previous results obtained by atomic force microscope (AFM)<sup>[80]</sup>. Figure 5.4(d) shows the displacement of electrostriction of no poling sample as a function of frequency. It can be seen that the electrostriction will increase as the frequency decrease which is in agreement with previous report<sup>[80]</sup> which is claimed to be related to the field-induced defects.

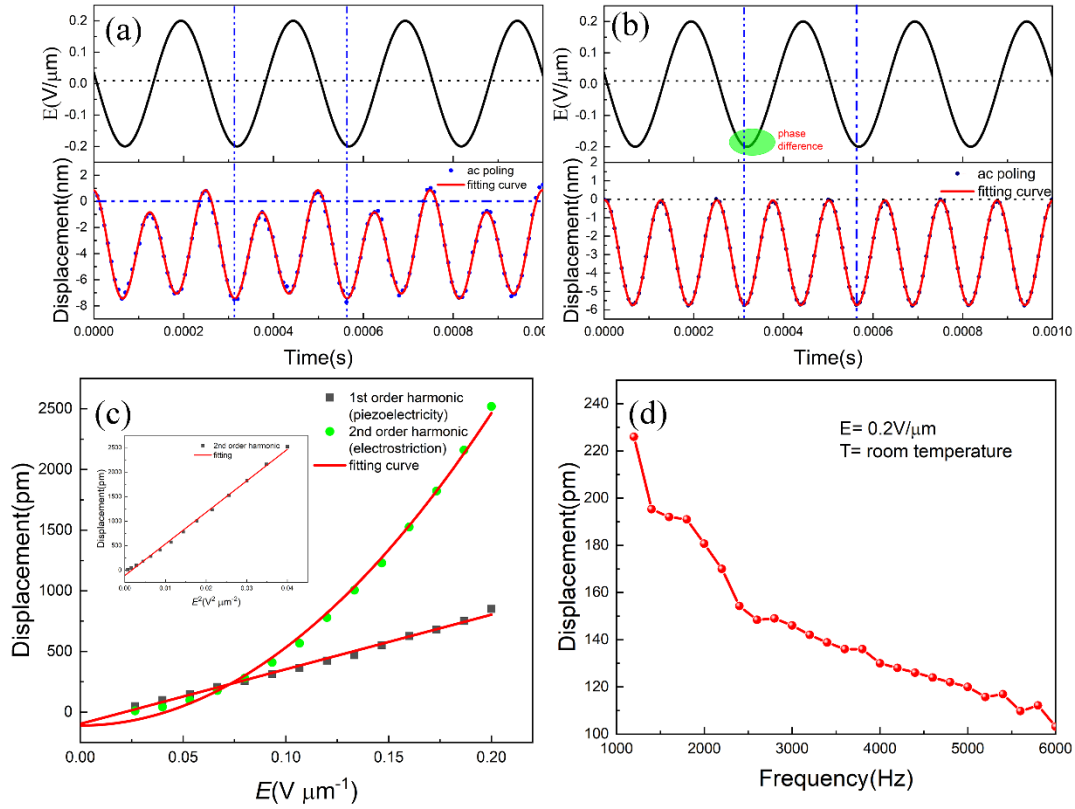


**Figure 5.4.** (a) displacement (both piezoelectricity and electrostriction), (b) displacement (filtering the displacement of piezoelectricity) of MAPbI<sub>3</sub> single crystal with a thickness of 3 mm after ac poling at 1 Hz under ac bias at 4 kHz, (c) displacement as a function of electric field due to the first-order piezoelectricity and second-order electrostriction, the inset diagram is the displacement of electrostriction as a function of the square of electric field. (d) The displacement of electrostriction as a function of frequency

### 5.5 Poling effect on the electrostrictive response in MAPbI<sub>3</sub> single crystals

For different poling conditions, the electrostrictive and piezoelectric effect were measured as function of the applied electrical fields with different frequencies. The results related to the piezoelectric and electrostrictive responses are depicted in Figure 5.5 along with the current-voltage curves and the dielectric parameters. The electrostrictive coefficient was estimated at  $M = -0.49 \text{ nm}^2\text{V}^{-2}$  for MAPbI<sub>3</sub> single crystals, i.e. a typical value for a material with a small dielectric constant<sup>[77]</sup>. With the electrical field applied in the [001] direction and the strain measured in the [001] direction, the effective electrostriction coefficient corresponds to the electrostrictive

tensor component  $M_{33}$  hereafter referred as  $M$  coefficient. However, the Maxwell stress will have a contribution to the strain which can be calculated from:<sup>[76]</sup>

$$M = -\varepsilon' \varepsilon_0 / 2Y \quad \dots(5.5)$$

where  $\varepsilon'$  is the relative dielectric permittivity,  $\varepsilon_0$  is the vacuum dielectric permittivity. Using the Young's modulus of 14.8 GPa and the dielectric constant 158, the estimated electrostriction coefficient is  $-0.047 \text{ nm}^2\text{V}^{-2}$  which is at least three orders magnitude smaller than the measured value from the electrostrictive displacement with ac poling. Thus, the electrostrictive coefficient increases up to  $-14.0 \text{ nm}^2\text{V}^{-2}$  after dc poling and  $-49.3 \text{ nm}^2\text{V}^{-2}$  after ac poling. These results underline the minor contribution from Maxwell stress effect to the electrostriction in MAPbI<sub>3</sub> crystal.

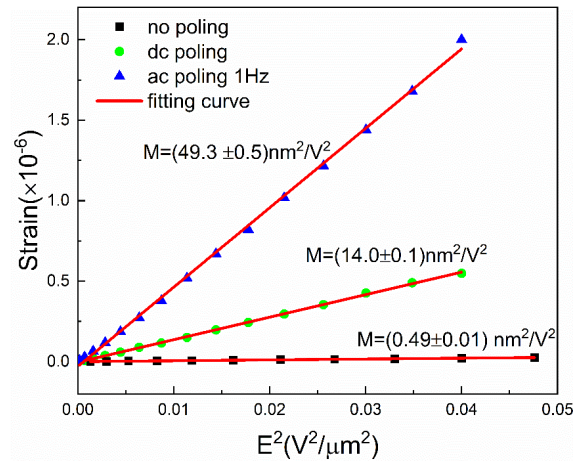


**Figure 5.5** Electrostrictive strain as a function of the square electric field

## 5.6 Poling effect on the piezoelectric response in MAPbI<sub>3</sub> single crystals

In a previous work, the piezoelectric force microscopy (PFM) was used to evaluate the piezoelectric coefficients in MAPbI<sub>3</sub> thin films. The values about 5 pm/V without light and 25 pm/V under white light were attributed to the voltage induced polarization<sup>[82]</sup>. Subsequent study revealed the enhanced piezoelectricity in Fe<sup>2+</sup>-incorporated MAPbI<sub>3</sub> films<sup>[87]</sup>. However, the application of the conductive tip directly on the sample in PFM leads to an effective piezoelectric coefficient that may not coincide with the intrinsic piezoelectric coefficient of the probed sample<sup>[89]</sup>. Previous reports have shown the non-uniform ionic transport features<sup>[31, 34-35]</sup> giving rise to a piezoelectric-like deformation under the applied electric field and tip-induced strain

gradient. This effect was proved by the electrochemical strain microscopy<sup>[90]</sup>. In addition, a converse flexoelectricity may induce large PFM signals in non-piezoelectric materials<sup>[89]</sup>. Based on the above discussion, the PFM method is not a reliable test method for the measurement of piezoelectric coefficients of MAPbI<sub>3</sub>. Thus, a single beam optical interferometry with a high resolution of  $10^{-3}$  nm is a relevant approach for the measurement of the intrinsic piezoelectric response<sup>[79, 92]</sup>. By using this method, the piezoelectric coefficient measured at 4 kHz in non-poled samples is about 0.013 pm/V which is two orders of magnitude smaller than that measurement by Mach–Zehnder interferometer at 100 Hz<sup>[80]</sup>. In fact, several references<sup>[22, 99, 187]</sup> claimed that the tetragonal phase MAPbI<sub>3</sub> at room temperature is centrosymmetric with space group I4/mcm where no second harmonic generation (SHG) signal and nor piezoelectricity are involved. The low piezoelectric effect should be more reliable compared to the large piezoelectric coefficient up to 5 pm/V; i.e. larger than the values in the non-centrosymmetric quartz. The origin of the expected weak piezoelectricity in MAPbI<sub>3</sub> may be induced by the lattice distortion caused by the defects<sup>[188]</sup>. As shown in Figure 5.6, for dc poled sample, the piezoelectric coefficient  $d_{33}$  reaches the value 0.076 pm/V in the [001] direction and different values can be obtained as function of the considered direction in the crystal. In the ac poled sample, the piezoelectric coefficient shows a substantial increase up to 1.33 pm/V at a low voltage ( $\leq 360$  V) and 1.64 pm/V at high voltage ( $> 360$  V). The enhanced piezoelectricity in poled samples can be accounted for by the slight distortion of Pb-I-Pb under the electric field<sup>[94]</sup>. The difference between the high voltage and low voltage may be originated from the slight poling effect at high voltage. This behavior is a consequence of the polarization domain sizes being modulated by the poling which may induce mechanical stress in the host lattice. The poling effect is also crucial on the ionic mobility which enhances the concentrations of both surface and volume defects as well. The influence of dc poling on the piezoelectric properties of MAPbI<sub>3</sub> is also confirmed by the change of the piezoelectric coefficient of the material under a large electric field. As shown in Figure 5.7, under a small electric field ( $< 0.25$  V/ $\mu\text{m}^{-1}$ ), the piezoelectric signal of MAPbI<sub>3</sub> is only 0.0096 pm/V, which is no order of magnitude difference from the 0.013 pm/V measured previously, but in

a large electric field ( $>0.30 \text{ V}/\mu\text{m}^{-1}$ ), the piezoelectric coefficient increases to  $0.077 \text{ pm/V}$ .

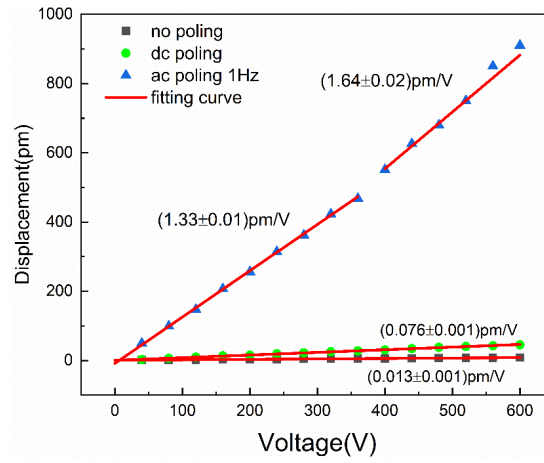


**Figure 5.6** Displacement induced by piezoelectric effect as a function of the applied voltage

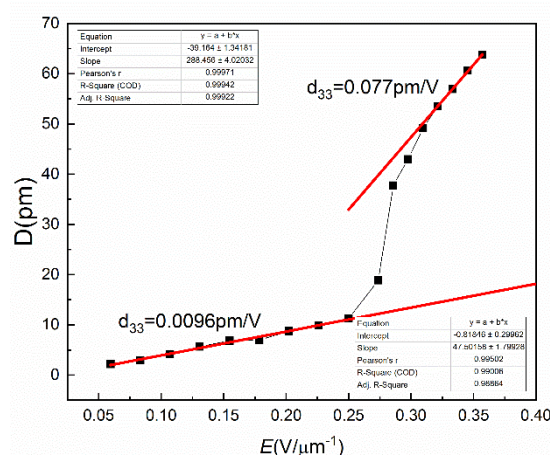


**Figure 5.7** Displacement induced by piezoelectric effect as a function of the applied voltage for the non-poled sample

## 5.7 Defects induced by poling

To figure out the role of the poling on the electrostrictive and piezoelectric effect, the current-voltage curves at different frequencies in ac poled crystal are plotted as illustrated in Figure 5.8(a). It can be seen that at 5 Hz and 10 Hz there is a hysteresis behavior which may be related to the ion migration which can be proved by the dielectric relaxation shown in Figure 5.8(b). At 1 Hz, the ion migration fully realizes and accumulate at the electrode, the hysteresis behavior nearly disappears. However, the current-voltage curve shows unidirectional conductivity as it may occurs in a p-n

junction. This conduction process is induced by a p-i-n structure being formed by the ionic migration under bias voltage<sup>[81]</sup>. In addition to the ionic transport feature, defects are expected to be created after the ac poling as suggested from the shift of the dielectric loss peak seen in Figure 5.8(b). The increase of the dielectric constant at low frequencies was discussed in our previous work<sup>[183]</sup> as emanating from the ionic migration in the sample which causes the formation of defect such as vacancies, anti-site positions or interstitials. As the observed shift of the loss peak to higher frequency is consistent with low activation energies<sup>[189]</sup>, we may expect that the defect density will increase as the activation energy decreases<sup>[190]</sup>. The observed shift of the dielectric loss peak in ac poled sample is more important compared to that observed for dc poling or in non-poled samples. The same features are also observed for the electrostrictive coefficients which increase after ac poling compared to the other poling conditions. These observations support the close correlation between defects and the electrostrictive responses as also stated by previous report<sup>[80]</sup>. In this context, the electrostriction effects originate from the cooperative ionic displacements throughout the crystal lattice<sup>[191]</sup>. The magnitude of the atomic displacements in these materials induced by applied electric fields depend on the polarizability of the host media and on the dielectric constant<sup>[79]</sup>. For most materials, the electrostrictive coefficients can be evaluated from the dielectric constant. Values of  $M$  range from  $10^{-6} \text{ nm}^2 \text{V}^{-2}$  in materials with low dielectric ( $\epsilon < 50$ ) to  $100 \text{ nm}^2 \text{V}^{-2}$  for materials with high dielectric constant ( $\epsilon > 1000$ )<sup>[192]</sup>. For the samples of ac poling and dc poling, the dielectric constant at 4 kHz is almost the same (as shown in Figure 5.8(b)), but the electrostrictive coefficient is very different as it may occurs for nonclassical electrostriction reported in some ion conductors. Those ion-conductors such as Gd-doped CeO<sub>2</sub>, (Y, Nb)-Stabilized  $\delta$ -Bi<sub>2</sub>O<sub>3</sub> with a small dielectric constant show a large electrostriction as also reported in the present work on MAPbI<sub>3</sub> single crystals. The large electrostriction effect in those materials depends on the involved defects favored by the poling process. In Gd-doped CeO<sub>2</sub>, the presence of the vacancies lowers the symmetry of the local charge distribution and therefore, the application of an electric field generates anisotropic ion displacements<sup>[79, 193]</sup>. In MAPbI<sub>3</sub>, due to the low defect formation energy<sup>[194]</sup>, the self-



doping behavior holds and develops under applied electric fields. Previous reports on the involvement of ion migrations in MAPbI<sub>3</sub> corroborate the enhancement of defects formation in the host lattice<sup>[34, 44, 195]</sup>. Although, the defects in MAPbI<sub>3</sub> have little influence on the efficiency of the underlying perovskite solar cells<sup>[196]</sup>, they contribute critically to the sample polarization, piezoelectricity<sup>[56]</sup> and ferromagnetism<sup>[55]</sup>. Based on the above discussion, the relationship between the defects and the large electrostriction seems relevant. As shown in figure 5.9, under dc poling, the electric field induces the ion migration to the electrodes and then contributes to the formation of more lattice defects. Under ac poling, the reverse bias forces the ions to alternate their migration from one electrode to the other via the underlying MAPbI<sub>3</sub> media. The process contributes to create more defects compared to the case of dc poling.

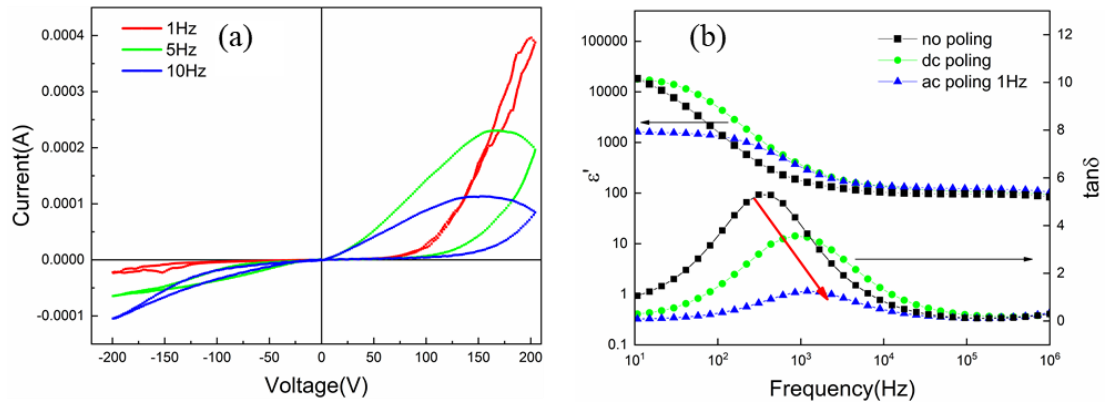


**Figure 5.8** (a) Current-voltage curve with different frequencies for the ac poled samples, (b) dielectric constant and loss as a function of the frequency without and with (ac, dc) poling

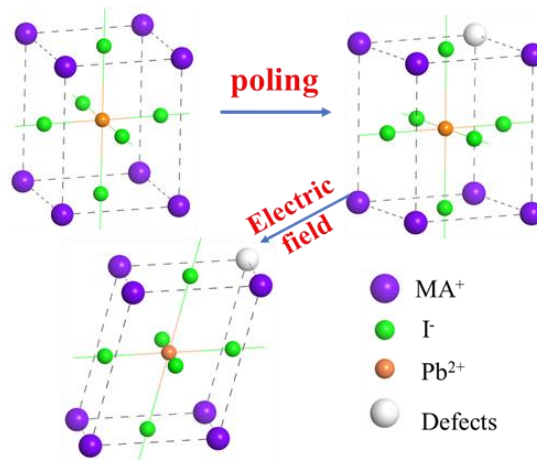


**Figure 5.9** Scheme of the electric field induced reorganization of a distorted lattice

### 5.8 The effect of ac poling frequency on electrostrictive and piezoelectric response of MAPbI<sub>3</sub> single crystals

To further understand the influence of the ac poling, the electrostrictive and piezoelectric effect of the ac poling at different frequencies are investigated and reported in Figure 5.10. It should be noted that both effects are larger for the low frequency 1 Hz compared to the samples poled at 100 Hz. As shown in Figure 5.11, the change in dielectric constant of samples poling at 1 Hz and 100 Hz confirms that the number of defects after 1 Hz ac poling is higher than that after 100 Hz. Thus, the frequency plays a critical central role in the strength of the electrostrictive and piezoelectric response in the hybrid halide perovskites such as MAPbI<sub>3</sub>.

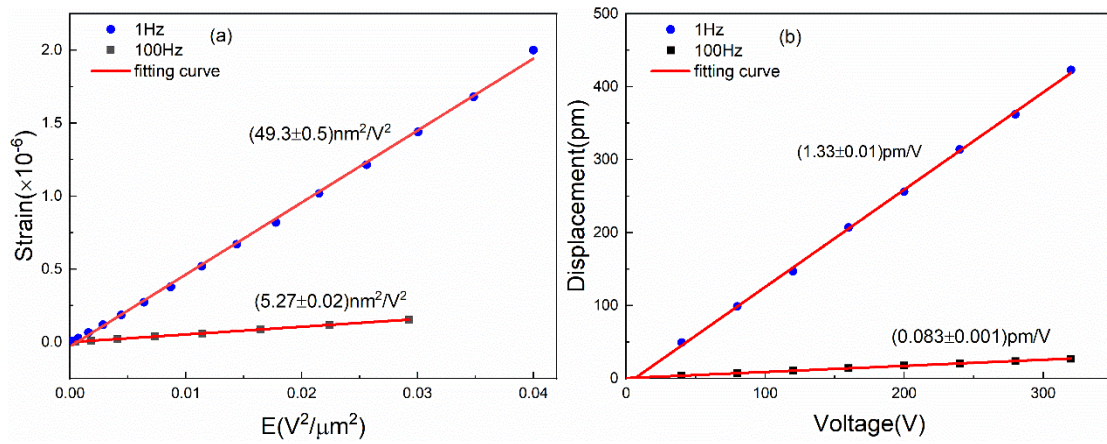


**Figure 5.10** (a) Electrostrictive and (b) piezoelectric effect for the samples ac poled at 1 Hz and 100 Hz

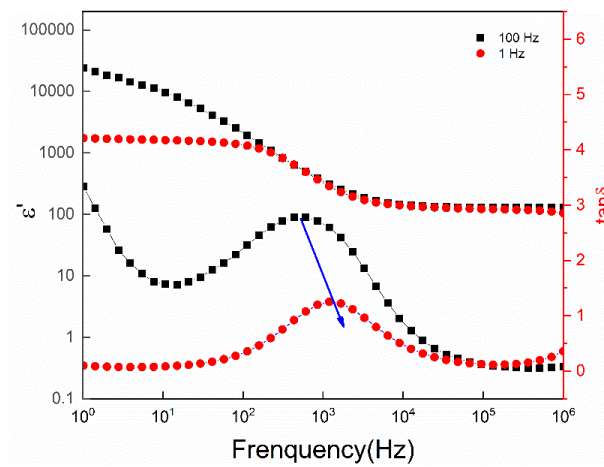


**Figure 5.11** The dielectric constant as a function of frequency for the samples ac poled at 1 Hz and 100 Hz

## 5.9 Conclusion

In conclusion, the investigations of the electrostrictive and piezoelectric effects in MAPbI<sub>3</sub> single crystals were realized under different electrical poling conditions. The electrostrictive and piezoelectric effect were found to be enhanced after ac poling and dc poling. The large electrostrictive response up to  $-49.3 \text{ nm}^2\text{V}^{-2}$  were reported after ac poling at 1 Hz. The more defects concentration after ac and dc poling which can be proved by the current-voltage curve and dielectric spectrum can be used to explain the improvement of the electrostrictive effect. The piezoelectric coefficient of non-poled sample is quite smaller than that using PFM which is more reasonable for the lattice distortion induced by the defects in centrosymmetric materials. Meanwhile, the piezoelectric coefficient reaches to 1.6 pm/V after ac poling which may be accounted by the lattice distortion induced by electric field. The different experimental approaches provide a strategy to fine-tune the electrostrictive and piezoelectric effect of MAPbI<sub>3</sub> single crystal and expand its potential application in actuators, energy harvesting and integrated microelectromechanical systems.



## Chapter 6 Ferroelectric properties of MAPbI<sub>3</sub>

### 6.1 Introduction

A wide literature was devoted to the ferroelectricity of MAPbI<sub>3</sub> since the ferroelectric domains were directly observed by PFM<sup>[197]</sup>. However, the results were controversial. Fan et al.<sup>[100]</sup> calculated the polarization via classic point charge model and the Berry phase method. The results showed that polarization is  $\sim 8 \mu\text{C}/\text{cm}^2$  and originated from dynamic orientational disorder of MA<sup>+</sup>. But Yan et al.<sup>[109]</sup> found that the off-center displacement of Pb<sup>2+</sup> within the PbI<sub>6</sub> octahedron introduces a major intrinsic polarization. The experimental results also conflicted with each other. The noninvolvement of ferroelectricity or its existence as it may be alternatively also involved anti-ferroelectricity, and ferroelasticity were claimed in MAPbI<sub>3</sub> <sup>[28, 101, 198-199]</sup>. The complexity of the ferroelectricity of MAPbI<sub>3</sub> probably results from a weak ferroelectricity that cannot be detected. Moreover, the methods of preparation and the state of samples probably alter the above properties.

To completely understand the ferroelectricity origin in MAPbI<sub>3</sub>, the ferroelectric hysteresis loops of pellets and that of films synthesized in ambient air were investigated. The polarization-electric field (*P-E*) loops and current-electric field (*I-E*) loops of MAPbI<sub>3</sub> show the same features. There is no evidence of ferroelectric switching. The ferroelectricity of the film and single crystals is investigated by piezo-response force microscopy (PFM). The results show that there are domain structures in film and single crystals of MAPbI<sub>3</sub>. Dielectric properties suggest that it is anti-ferroelectricity in low temperature. At room temperature there is no phase transition of the ferroelectricity to the paraelectric phase.

### 6.2 Sample preparation and measurement

The crystal structure of the samples was characterized by powders X-ray diffractometer (XRD, DX-2700BH) with a Cu K $\alpha$  radiation. The *P-E* and *I-E* hysteresis loops of samples were measured by a TF analyzer (Model 2000E, aixACCT Systems, Germany). Ferroelectric domains were observed by atomic force microscope

(AFM5300, Hitachi, Japan). Dielectric properties and the real part of impedance were measured by Novocontrol Alpha-A BroadBand Dielectric Spectrometer, Hundsangen, Germany.

### 6.3 Ferroelectric properties of MAPbI<sub>3</sub>

#### 6.3.1 The effect of CH<sub>3</sub>NH<sub>3</sub>I excess on the phase of MAPbI<sub>3</sub>

Figure 6.1 (a) and (b) show the XRD pattern of the powder and film of MAPbI<sub>3</sub>. The pure MAPbI<sub>3</sub> exhibits diffraction peaks at  $2\theta$  of values of  $14.39^\circ$ ,  $20.26^\circ$ ,  $23.80^\circ$ ,  $24.81^\circ$ ,  $28.75^\circ$ ,  $32.19^\circ$ ,  $40.75^\circ$ , and  $43.36^\circ$  corresponding to the (110), (112), (211), (202), (220), (310), (312), (224), (314) crystal planes of tetragonal perovskite, respectively<sup>[197, 200-201]</sup>. The peak located at  $12.49^\circ$  indicates that PbI<sub>2</sub> impurity phase exists but disappears in the powder and film prepared with MAI: PbI<sub>2</sub> = 1.05:1. It indicates that slight excess MAI ensure the sufficient reaction and eliminate the PbI<sub>2</sub> impurity phase. It is consistent with early report<sup>[202]</sup>. The intensity of (110) peak of film increases as the ratio of MAI: PbI<sub>2</sub> increases from 1:1 to 1.05:1, it means that slight excess MAI can also improve the crystallinity of film.

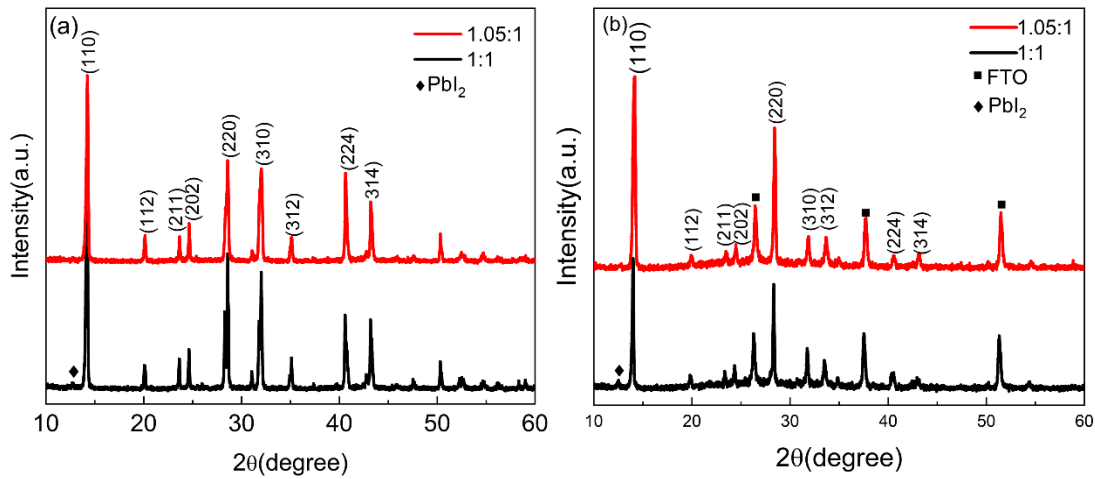


**Figure 6.1** (a) The XRD pattern of the pellets, (b) The XRD pattern of the film

#### 6.3.2 Ferroelectric and dielectric properties of the MAPbI<sub>3</sub> pellets

To investigate the ferroelectric properties, the polarization variation with the applied electric field is examined. Figure 6.2 (a), (b) and (c) show the *P-E* and *I-E* loops of pellets at the frequency of 10 Hz and at three different voltages of 0.075 kV/cm, 0.15

kV/cm, and 1.5 kV/cm. At the voltages of 0.075 kV/cm and 0.15 kV/cm, they show the mixing behaviors of a resistor and a capacitor. The polarization of samples increases with the increase of voltage. The non-saturating behavior suggests that the ferroelectric properties are not dominant to produce the observed hysteresis. The samples behave more like a linear resistor at the voltages of 1.5 kV/cm. In this case, the leakage current is dominated, and the effect of capacitance is covered by large leakage current.

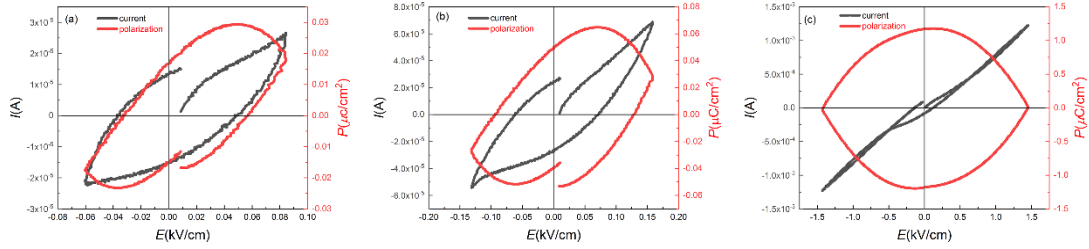


**Figure 6.2** The P-E and I-E loops of pellets for the frequency of 10 Hz and at three different electric field (a) 0.075 kV/cm, (b) 0.15 kV/cm, (c) 1.5 kV/cm

For deep insight in ferroelectricity of MAPbI<sub>3</sub>, the dielectric constant and the real part of impedance as a function of temperature are investigated. The change of the dielectric constant can help to identify the behavior of dipoles. It must be noted that the high dielectric constant at low frequency and high temperature do not correspond to bulk effect. It is attributed to the fact that the free charges accumulate at interface within the bulk of the sample or at the interface between the sample and the electrode<sup>[203]</sup>. The dielectric constant and dielectric loss of MAPbI<sub>3</sub> are measured from 150 K to 350 K at the frequencies of 10 kHz, 100 kHz, and 1000 kHz. Those results are showed in Figure 6.3. It can be seen that the dielectric loss increases with the increase of temperature and decreases with the increase of frequency. The large dielectric loss at high temperature and low frequency results in the increase of dielectric constant. There is a peak of dielectric constant at 162 K at all frequency. It is associated to the tetragonal-orthorhombic phase transition of MAPbI<sub>3</sub><sup>[25]</sup>. The dielectric constant in the orthorhombic phase is temperature-independent. An anti-ferroelectric ordering of dipoles of orthorhombic phase possibly leads to the relatively temperature-independent dielectric properties<sup>[204]</sup>. The dielectric constant decreases with the increase of temperature from 162 K to 350 K and show the evident temperature-dependent feature.

It suggests that the anti-ferroelectric ordering of dipoles is destroyed gradually with the increase of temperature. But there is no peak at 327 K which is the temperature of the tetragonal to the cubic phase transition. It indicates that there is no phase transition from ferroelectric to paraelectric phase.

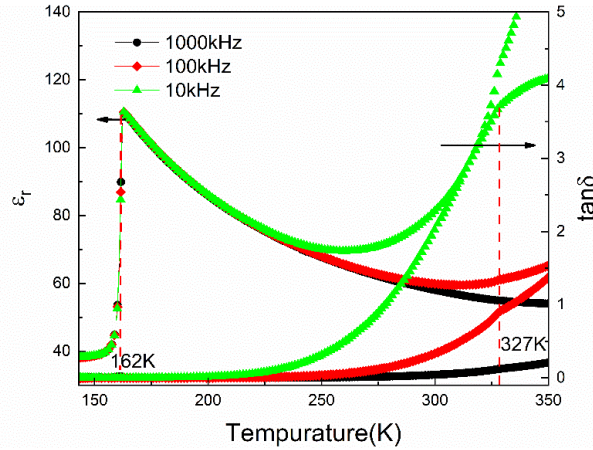


**Figure 6.3** Dielectric constant and dielectric loss as a function of temperature at the frequency of 10 kHz 100 kHz and 1 MHz for MAPbI<sub>3</sub> pellets

### 6.3.3 Analysis of the surface morphology and ferroelectric properties of the MAPbI<sub>3</sub> films

In order to further study the ferroelectric properties of MAPbI<sub>3</sub>, MAPbI<sub>3</sub> thin films were prepared by spin coating. Figure 6.4(a) is the SEM top view of the thin films. It can be seen that the morphology is dendritic, which is caused by the orientation growth of crystals during the evaporation of the solvent. Figure 6.4(b) is the SEM of the cross-section of the films, the thickness of the film is about 2  $\mu\text{m}$ . Use a mask to evaporate a layer of gold electrode on the surface of the films. Figure 6.5 shows the  $P$ - $E$  and  $I$ - $E$  loops of film at the frequency of 10 Hz and the voltage of 1 V. The shape of  $P$ - $E$  loops is an ellipse and the shape of  $I$ - $E$  loops is linear. Those results are attributed to the large leakage current in thin film. Both of pellets and films have no evident domain switching current which can be observed in typical ferroelectricity such as BaTiO<sub>3</sub>. Probably the domain switching current is very small and is covered by the leakage current completely. Those results are consistent with refs<sup>[100]</sup> and <sup>[205]</sup> for samples prepared in the glove box. Most of these investigations concluded on the absence of ferroelectricity in MAPbI<sub>3</sub> systems.



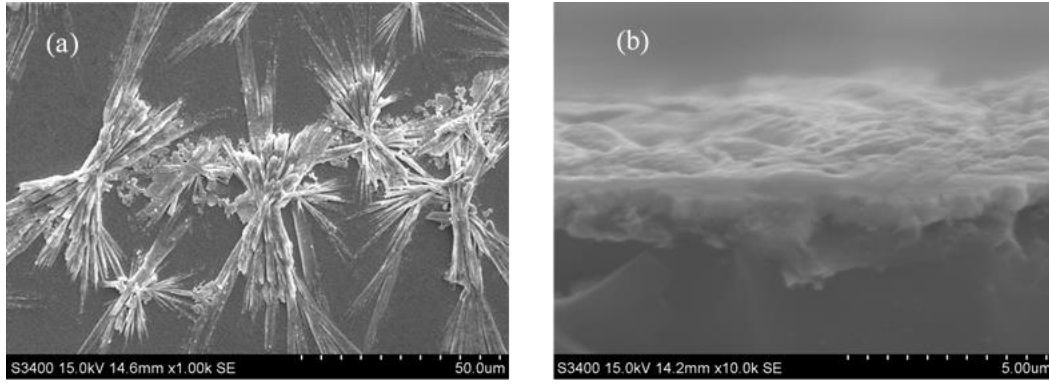


**Figure 6.4** The SEM image of MAPbI<sub>3</sub> (a) top-view (b) cross-sectional SEM images

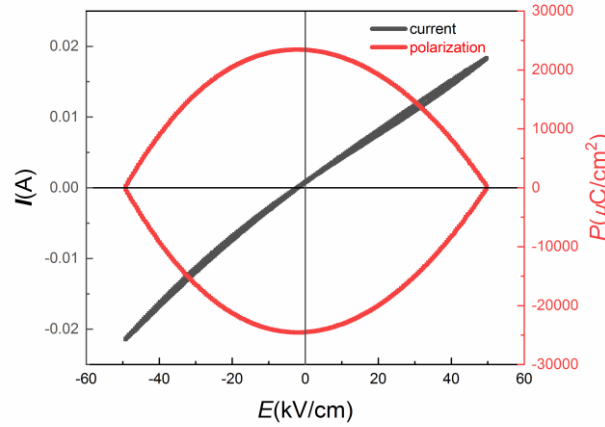


**Figure 6.5** The hysteresis loop of MAPbI<sub>3</sub> films

Piezo-response force microscopy (PFM) is based on the detection of a bias-induced surface deformation. If MAPbI<sub>3</sub> is ferroelectric, the surface deformation resulting from the change of polarization under the bias fields can be observed while the influence of leakage current can be avoided by PFM. Moreover, PFM can measure the deformations in the sub-picometer and map ferroelectric domain patterns with a lateral resolution of a few nanometers. Hence the ferroelectric properties of film of MAPbI<sub>3</sub> are investigated by PFM. Figure 6.6 (a) is a  $3 \times 3 \mu\text{m}^2$  AFM image showing the topography of the MAPbI<sub>3</sub> thin films. The PFM contrast can be influenced by the topographic artifacts and a flat surface of the sample is needed. The topography shows that the film is compact and flat. Figure 6.6 (b) and (c) show the horizontal and vertical PFM imaging. The bright and dark area with the different direction of polarization is

observed. This fact didn't result from the roughness of the surface which may lead to the difference in the amplitude even if it is weak probably due to the low level of ferroelectric response. In addition, the amplitude in the plane is stronger than that out of the plane.

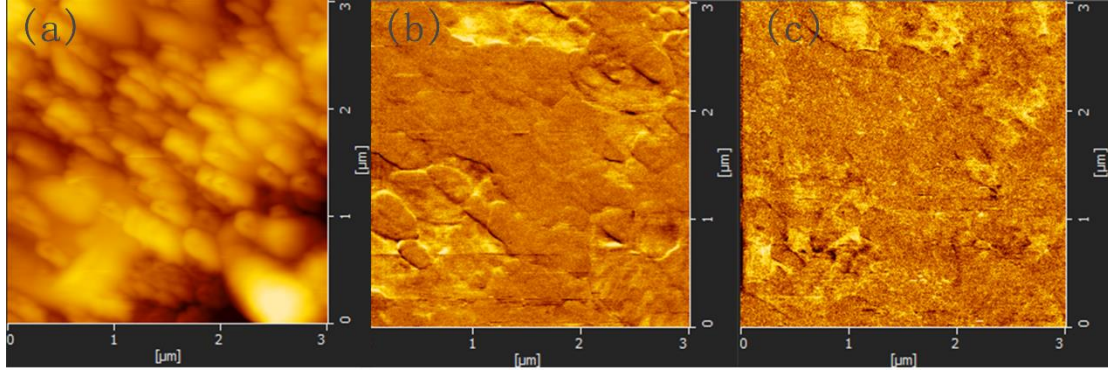


**Figure 6.6** AFM and PFM images of MAPbI<sub>3</sub> thin film ( $3 \times 3 \mu\text{m}^2$ ): (a) AFM topography, (b) PFM amplitude in plane, (c) PFM amplitude out of the plane

### 6.3.4 Ferroelectric properties of MAPbI<sub>3</sub> single crystals

Due to the large number of defects in the bulk crystal and in films, the ferroelectric properties of the material may be affected by such defects [187]. Even though MAPbI<sub>3</sub> exhibits a ferroelectricity, different ferroelectric domain orientations for MAPbI<sub>3</sub> films will cancel each other out. In order to eliminate the influence of these problems, we investigate the hysteresis loop of the MAPbI<sub>3</sub> single crystals at 1 Hz, 5 Hz, 10 Hz, 50 Hz, 100 Hz as reported in Figure 6.7. From these results, the following conclusions can be drawn: (1) The hysteresis loop exhibits frequency-dependent characteristics and unsaturated shapes. These characteristics indicate that the ferroelectricity of MAPbI<sub>3</sub> is not sufficient to produce a conventional hysteresis loop; (2) MAPbI<sub>3</sub> has a large leakage current at low frequencies. The Current-voltage curve has unidirectional conductivity at low frequencies, and unidirectional conductivity is closely related to ion migration; (3) The leakage current is small at high frequencies, which may be due to the weakening of ion migration at high frequencies; (4) The phenomenon in the MAPbI<sub>3</sub> single crystals is the same as in films where no obvious domain switching was shown along with the current generated in the crystal. Because the ion migration in single crystals under an electric field will produce a large leakage current, it is also difficult to analyze the

ferroelectric properties of MAPbI<sub>3</sub> single crystal by hysteresis loop. In order to avoid the influence of leakage current, PFM is used to investigate the ferroelectric properties of single crystals. Figure 6.8(a) reports the AFM topography of MAPbI<sub>3</sub> single crystal. It can be seen that the surface is relatively flat. Figure 6.8(b) is the PFM signal in the plane. There are bright and gray area indicating that MAPbI<sub>3</sub> single crystal shows a ferroelectricity, but it does not have the common stripe domain structure likesome ferroelectric single crystals.

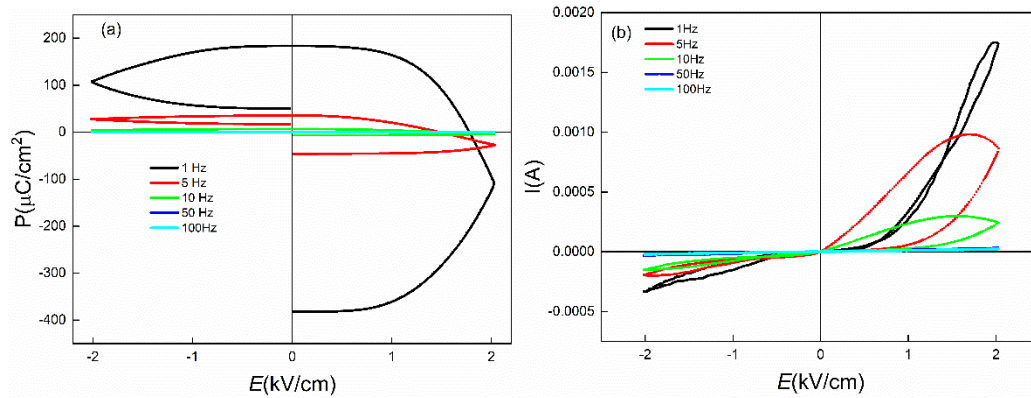


**Figure 6.7** Hysteresis loops of the MAPbI<sub>3</sub> single crystal. (a) P-E loops. (b) I-E loop

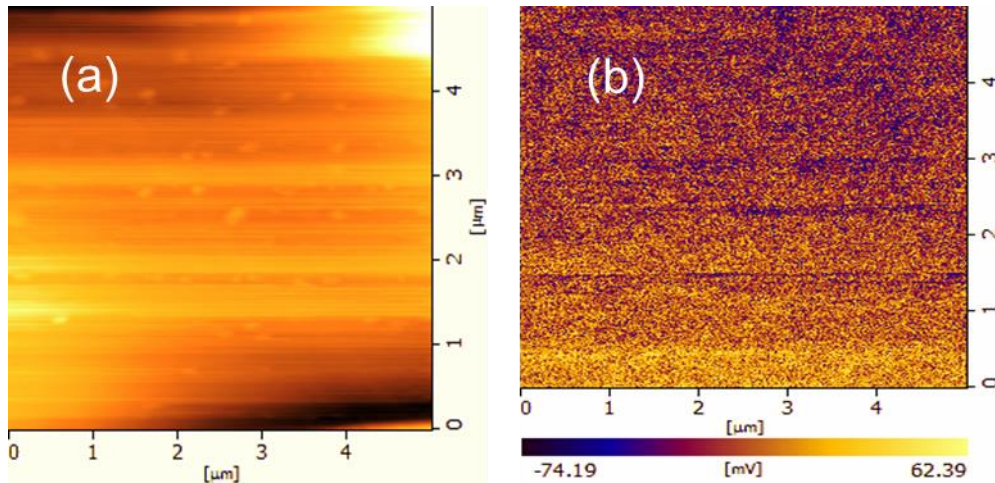


**Figure 6.8** (a) AFM topography, (b) PFM amplitude in plane of MAPbI<sub>3</sub> single crystal

## 6.4 Conclusion

In summary, the ferroelectricity of pellets and film of MAPbI<sub>3</sub> synthesized in ambient air are investigated. The P-E hysteresis loops demonstrate that there is no domain switching current which is a typical characteristic of ferroelectricity. But the

ferroelectric domains are observed in the film synthesized in ambient air. The dielectric constant as a function of temperature demonstrates that there are the tetragonal to orthorhombic and tetragonal to cubic phase transition. There is no ferroelectric-paraelectric phase transition. The hysteresis loop of the single crystal is affected by ion migration, and there is no typical hysteresis loop. The PFM signal from single crystal indicates that the single crystal has weak ferroelectricity.

## Chapter 7 Exploration of MAPbI<sub>3</sub> Photocatalytic Properties

### 7.1 Introduction

Benzaldehyde is the raw material of many fine chemicals and used as an intermediate widely used in dyes, pesticides, medicines, and other industries. As a raw material with large demand, the green and efficient production of benzaldehyde will be of great significance. The benzyl alcohol oxidation method has become a relatively common production method in industry due to its simple process. However, the traditional production method will produce toxic and harmful substances, which does not meet environmental protection requirements and green sustainable development. Therefore, the search for a high-efficiency and green catalysts has become a challenging task and attract the interest of wide scientific community. Among many catalysts, TiO<sub>2</sub> has become a hot spot in industrial applications and basic research due to its wide band gap, high efficiency, high stability, and low cost. However, its absorption of light is limited to the ultraviolet and cannot absorb visible light, which accounts for 45%-50% of solar energy. The narrow band gap semiconductor of MAPbI<sub>3</sub> provides a new strategy for improving the photocatalytic performance of TiO<sub>2</sub>, through an easy transfer of photogenerated charge carriers. However, the instability of MAPbI<sub>3</sub> under moisture also limits its application in heterogeneous photocatalysis. In order to solve this problem, Wu et al.<sup>[21]</sup> synthesized a composite of MAPbI<sub>3</sub> and reduced graphene oxide (rGO), which showed high photocatalytic hydrogen production efficiency in the HI saturated solution of MAPbI<sub>3</sub>. Huang et al.<sup>[133]</sup> explored the photocatalytic oxidation performance of TiO<sub>2</sub>/FAPbBr<sub>3</sub> composite materials in toluene solution for benzyl alcohol. The goal of this work is to explore the possibility of exploiting the photactivity of MAPbI<sub>3</sub> in photocatalytic reactions. The main focus on the material structure associates heterostructures made by MAPbI<sub>3</sub>/TiO<sub>2</sub>. This association is expected to create synergetic charge creation required for the oxidation of benzyl alcohol by oxygen and hydroxyl radicals with relevant efficiency.

## 7.2 Sample preparation and photocatalytic characterization

MAPbI<sub>3</sub> powder is prepared by the anti-solvent method. MAI and PbI<sub>2</sub> are dissolved in dimethylformamide (DMF) in equal moles to prepare a 1 mol/L solution, and then kept the solution in an oil bath at 60 °C for 12 h. Then the solution is dropped to 5 ml toluene solution which is continuously stirred. The resulting mixture is continuously stirred for 12 h, and then the solution and the precipitate are separated using a centrifuge, and the precipitate is washed with toluene several times and then are placed in an oven and dried at 80 °C to get the powder.

x (MAPbI<sub>3</sub>)/TiO<sub>2</sub> powder (x is the mass percentage of MAPbI<sub>3</sub> wt%) is prepared by the same method. The only difference is that a certain amount of MAPbI<sub>3</sub> solution is added dropwise to a toluene solution containing a certain amount of TiO<sub>2</sub>, and finally the mass percentages are 5%, 10%, 15%, 20%, and 25% of MAPbI<sub>3</sub>/TiO<sub>2</sub>. The second step dissolve 1 uL of benzyl alcohol in 10 ml of toluene solution to prepare a 1 mmol/L solution, and then add 10 mg of catalyst to the solution with an ultrasonic dispersion to ensure separated grains and then higher contact surface between the photocatalysts and the liquid. Then, the resulting solution was placed under a 500 W xenon lamp in order to create the photoinduced charges required for the photocatalytic oxidation reactions. After 1 h of illumination, we take 1 ml of the solution with a syringe and filter, and use a gas chromatograph to analyze the content of benzyl alcohol and benzaldehyde.

## 7.3 XRD pattern of MAPbI<sub>3</sub>/TiO<sub>2</sub>

Figure 7.1 shows the XRD of TiO<sub>2</sub>, MAPbI<sub>3</sub> and x MAPbI<sub>3</sub>/TiO<sub>2</sub> (x=5%, 10%, 15%, 20%, 25%) samples. Pure MAPbI<sub>3</sub> and MAPbI<sub>3</sub>/TiO<sub>2</sub> composite materials are prepared by the anti-solvent method.

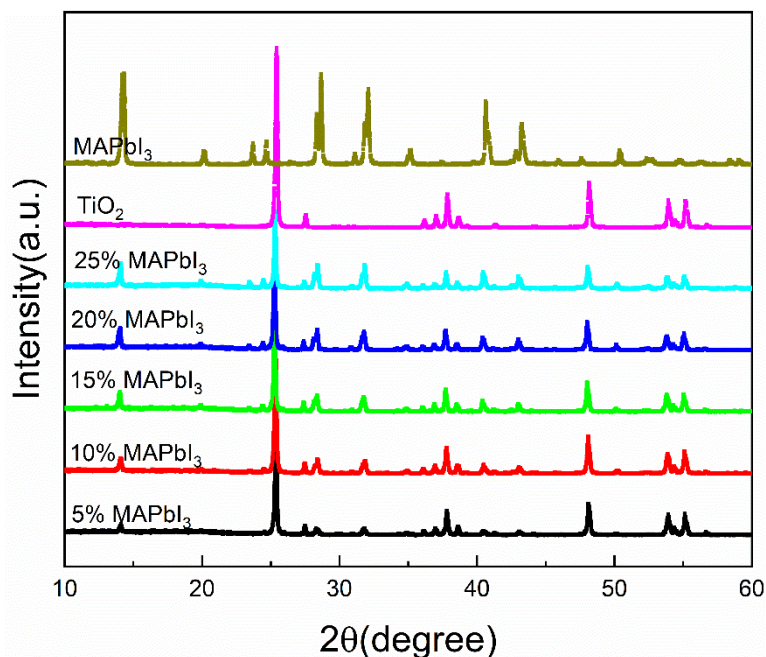
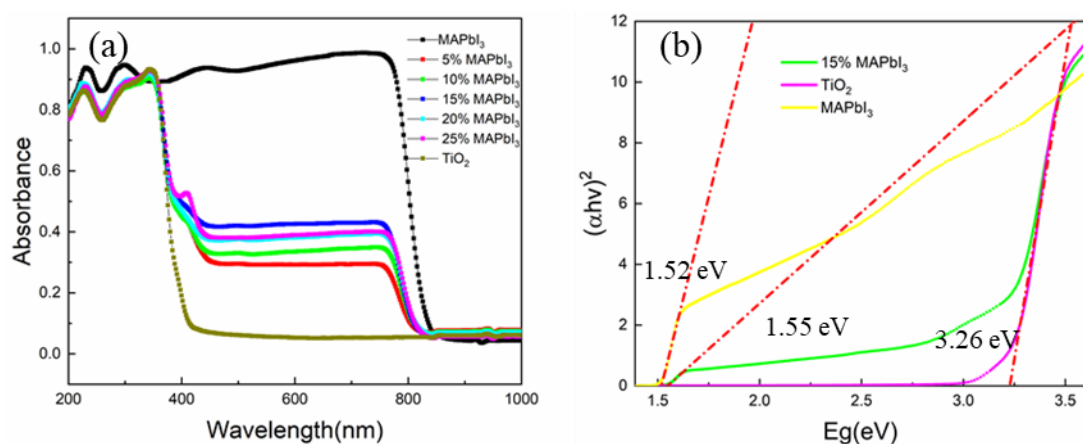


**Figure 7.1** XRD of TiO<sub>2</sub>, MAPbI<sub>3</sub> and MAPbI<sub>3</sub>/TiO<sub>2</sub> between the 2θ range of 10-60°

#### 7.4 Optical properties of MAPbI<sub>3</sub>/TiO<sub>2</sub> composite

Figure 7.2(a) shows the UV-visible absorption spectra of MAPbI<sub>3</sub> and TiO<sub>2</sub> and MAPbI<sub>3</sub>/TiO<sub>2</sub>, and Figure 7.2(b) shows the corresponding band gap. The absorption edge of MAPbI<sub>3</sub> is about 845 nm, and the corresponding band gap is 1.52 eV, covering the entire visible light range. The absorption edge of TiO<sub>2</sub> is around 410 nm, which corresponds to a band gap of 3.26 eV, and can only absorb ultraviolet. The absorption edge of the MAPbI<sub>3</sub>/TiO<sub>2</sub> is about 800 nm. Obviously, the MAPbI<sub>3</sub>/TiO<sub>2</sub> combines the characteristics of the two materials so that it can absorb ultraviolet and visible light bands, thereby providing the possibility to improve the photocatalytic performance of TiO<sub>2</sub>. Among them, the absorption of MAPbI<sub>3</sub>/TiO<sub>2</sub> in the visible light range is enhanced in the range of 5%-15%, which is caused by the increase in the content of MAPbI<sub>3</sub>; but in the range of 15%-25%, the absorption of MAPbI<sub>3</sub>/TiO<sub>2</sub> in visible light range is decreased. Therefore, when the content of x is 15%, it has the best light absorption performance in the visible light region. Therefore, this component is selected in the subsequent photocatalysis experiment process, and its corresponding band gap is 1.55 eV.

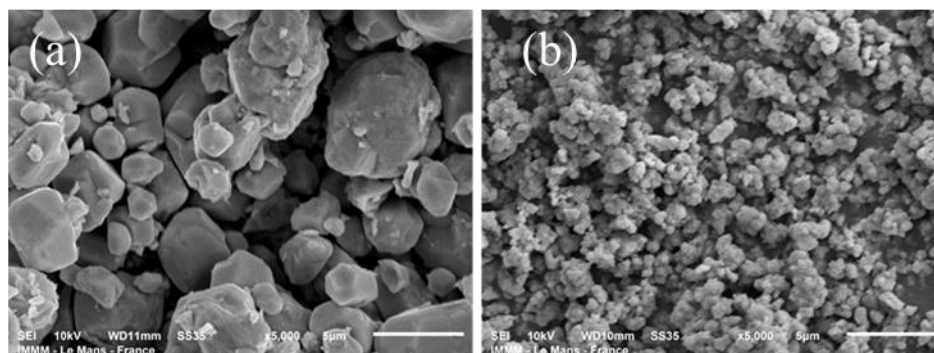




**Figure 7.2** (a) UV-Vis spectra of MAPbI<sub>3</sub>, TiO<sub>2</sub>, and MAPbI<sub>3</sub>/TiO<sub>2</sub> with (b) the corresponding bandgaps

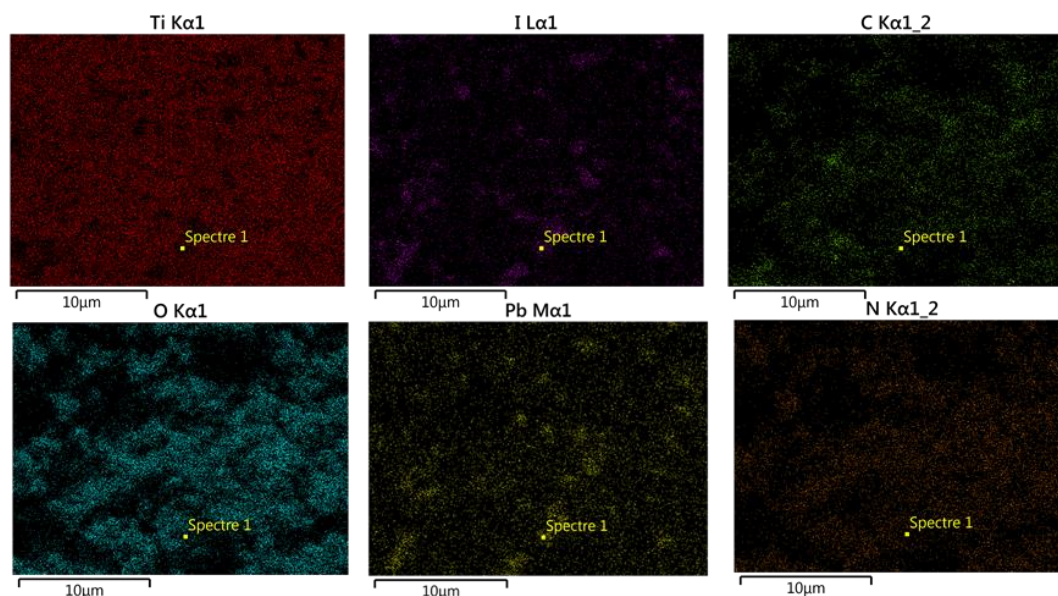
### 7.5 Microstructure and EDS spectrum of MAPbI<sub>3</sub>/TiO<sub>2</sub>

Figure 7.3(a) and (b) show the microscopic morphology of MAPbI<sub>3</sub> and 15%MAPbI<sub>3</sub>/TiO<sub>2</sub>, respectively. The particle size of MAPbI<sub>3</sub> is about 1-5  $\mu\text{m}$ , while the particle size of 15%MAPbI<sub>3</sub>/TiO<sub>2</sub> is small, which means that TiO<sub>2</sub> will inhibit the growth of MAPbI<sub>3</sub> grains during the anti-solvent preparation process. The EDS spectrum of 15% MAPbI<sub>3</sub>/TiO<sub>2</sub> is shown in Figure 7.4. It can be seen that the distribution of each element is uniform indicating that MAPbI<sub>3</sub> and TiO<sub>2</sub> are more uniformly combined.



**Figure 7.3** The SEM of (a) MAPbI<sub>3</sub> and (b) 15%MAPbI<sub>3</sub>/TiO<sub>2</sub>





**Figure 7.4** The EDS of 15% MAPbI<sub>3</sub>/TiO<sub>2</sub>

## 7.6 Photocatalytic oxidation properties of MAPbI<sub>3</sub>/TiO<sub>2</sub>

In order to study the photocatalytic performance of MAPbI<sub>3</sub>/TiO<sub>2</sub>, the blank experiment, the catalytic performance of pure MAPbI<sub>3</sub> powder and TiO<sub>2</sub> were also studied as comparative experiments. After 1 h of illumination, 1 ml of the solution was drawn and analyzed for the content of benzyl alcohol and benzaldehyde by gas chromatography. As shown in Figure 7.5, the peak position of benzaldehyde is 9.605 min, and the peak position of benzaldehyde is 11.05 min.

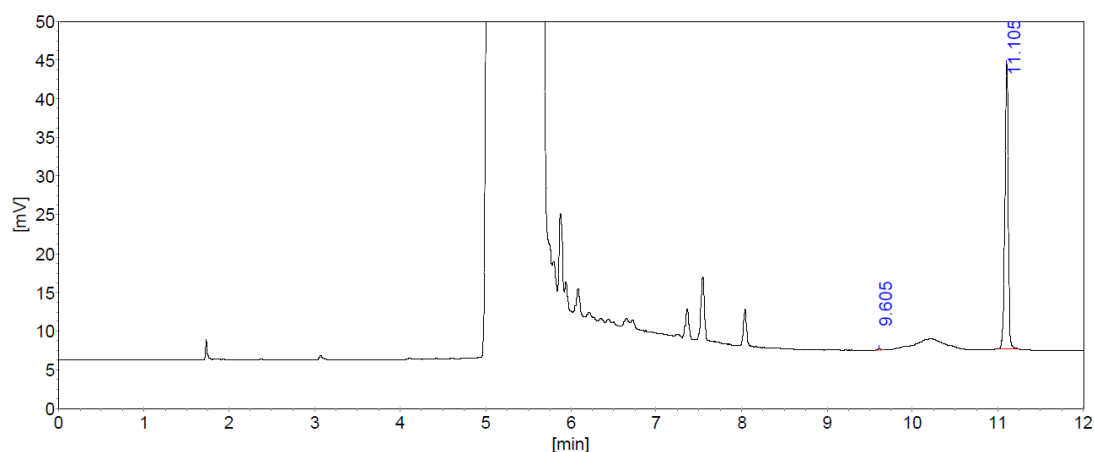


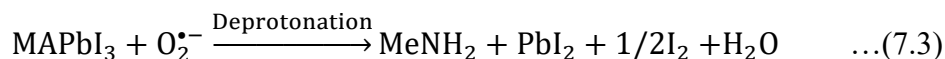
**Figure 7.5** The peak position of benzyl alcohol and benzaldehyde measured by gas chromatography

**Table 7.1** Comparison of benzyl alcohol and benzaldehyde content before and after catalysis

	blank experiment (BI)	blank experiment (AI)	M (BI)	M (AI)	T (BI)	T (AI)	MT (BI)	MT (AI)
Benzaldehyde	1.54%	3.23%	1.82%	6.24%	0.95%	26.90%	0.52%	4.48%
Benzyl alcohol	98.46%	96.77%	98.18%	93.76%	99.06%	76.10%	99.48%	95.52%

Table 7.1 shows the content of benzyl alcohol and benzaldehyde of the samples after being exposed to light for 1 h. Where M represents pure MAPbI<sub>3</sub>, T represents TiO<sub>2</sub>, and MT represents MAPbI<sub>3</sub>/TiO<sub>2</sub>. BI represents “before illumination”. AI represents “after illumination”. The content of benzaldehyde of the blank experiment is 1.54% before illumination which indicates that there is slow oxidation process of benzyl alcohol during storage. After illumination, the content of benzaldehyde reached 3.23%, which means that even in the absence of catalyst, illumination can enhance the oxidation of benzyl alcohol. When 10 mg of MAPbI<sub>3</sub> is added as a catalyst, the content of benzaldehyde before illumination is 1.82%, and the content of benzaldehyde after the illumination is 6.24%, which indicates that MAPbI<sub>3</sub> as a catalyst can enhance the oxidation of benzyl alcohol. However, the catalytic effect is not obvious. Meanwhile, the color of the solution before and after catalysis has changed significantly, as shown in Figure 7.6, from the original pure black to a mixture of gray and red. Since the color of MAPbI<sub>3</sub> is pure black, the change in color indicates that some MAPbI<sub>3</sub> has been oxidized. In previous studies, reported works have shown that oxygen can cause the decomposition of MAPbI<sub>3</sub>, but the decomposition rate of MAPbI<sub>3</sub> is relatively slow<sup>[206]</sup>. Illumination can accelerate the decomposition of MAPbI<sub>3</sub>, which is due to the rapid oxidation of I<sup>-</sup> ions to I<sub>2</sub> under illumination. The red color of the solution after illumination confirms this conclusion. The reaction mechanism of this process is as follows<sup>[207]</sup>:





Where MAPbI<sub>3</sub><sup>\*</sup> is a particle with photogenerated carriers. During this process, MAPbI<sub>3</sub> can absorb photons to generate excitons, and then the electrons are transferred to oxygen molecules to form superoxide anions. Methylamine, lead iodide, iodine and water are produced by the reaction between superoxide anion and MAPbI<sub>3</sub>. The iodine is purple, which is the reason that the color of solution changes. The content of benzaldehyde is 0.95% before illumination and 26.9% after illumination when using TiO<sub>2</sub> as catalyst indicating that the photocatalytic performance of TiO<sub>2</sub> is good. When MAPbI<sub>3</sub>/TiO<sub>2</sub> is used as a catalyst, the content of benzaldehyde before illumination is 0.52% and 4.48% after illumination, which is far lower than TiO<sub>2</sub>. After the combination of the MAPbI<sub>3</sub> and TiO<sub>2</sub>, the photocatalytic performance is decreased. Figure 7.7 shows the color change of the solution before and after the reaction with MAPbI<sub>3</sub>/TiO<sub>2</sub> as a catalyst. The gray solution before illumination is a result of the mixture of black MAPbI<sub>3</sub> and white TiO<sub>2</sub>. However, after illumination the gray disappears, leaving only white TiO<sub>2</sub> and red iodine. This phenomenon indicates that TiO<sub>2</sub> will preferentially catalyze and oxidize MAPbI<sub>3</sub>, that is why the photocatalytic performance of MAPbI<sub>3</sub>/TiO<sub>2</sub> as a catalyst decrease.



**Figure 7.6** Color change of solution before (left) and after (right) catalysis with MAPbI<sub>3</sub> as catalyst



**Figure 7.7** Color change of solution before (left) and after (right) catalysis with MAPbI<sub>3</sub>/TiO<sub>2</sub> as catalyst

## 7.7 Conclusions

In this chapter, MAPbI<sub>3</sub> and MAPbI<sub>3</sub>/TiO<sub>2</sub> powders were prepared by the anti-solvent method. The absorption spectrums show that 15% MAPbI<sub>3</sub>/TiO<sub>2</sub> has the best light absorption performance, and its band gap is between MAPbI<sub>3</sub> and TiO<sub>2</sub>, indicating that MAPbI<sub>3</sub> can expand the light absorption range of TiO<sub>2</sub>. The SEM topography shows that the particle size of MAPbI<sub>3</sub> in MAPbI<sub>3</sub>/TiO<sub>2</sub> is significantly smaller than that of pure MAPbI<sub>3</sub>. The EDS spectrum shows that the distribution of MAPbI<sub>3</sub> and TiO<sub>2</sub> is uniform. The photocatalytic oxidation results indicate that MAPbI<sub>3</sub> has a small photocatalytic oxidation effect on benzyl alcohol, and the catalytic oxidation effect is reduced because I<sup>-</sup> is easily oxidized during the catalytic oxidation process. The catalytic oxidation effect of MAPbI<sub>3</sub>/TiO<sub>2</sub> is much lower than that of TiO<sub>2</sub>, and the assumption of improving photocatalytic properties of TiO<sub>2</sub> by MAPbI<sub>3</sub> has not been realized. It is mainly due to the preferential catalytic oxidation of I<sup>-</sup> by TiO<sub>2</sub>, which leads to the reduction of the catalytic oxidation efficiency of benzyl alcohol. The above experimental results show that MAPbI<sub>3</sub> has a certain catalytic oxidation ability, but the easy decomposition characteristics of MAPbI<sub>3</sub> and the easy catalytic oxidation characteristics of MAPbI<sub>3</sub> limit its application in photocatalytic oxidation. The improvement of the setup to design efficient photocatalyst based on MAPbI<sub>3</sub>/TiO<sub>2</sub> is among the perspectives to develop in near features.

## Chapter 8 General Conclusion and Perspective

### 8.1. Conclusion

- **An overview**

The hybrid perovskite MAPbI<sub>3</sub> possesses excellent optoelectronic properties and their optimization and applications require in depth understanding of the material structure and fundamental physical properties. This thesis investigates the structure and main properties of MAPbI<sub>3</sub> through the following approaches: (1) Study of the dielectric properties of single crystals to point out the relationship between ion migration and giant dielectric effects. Both methylamine MA<sup>+</sup> cations and iodide I<sup>-</sup> anions are mobile species which contribute to the dielectric constant strength. This effect was established and explained by the abnormal change of the dielectric constant of MAPbI<sub>3</sub> under illumination. Through the study of the thermal variation of the dielectric spectrum, the relationship between the orientation of MA<sup>+</sup> ions and the temperature are clarified as also was inferred from the influence of non-polar ions Cs<sup>+</sup> on the ion orientation of MA<sup>+</sup>. The evolution of the dielectric constant was also analyzed close to the critical temperatures of the phase transitions in MAPbI<sub>3</sub>. This study rules out the involvement of ferroelectric-paraelectric phase at the tetragonal-cubic phase change (2) The effects of AC and DC poling on the electrostriction and piezoelectric properties of MAPbI<sub>3</sub> were investigated and point out the role of poling in the strength of the phenomena. The investigations of electrostrictive and piezoelectric effects was conducted with and without poling using DC or AC. The different experiments point out the promising applications of MAPbI<sub>3</sub> in actuators, energy harvesting and integrated MEMS systems. (3) The ferroelectric properties of MAPbI<sub>3</sub> were studied by two different methods: ferroelectric hysteresis loop and PFM. For the structural features, high-resolution XRD was used to characterize the phase transition between the tetragonal and cubic phase in MAPbI<sub>3</sub>; (4) MAPbI<sub>3</sub> and MAPbI<sub>3</sub>/TiO<sub>2</sub> powders were prepared by the anti-solvent method, and the effect of MAPbI<sub>3</sub> on the photocatalytic reactions to oxidize Benzaldehyde and Benzyl alcohol.

### Detailed achieved contributions

The main contributions of the thesis work are as follows:

(1) the dielectric behavior and electrical conductivity of MAPbI<sub>3</sub> single crystal were investigated as function of the frequency in the range [0.01 Hz, 1 MHz] and for the temperatures  $193 \leq T \leq 303$  K. The giant dielectric constant realized at low frequencies and at high temperatures is induced by the ionic migration which may involve both methylamine MA<sup>+</sup> cations and iodide I<sup>-</sup> anions. Additional vacancies are thermally created at high temperatures and the long-range movements of ions will favor their accumulation leading to the space charge density at the interface between the crystal (001) and the Ag electrodes. At intermediate frequencies, hopping of ions is characterized by Debye-like relaxation while at high frequencies the dipole relaxation of MA<sup>+</sup> has small contribution to the dielectric constant. The present results are used to explain the abnormal dielectric properties which were pointed out in MAPbI<sub>3</sub> films with the giant dielectric constant under the light and give exhaustive insights on the process of ionic transport in the hybrid perovskite structure.

The dielectric temperature spectrum of the MAPbI<sub>3</sub> crystal shows that the material has a dielectric peak at 162 K corresponding to the phase transition from the orthorhombic phase to the tetragonal phase. The dielectric constant changes slightly at 327 K indicates that the phase transition from the tetragonal phase to the cubic phase is not the phase transition of ferroelectric phase to paraelectric phase. According to the Kirkwood–Fröhlich–Onsager theory, the fitting results show that MA<sup>+</sup> is in anti-parallel arrangement in the orthorhombic phase, and the dielectric constant does not change with temperature. In the tetragonal phase, the anti-parallel arrangement of MA<sup>+</sup> gradually breaks and shows obvious temperature characteristics. After Cs<sup>+</sup> doping, the optical band gap of MAPbI<sub>3</sub> is changed. According to dielectric temperature spectrum of Cs<sup>+</sup> doped MAPbI<sub>3</sub>, it can be found that Cs<sup>+</sup> doping significantly improves the temperature stability of MAPbI<sub>3</sub> and promotes the anti-parallel arrangement of MA<sup>+</sup> at the same time.

(2) The XRD study of the tetragonal phase to the cubic phase shows that the phase transition from the tetragonal phase to the cubic phase of MAPbI<sub>3</sub> occurs at around

59 °C. There is no obvious difference in the lattice parameters between the heating process and the cooling process indicating that it is the second-order phase transition. (211) As the characteristic peak of the tetragonal phase, its strength gradually decreases with the increase of temperature, and its strength is related to the rotation angle of the octahedra. The change of rotation angle with temperature indicates that the phase transition is not purely a second-order phase transition. By studying the  $\Omega$  scan mode, it is found that the single crystal has a pre-phase transition effect near 59 °C. The Raman results show that there are two vibration peaks of organic groups near the phase transition, indicating that the organic groups may have an influence on the phase transition.

(3) The investigations of the electrostrictive and piezoelectric effects in MAPbI<sub>3</sub> single crystals were realized under different electrical poling conditions. The electrostrictive and piezoelectric effect were found to be enhanced after ac poling and dc poling. The large electrostrictive response up to  $-49.3 \text{ nm}^2\text{V}^{-2}$  were reported after ac poling at 1 Hz. The more defects concentration after ac and dc poling which can be proved by the current-voltage curve and dielectric spectrum can be used to explain the improvement of the electrostrictive effect. The piezoelectric coefficient of non-poled sample is quite smaller than that using PFM which is more reasonable for the lattice distortion induced by the defects in centrosymmetric material. Meanwhile, the piezoelectric coefficient reaches to 1.6 pm/V after ac poling which may be accounted by the lattice distortion induced by electric field. The different experimental approaches provide a strategy to fine-tune the electrostrictive and piezoelectric effect of MAPbI<sub>3</sub> single crystal and expand its potential application in actuators, energy harvesting and integrated microelectromechanical systems.

(4) The ferroelectricity of pellets and film of MAPbI<sub>3</sub> synthesized in ambient air are investigated. The P-E hysteresis loops demonstrate that there is no domain switching current which is a typical characteristic of ferroelectricity. But the ferroelectric domains are observed in the film synthesized in ambient air. The dielectric constant as a function of temperature demonstrates that there are the tetragonal to orthorhombic and tetragonal to cubic phase transition. There is no ferroelectricity to

paraelectric phase transition. The hysteresis loop of the single crystal is affected by ion migration, and there is no typical hysteresis loop. The single crystal PFM signal indicates that the single crystal has weak ferroelectricity.

(5) MAPbI<sub>3</sub> and MAPbI<sub>3</sub>/TiO<sub>2</sub> powders were prepared by the anti-solvent method. The absorption spectrum shows that 15% MAPbI<sub>3</sub>/TiO<sub>2</sub> has the best light absorption performance, and its band gap is between MAPbI<sub>3</sub> and TiO<sub>2</sub>, indicating that MAPbI<sub>3</sub> can expand the light absorption range of TiO<sub>2</sub>. The SEM topography shows that the particle size of MAPbI<sub>3</sub> in MAPbI<sub>3</sub>/TiO<sub>2</sub> is significantly smaller than that of pure MAPbI<sub>3</sub>. The EDS spectrum shows that the distribution of MAPbI<sub>3</sub> and TiO<sub>2</sub> is uniform. The photocatalytic oxidation results indicate that MAPbI<sub>3</sub> has a small photocatalytic oxidation effect on benzyl alcohol, and the catalytic oxidation effect is reduced because I<sup>-</sup> is easily oxidized during the catalytic oxidation process. The catalytic oxidation effect of MAPbI<sub>3</sub>/TiO<sub>2</sub> is much lower than that of TiO<sub>2</sub>, and the assumption of improving photocatalytic properties of TiO<sub>2</sub> by MAPbI<sub>3</sub> has not been realized. It is mainly due to the preferential catalytic oxidation of I<sup>-</sup> by TiO<sub>2</sub>, which leads to the reduction of the catalytic oxidation efficiency of benzyl alcohol. The above experimental results show that MAPbI<sub>3</sub> has a certain catalytic oxidation ability, but the easy decomposition characteristics of MAPbI<sub>3</sub> and the easy catalytic oxidation characteristics of MAPbI<sub>3</sub> limit its application in photocatalytic oxidation.

## 8.2 Perspective

(1) The research on the dielectric properties of MAPbI<sub>3</sub> single crystals is currently only a physical model for analysis, and the relationship between ion migration and dielectric properties of MAPbI<sub>3</sub> is initially established. In the future, the change of the dielectric constant under the bias voltage should be investigated and analyze the influence of the bias voltage on ion migration. In addition, the influence of light on ion migration can be investigated by applying light sources with different intensity.

(2) The study on the electrostrictive and piezoelectric properties of MAPbI<sub>3</sub> is limited to room temperature. In the future, it may be possible to combine experimental devices with temperature control devices to study the effects of temperature on



electrostriction and piezoelectric properties. Since defects have some influence on the electrostriction, it may be possible to study the effect of defects on the crystal structure of MAPbI<sub>3</sub> through X-ray fine absorption structure, and then reveal the relationship between defects and electrostriction.

(3) The prospective photocatalytic tests carried out on MAPbI<sub>3</sub>/TiO<sub>2</sub> deserves to be developed with suitable architecture design. We are confident in the efficient photoactivity as it is exploited in photovoltaics. As phototocatalyst, we must ensure a protective role of TiO<sub>2</sub> which can be made by suitable coating of MAPbI<sub>3</sub>. Thus, the hybrid perovskite contributes to the harvesting of the wide solar spectrum along with its protection from degradation. Thus, this approach may pave the way to innovative photocatalyst.



### Bibliography

1. Kumar, D.; Srivastava, S. K.; Singh, P. K.; Husain, M.; Kumar, V., Fabrication of silicon nanowire arrays based solar cell with improved performance. *Solar Energy Materials and Solar Cells* **2011**, *95* (1), 215-218.
2. Garnett, E.; Yang, P., Light trapping in silicon nanowire solar cells. *Nano Lett* **2010**, *10* (3), 1082-1087.
3. Müller, J.; Rech, B.; Springer, J.; Vanecek, M., TCO and light trapping in silicon thin film solar cells. *Solar Energy* **2004**, *77* (6), 917-930.
4. Nakayama, K.; Tanabe, K.; Atwater, H. A., Plasmonic nanoparticle enhanced light absorption in GaAs solar cells. *Appl Phys Lett* **2008**, *93* (12), 121904.
5. Huynh, W. U.; Dittmer, J. J.; Alivisatos, A. P., Hybrid nanorod-polymer solar cells. *Science* **2002**, *295* (5564), 2425-7.
6. Jackson, P.; Wuerz, R.; Hariskos, D.; Lotter, E.; Witte, W.; Powalla, M., Effects of heavy alkali elements in Cu(In,Ga)Se<sub>2</sub> solar cells with efficiencies up to 22.6%. *physica status solidi (RRL) – Rapid Research Letters* **2016**, *10* (8), 583-586.
7. Grätzel, M., Conversion of sunlight to electric power by nanocrystalline dye-sensitized solar cells. *Journal of Photochemistry and Photobiology A: Chemistry* **2004**, *164* (1-3), 3-14.
8. Nozik, A. J., Quantum dot solar cells. *Physica E-Low-Dimensional Systems & Nanostructures* **2002**, *14*, 115-120.
9. Lin, Y.; Li, Y.; Zhan, X., Small molecule semiconductors for high-efficiency organic photovoltaics. *Chem Soc Rev* **2012**, *41* (11), 4245-72.
10. Weber, D., CH<sub>3</sub>NH<sub>3</sub>PbX<sub>3</sub>, ein Pb(II)-System mit kubischer Perowskitstruktur. *Zeitschrift für Naturforsch* **1978**, *33 b*, 1443–1445.
11. Weber, D., CH<sub>3</sub>NH<sub>3</sub>SnBr<sub>x</sub>I<sub>3-x</sub> (x = 0-3), ein Sn(II)-System mit kubischer Perowskitstruktur. *Zeitschrift für Naturforsch* **1978**, *33 b*, 862–865.
12. Kojima, A.; Teshima, K.; Shirai, Y.; Miyasaka, T., Organometal Halide Perovskites as Visible-Light Sensitizers for Photovoltaic Cells. *J Am Chem Soc* **2009**, *131* (17), 6050.
13. Zhao, J.; Li, Z.; Wang, M.; Wang, Q.; Jin, Z., Exploring the film growth in perovskite solar cells. *Journal of Materials Chemistry A* **2021**, *9* (10), 6029-6049.

14. Best Research-Cell Efficiency. <https://www.nrel.gov/pv/cell-efficiency.html>.
15. Nie, J.; Zhang, Y.; Li, L.; Wang, J., Piezo-phototronic effect enhanced photodetectors based on MAPbI<sub>3</sub> perovskite. *J Mater Chem C* **2020**, 8 (8), 2709-2718.
16. Zhu, H. L.; Liang, Z. F.; Huo, Z. B.; Ng, W. K.; Mao, J.; Wong, K. S.; Yin, W. J.; Choy, W. C. H., Low-Bandgap Methylammonium-Rubidium Cation Sn-Rich Perovskites for Efficient Ultraviolet-Visible-Near Infrared Photodetectors. *Adv Funct Mater* **2018**, 28 (16), 1706068.
17. Wang, S.; Liu, Y. L.; Li, G.; Zhang, J.; Zhang, N.; Xiao, S. M.; Song, Q. H., Lead Halide Perovskite Based Microdisk Lasers for On-Chip Integrated Photonic Circuits. *Advanced Optical Materials* **2018**, 6 (6), 1701266.
18. Veldhuis, S. A.; Boix, P. P.; Yantara, N.; Li, M. J.; Sum, T. C.; Mathews, N.; Mhaisalkar, S. G., Perovskite Materials for Light-Emitting Diodes and Lasers. *Adv Mater* **2016**, 28 (32), 6804-6834.
19. Stranks, S. D.; Snaith, H. J., Metal-halide perovskites for photovoltaic and light-emitting devices. *Nature Nanotechnology* **2015**, 10 (5), 391-402.
20. Peng, M.; Wen, W.; Chen, S.; Chen, B. X.; Yan, K.; Hu, H. W.; Dong, B.; Gao, X.; Yu, X.; Jiang, X. M.; Zou, D. C., Organolead trihalide perovskite materials for efficient light emitting diodes. *Science China-Chemistry* **2016**, 59 (6), 653-658.
21. Wu, Y. Q.; Wang, P.; Zhu, X. L.; Zhang, Q. Q.; Wang, Z. Y.; Liu, Y. Y.; Zou, G. Z.; Dai, Y.; Whangbo, M. H.; Huang, B. B., Composite of CH<sub>3</sub>NH<sub>3</sub>PbI<sub>3</sub> with Reduced Graphene Oxide as a Highly Efficient and Stable Visible-Light Photocatalyst for Hydrogen Evolution in Aqueous HI Solution. *Adv Mater* **2018**, 30 (7), 1704342.
22. Baikie, T.; Fang, Y.; Kadro, J. M.; Schreyer, M.; Wei, F.; Mhaisalkar, S. G.; Graetzel, M.; White, T. J., Synthesis and crystal chemistry of the hybrid perovskite (CH<sub>3</sub>NH<sub>3</sub>)PbI<sub>3</sub> for solid-state sensitised solar cell applications. *Journal of Materials Chemistry A* **2013**, 1 (18), 5628–5641.
23. Oku, T., Crystal Structures of CH<sub>3</sub>NH<sub>3</sub>PbI<sub>3</sub> and Related Perovskite Compounds Used for Solar Cells. **2015**.
24. Whitfield, P. S.; Herron, N.; Guise, W. E.; Page, K.; Cheng, Y. Q.; Milas, I.; Crawford, M. K., Structures, Phase Transitions and Tricritical Behavior of the Hybrid Perovskite Methyl Ammonium Lead Iodide. *Sci Rep* **2016**, 6, 35685.
25. Weller, M. T.; Weber, O. J.; Henry, P. F.; Di Pumpo, A. M.; Hansen, T. C., Complete structure and cation orientation in the perovskite photovoltaic methylammonium lead iodide between 100

- and 352 K. *Chem Commun (Camb)* **2015**, 51 (20), 4180-4183.
26. Lee, M. M.; Teuscher, J.; Miyasaka, T.; Murakami, T. N.; Snaith, H. J., Efficient Hybrid Solar Cells Based on Meso-Superstructured Organometal Halide Perovskites. *Science* **2012**, 338 (6107), 643-647.
27. Motta, C.; El-Mellouhi, F.; Kais, S.; Tabet, N.; Alharbi, F.; Sanvito, S., Revealing the role of organic cations in hybrid halide perovskite  $\text{CH}_3\text{NH}_3\text{PbI}_3$ . *Nat Commun* **2015**, 6, 7026.
28. Rakita, Y.; Bar-Elli, O.; Meirzadeh, E.; Kaslasi, H.; Peleg, Y.; Hodes, G.; Lubomirsky, I.; Oron, D.; Ehre, D.; Cahen, D., Tetragonal  $\text{CH}_3\text{NH}_3\text{PbI}_3$  is ferroelectric. *Proceedings of the National Academy of Sciences of the United States of America* **2017**, 114 (28), E5504-E5512.
29. D'Innocenzo, V.; Grancini, G.; Alcocer, M. J.; Kandada, A. R.; Stranks, S. D.; Lee, M. M.; Lanzani, G.; Snaith, H. J.; Petrozza, A., Excitons versus free charges in organo-lead tri-halide perovskites. *Nat Commun* **2014**, 5, 3586.
30. Zhumekenov, A. A.; Haque, M. A.; Yin, J.; El-Zohry, A. M.; Lee, K. J.; Dursun, I.; Mohammed, O. F.; Baran, D.; Bakr, O. M., Reduced ion migration and enhanced photoresponse in cuboid crystals of methylammonium lead iodide perovskite. *J Phys D Appl Phys* **2019**, 52 (5), 054001.
31. Calado, P.; Telford, A. M.; Bryant, D.; Li, X. E.; Nelson, J.; O'Regan, B. C.; Barnes, P. R. F., Evidence for ion migration in hybrid perovskite solar cells with minimal hysteresis. *Nat Commun* **2016**, 7, 13831.
32. Liu, Y.; Collins, L.; Proksch, R.; Kim, S.; Watson, B. R.; Doughty, B.; Calhoun, T. R.; Ahmadi, M.; Ievlev, A. V.; Jesse, S.; Retterer, S. T.; Belianinov, A.; Xiao, K.; Huang, J.; Sumpter, B. G.; Kalinin, S. V.; Hu, B.; Ovchinnikova, O. S., Chemical nature of ferroelastic twin domains in  $\text{CH}_3\text{NH}_3\text{PbI}_3$  perovskite. *Nat Mater* **2018**, 17 (11), 1013-1019.
33. Almora, O.; Aranda, C.; Garcia-Belmonte, G., Do Capacitance Measurements Reveal Light-Induced Bulk Dielectric Changes in Photovoltaic Perovskites? *J Phys Chem C* **2018**, 122 (25), 13450-13454.
34. Xing, J.; Wang, Q.; Dong, Q. F.; Yuan, Y. B.; Fanga, Y. J.; Huang, J. S., Ultrafast ion migration in hybrid perovskite polycrystalline thin films under light and suppression in single crystals. *Physical Chemistry Chemical Physics* **2016**, 18 (44), 30484-30490.
35. Eames, C.; Frost, J. M.; Barnes, P. R. F.; O'Regan, B. C.; Walsh, A.; Islam, M. S., Ionic transport in hybrid lead iodide perovskite solar cells. *Nat Commun* **2015**, 6, 7497.

36. Yuan, Y.; Chae, J.; Shao, Y.; Wang, Q.; Xiao, Z.; Centrone, A.; Huang, J., Photovoltaic Switching Mechanism in Lateral Structure Hybrid Perovskite Solar Cells. *Advanced Energy Materials* **2015**, *5* (15), 1500615.
37. Futscher, M. H.; Lee, J. M.; McGovern, L.; Muscarella, L. A.; Wang, T.; Haider, M. I.; Fakharuddin, A.; Schmidt-Mende, L.; Ehrler, B., Quantification of ion migration in  $\text{CH}_3\text{NH}_3\text{PbI}_3$  perovskite solar cells by transient capacitance measurements. *Materials Horizons* **2019**, *6* (7), 1497-1503.
38. Yin, W.-J.; Shi, T.; Yan, Y., Unusual defect physics in  $\text{CH}_3\text{NH}_3\text{PbI}_3$  perovskite solar cell absorber. *Appl Phys Lett* **2014**, *104* (6), 063903.
39. Zhu, H. W.; Zhang, F.; Xiao, Y.; Wang, S. R.; Li, X. G., Suppressing defects through thiadiazole derivatives that modulate  $\text{CH}_3\text{NH}_3\text{PbI}_3$  crystal growth for highly stable perovskite solar cells under dark conditions. *Journal of Materials Chemistry A* **2018**, *6* (12), 4971-4980.
40. Liu, C.; Huang, Z. Q.; Hu, X. T.; Meng, X. C.; Huang, L. Q.; Xiong, J.; Tan, L. C.; Chen, Y. W., Grain Boundary Modification via F4TCNQ To Reduce Defects of Perovskite Solar Cells with Excellent Device Performance. *Acs Appl Mater Inter* **2018**, *10* (2), 1909-1916.
41. Lang, F.; Shargaieva, O.; Brus, V. V.; Rappich, J.; Nickel, N. H., Creation and annealing of metastable defect states in  $\text{CH}_3\text{NH}_3\text{PbI}_3$  at low temperatures. *Appl Phys Lett* **2018**, *112* (8).
42. Cai, F. L.; Cai, J. L.; Yang, L. Y.; Li, W.; Gurney, R. S.; Yi, H. N.; Iraqi, A.; Liu, D.; Wang, T., Molecular engineering of conjugated polymers for efficient hole transport and defect passivation in perovskite solar cells. *Nano Energy* **2018**, *45*, 28-36.
43. Snaith, H. J.; Abate, A.; Ball, J. M.; Eperon, G. E.; Leijtens, T.; Noel, N. K.; Stranks, S. D.; Wang, J. T.; Wojciechowski, K.; Zhang, W., Anomalous Hysteresis in Perovskite Solar Cells. *J Phys Chem Lett* **2014**, *5* (9), 1511-5.
44. Yuan, Y. B.; Huang, J. S., Ion Migration in Organometal Trihalide Perovskite and Its Impact on Photovoltaic Efficiency and Stability. *Accounts of Chemical Research* **2016**, *49* (2), 286-293.
45. Tress, W.; Marinova, N.; Moehl, T.; Zakeeruddin, S. M.; Nazeeruddin, M. K.; Grätzel, M., Understanding the rate-dependent J-V hysteresis, slow time component, and aging in  $\text{CH}_3\text{NH}_3\text{PbI}_3$  perovskite solar cells: the role of a compensated electric field. *Energy Environ. Sci.* **2015**, *8* (3), 995-1004.
46. Kim, H. S.; Park, N. G., Parameters Affecting I-V Hysteresis of  $\text{CH}_3\text{NH}_3\text{PbI}_3$  Perovskite Solar

- Cells: Effects of Perovskite Crystal Size and Mesoporous TiO<sub>2</sub> Layer. *J Phys Chem Lett* **2014**, *5* (17), 2927-34.
47. Wei, J.; Zhao, Y.; Li, H.; Li, G.; Pan, J.; Xu, D.; Zhao, Q.; Yu, D., Hysteresis Analysis Based on the Ferroelectric Effect in Hybrid Perovskite Solar Cells. *J Phys Chem Lett* **2014**, *5* (21), 3937-45.
48. Guo, H. Y.; Liu, P. X.; Zheng, S. C.; Zeng, S. X.; Liu, N.; Hong, S. B., Re-entrant relaxor ferroelectricity of methylammonium lead iodide. *Curr Appl Phys* **2016**, *16* (12), 1603-1606.
49. Meloni, S.; Moehl, T.; Tress, W.; Franckevicius, M.; Saliba, M.; Lee, Y. H.; Gao, P.; Nazeeruddin, M. K.; Zakeeruddin, S. M.; Rothlisberger, U.; Graetzel, M., Ionic polarization-induced current-voltage hysteresis in CH<sub>3</sub>NH<sub>3</sub>PbX<sub>3</sub> perovskite solar cells. *Nat Commun* **2016**, *7*, 10334.
50. Li, C.; Tscheuschner, S.; Paulus, F.; Hopkinson, P. E.; Kiessling, J.; Kohler, A.; Vaynzof, Y.; Huettnner, S., Iodine Migration and its Effect on Hysteresis in Perovskite Solar Cells. *Adv Mater* **2016**, *28* (12), 2446-54.
51. Hoke, E. T.; Slotcavage, D. J.; Dohner, E. R.; Bowring, A. R.; Karunadasa, H. I.; McGehee, M. D., Reversible photo-induced trap formation in mixed-halide hybrid perovskites for photovoltaics. *Chem Sci* **2015**, *6* (1), 613-617.
52. Xiao, Z. G.; Yuan, Y. B.; Shao, Y. C.; Wang, Q.; Dong, Q. F.; Bi, C.; Sharma, P.; Gruverman, A.; Huang, J. S., Giant switchable photovoltaic effect in organometal trihalide perovskite devices. *Nature Materials* **2015**, *14* (2), 193-198.
53. Deng, X. F.; Wen, X. M.; Zheng, J. H.; Young, T.; Lau, C. F. J.; Kim, J.; Green, M.; Huang, S. J.; Ho-Baillie, A., Dynamic study of the light soaking effect on perovskite solar cells by in-situ photoluminescence microscopy. *Nano Energy* **2018**, *46*, 356-364.
54. Anusca, I.; Balčiūnas, S.; Gemeiner, P.; Svirskas, Š.; Sanlialp, M.; Lackner, G.; Fettkenhauer, C.; Belovickis, J.; Samulionis, V.; Ivanov, M.; Dkhil, B.; Banys, J.; Shvartsman, V. V.; Lupascu, D. C., Dielectric Response: Answer to Many Questions in the Methylammonium Lead Halide Solar Cell Absorbers. *Advanced Energy Materials* **2017**, *7* (19), 1700600.
55. Sil, S.; Luitel, H.; Dhar, J.; Chakrabarti, M.; Ray, P. P.; Bandyopadhyay, B.; Sanyal, D., Defect induced room temperature ferromagnetism in methylammonium lead iodide perovskite. *Physics Letters A* **2020**, *384* (14), 126278.

56. Dhar, J.; Sil, S.; Hoque, N. A.; Dey, A.; Das, S.; Ray, P. P.; Sanyal, D., Lattice-Defect-Induced Piezo Response in Methylammonium-Lead-Iodide Perovskite Based Nanogenerator. *ChemistrySelect* **2018**, 3 (19), 5304-5312.
57. Wilson, J. N.; Frost, J. M.; Wallace, S. K.; Walsh, A., Dielectric and ferroic properties of metal halide perovskites. *Appl Mater* **2019**, 7 (1), 010901.
58. Chen, Y. F.; Tsai, Y. T.; Bassani, D. M.; Hirsch, L., Experimental evidence of the anti-parallel arrangement of methylammonium ions in perovskites. *Appl Phys Lett* **2016**, 109 (21), 213504.
59. Govinda, S.; Kore, B. P.; Bokdam, M.; Mahale, P.; Kumar, A.; Pal, S.; Bhattacharyya, B.; Lahnsteiner, J.; Kresse, G.; Franchini, C.; Pandey, A.; Sarma, D. D., Behavior of Methylammonium Dipoles in MAPbX<sub>3</sub> (X = Br and I). *Journal of Physical Chemistry Letters* **2017**, 8 (17), 4113-4121.
60. Goehry, C.; Nemnes, G. A.; Manolescu, A., Collective Behavior of Molecular Dipoles in CH<sub>3</sub>NH<sub>3</sub>PbI<sub>3</sub>. *J Phys Chem C* **2015**, 119 (34), 19674-19680.
61. Juarez-Perez, E. J.; Sanchez, R. S.; Badia, L.; Garcia-Belmonte, G.; Kang, Y. S.; Mora-Sero, I.; Bisquert, J., Photoinduced Giant Dielectric Constant in Lead Halide Perovskite Solar Cells. *J Phys Chem Lett* **2014**, 5 (13), 2390-2394.
62. Almond, D. P.; Bowen, C. R., An Explanation of the Photoinduced Giant Dielectric Constant of Lead Halide Perovskite Solar Cells. *J Phys Chem Lett* **2015**, 6 (9), 1736-1740.
63. Frost, J. M.; Walsh, A., What Is Moving in Hybrid Halide Perovskite Solar Cells? *Accounts of Chemical Research* **2016**, 49 (3), 528-535.
64. Hoque, M. N. F.; Yang, M. J.; Li, Z.; Islam, N.; Pan, X.; Zhu, K.; Fan, Z. Y., Polarization and Dielectric Study of Methylammonium Lead Iodide Thin Film to Reveal its Nonferroelectric Nature under Solar Cell Operating Conditions. *Acs Energy Letters* **2016**, 1 (1), 142-149.
65. Shaikh, P. A.; Shi, D.; Retamal, J. R. D.; Sheikh, A. D.; Haque, M. A.; Kang, C.-F.; He, J.-H.; Bakr, O. M.; Wu, T., Schottky junctions on perovskite single crystals: light-modulated dielectric constant and self-biased photodetection. *J Mater Chem C* **2016**, 4 (35), 8304-8312.
66. Sheikh, M. S.; Sakhya, A. P.; Dutta, A.; Sinha, T. P., Dielectric relaxation of CH<sub>3</sub>NH<sub>3</sub>PbI<sub>3</sub> thin film. *Thin Solid Films* **2017**, 638, 277-281.
67. Uchino, K.; Nomura, S.; Cross, L. E.; Jang, S. J.; Newnham, R. E., Electrostrictive effect in lead magnesium niobate single crystals. *Journal of Applied Physics* **1980**, 51 (2), 1142-1145.



68. Cross, L. E.; Jang, S. J.; Newnham, R. E.; Nomura, S.; Uchino, K., Large electrostrictive effects in relaxor ferroelectrics. *Ferroelectrics* **1980**, *23* (1), 187-191.
69. Zhang, Q. M.; Bharti, V. V.; Zhao, X., Giant electrostriction and relaxor ferroelectric behavior in electron-irradiated poly(vinylidene fluoride-trifluoroethylene) copolymer. *Science* **1998**, *280* (5372), 2101-4.
70. Zhang, Q. M.; Li, H.; Poh, M.; Xia, F.; Cheng, Z. Y.; Xu, H.; Huang, C., An all-organic composite actuator material with a high dielectric constant. *Nature* **2002**, *419* (6904), 284-287.
71. Li, F.; Jin, L.; Xu, Z.; Zhang, S., Electrostrictive effect in ferroelectrics: An alternative approach to improve piezoelectricity. *Applied Physics Reviews* **2014**, *1* (1), 011103.
72. Li, F.; Jin, L.; Xu, Z.; Wang, D.; Zhang, S., Electrostrictive effect in  $\text{Pb}(\text{Mg}_{1/3}\text{Nb}_{2/3})\text{O}_3$ - $x\text{PbTiO}_3$  crystals. *Appl Phys Lett* **2013**, *102* (15), 152910.
73. Gao, J.; Xu, Z.; Li, F.; Zhang, C.; Li, Z.; Wu, X.; Wang, L.; Liu, Y.; Liu, G.; He, H., Pyroelectric properties of rhombohedral and tetragonal  $\text{Pb}(\text{In}_{1/2}\text{Nb}_{1/2})$ - $\text{Pb}(\text{Mg}_{1/3}\text{Nb}_{2/3})$ - $\text{PbTiO}_3$  crystals. *Journal of Applied Physics* **2011**, *110* (10), 106101.
74. Misture, S. T.; Pilgrim, S. M.; Hicks, J. C.; Blue, C. T.; Payzant, E. A.; Hubbard, C. R., Measurement of the electrostrictive coefficients of modified lead magnesium niobate using neutron powder diffraction. *Appl Phys Lett* **1998**, *72* (9), 1042-1044.
75. Craciun, F., Strong variation of electrostrictive coupling near an intermediate temperature of relaxor ferroelectrics. *Phys Rev B* **2010**, *81* (18).
76. Pelrine, R. E.; Kornbluh, R. D.; Joseph, J. P., Electrostriction of polymer dielectrics with compliant electrodes as a means of actuation. *Sensor Actuat a-Phys* **1998**, *64* (1), 77-85.
77. Yavo, N.; Smith, A. D.; Yeheskel, O.; Cohen, S.; Korobko, R.; Wachtel, E.; Slater, P. R.; Lubomirsky, I., Large Nonclassical Electrostriction in (Y, Nb)-Stabilized  $\delta$ - $\text{Bi}_2\text{O}_3$ . *Adv Funct Mater* **2016**, *26* (7), 1138-1142.
78. Yavo, N.; Yeheskel, O.; Wachtel, E.; Ehre, D.; Frenkel, A. I.; Lubomirsky, I., Relaxation and saturation of electrostriction in 10 mol% Gd-doped ceria ceramics. *Acta Mater* **2018**, *144*, 411-418.
79. Korobko, R.; Lerner, A.; Li, Y.; Wachtel, E.; Frenkel, A. I.; Lubomirsky, I., In-situ extended X-ray absorption fine structure study of electrostriction in Gd doped ceria. *Appl Phys Lett* **2015**, *106* (4), 042904.
80. Chen, B.; Li, T.; Dong, Q.; Mosconi, E.; Song, J.; Chen, Z.; Deng, Y.; Liu, Y.; Ducharme, S.;

- Gruverman, A.; Angelis, F.; Huang, J., Large electrostrictive response in lead halide perovskites. *Nat Mater* **2018**, *17* (11), 1020-1026.
81. Dong, Q.; Song, J.; Fang, Y.; Shao, Y.; Ducharme, S.; Huang, J., Lateral-Structure Single-Crystal Hybrid Perovskite Solar Cells via Piezoelectric Poling. *Adv Mater* **2016**, *28* (14), 2816-21.
82. Coll, M.; Gomez, A.; Mas-Marza, E.; Almora, O.; Garcia-Belmonte, G.; Campoy-Quiles, M.; Bisquert, J., Polarization Switching and Light-Enhanced Piezoelectricity in Lead Halide Perovskites. *Journal of Physical Chemistry Letters* **2015**, *6* (8), 1408-1413.
83. Kholkin, A. L.; Iakovlev, S. O.; Baptista, J. L., Direct effect of illumination on ferroelectric properties of lead zirconate titanate thin films. *Appl Phys Lett* **2001**, *79* (13), 2055-2057.
84. Kholkin, A. L.; Setter, N., Photoinduced poling of lead titanate zirconate thin films. *Appl Phys Lett* **1997**, *71* (19), 2854-2856.
85. Song, J.; Xiao, Z.; Chen, B.; Prockish, S.; Chen, X.; Rajapitamahuni, A.; Zhang, L.; Huang, J.; Hong, X., Enhanced Piezoelectric Response in Hybrid Lead Halide Perovskite Thin Films via Interfacing with Ferroelectric PbZr<sub>0.2</sub>Ti<sub>0.8</sub>O<sub>3</sub>. *ACS Appl Mater Interfaces* **2018**, *10* (22), 19218-19225.
86. Kim, Y. J.; Dang, T. V.; Choi, H. J.; Park, B. J.; Eom, J. H.; Song, H. A.; Seol, D.; Kim, Y.; Shin, S. H.; Nah, J.; Yoon, S. G., Piezoelectric properties of CH<sub>3</sub>NH<sub>3</sub>PbI<sub>3</sub> perovskite thin films and their applications in piezoelectric generators. *Journal of Materials Chemistry A* **2016**, *4* (3), 756-763.
87. Ippili, S.; Jella, V.; Kim, J.; Hong, S.; Yoon, S.-G., Enhanced piezoelectric output performance via control of dielectrics in Fe<sup>2+</sup>-incorporated MAPbI<sub>3</sub> perovskite thin films: Flexible piezoelectric generators. *Nano Energy* **2018**, *49*, 247-256.
88. Ding, R.; Liu, H.; Zhang, X. L.; Xiao, J. X.; Kishor, R.; Sun, H. X.; Zhu, B. W.; Chen, G.; Gao, F.; Feng, X. H.; Chen, J. S.; Chen, X. D.; Sun, X. W.; Zheng, Y. J., Flexible Piezoelectric Nanocomposite Generators Based on Formamidinium Lead Halide Perovskite Nanoparticles. *Adv Funct Mater* **2016**, *26* (42), 7708-7716.
89. Abdollahi, A.; Domingo, N.; Arias, I.; Catalan, G., Converse flexoelectricity yields large piezoresponse force microscopy signals in non-piezoelectric materials. *Nat Commun* **2019**, *10* (1), 1266.
90. Morozovska, A. N.; Eliseev, E. A.; Balke, N.; Kalinin, S. V., Local probing of ionic diffusion

by electrochemical strain microscopy: Spatial resolution and signal formation mechanisms. *Journal of Applied Physics* **2010**, *108* (5), 053712.

91. Zeng, Q.; Wang, H.; Xiong, Z.; Huang, Q.; Lu, W.; Sun, K.; Fan, Z.; Zeng, K., Nanoscale Ferroelectric Characterization with Heterodyne Megasonic Piezoresponse Force Microscopy. *Advanced Science* **2021**, 2003993.

92. J.-M. Liu , B. P., H.L.W. Chan, S.N. Zhu, Y.Y. Zhu, Z.G. Liu, Piezoelectric coefficient measurement of piezoelectric thin films: an overview. *Materials Chemistry and Physics* **2002**, *75* (1-3), 12-18.

93. Du, H.-l.; Tang, F.-s.; Li, Z.-m.; Zhou, W.-c.; Qu, S.-b.; Pei, Z.-b., Effect of poling condition on piezoelectric properties of  $(\text{K}_{0.5}\text{Na}_{0.5})\text{NbO}_3$  ceramics. *Transactions of Nonferrous Metals Society of China* **2006**, *16*, s462-s465.

94. Kim, D. B.; Park, K. H.; Cho, Y. S., Origin of high piezoelectricity of inorganic halide perovskite thin films and their electromechanical energy-harvesting and physiological current-sensing characteristics. *Energy & Environmental Science* **2020**, *13*.

95. Kawamura, Y.; Mashiyama, H.; Hasebe, K., Structural Study on Cubic–Tetragonal Transition of  $\text{CH}_3\text{NH}_3\text{PbI}_3$ . *J Phys Soc Jpn* **2002**, *71* (7), 1694-1697.

96. Poglitsch, A.; Weber, D., Dynamic disorder in methylammoniumtrihalogenoplumbates (II) observed by millimeter-wave spectroscopy. *The Journal of Chemical Physics* **1987**, *87* (11), 6373-6378.

97. Stoumpos, C. C.; Malliakas, C. D.; Kanatzidis, M. G., Semiconducting tin and lead iodide perovskites with organic cations: phase transitions, high mobilities, and near-infrared photoluminescent properties. *Inorg Chem* **2013**, *52* (15), 9019-38.

98. Rothmann, M. U.; Li, W.; Zhu, Y.; Bach, U.; Spiccia, L.; Etheridge, J.; Cheng, Y. B., Direct observation of intrinsic twin domains in tetragonal  $\text{CH}_3\text{NH}_3\text{PbI}_3$ . *Nat Commun* **2017**, *8*.

99. Sharada, G.; Mahale, P.; Kore, B. P.; Mukherjee, S.; Pavan, M. S.; De, C. D.; Ghara, S.; Sundaresan, A.; Pandey, A.; Row, T. N. G.; Sarma, D. D., Is  $\text{CH}_3\text{NH}_3\text{PbI}_3$  Polar? *Journal of Physical Chemistry Letters* **2016**, *7* (13), 2412-2419.

100. Fan, Z.; Xiao, J.; Sun, K.; Chen, L.; Hu, Y.; Ouyang, J.; Ong, K. P.; Zeng, K.; Wang, J., Ferroelectricity of  $\text{CH}_3\text{NH}_3\text{PbI}_3$  Perovskite. *J Phys Chem Lett* **2015**, *6* (7), 1155-61.

101. Sajedi Alvar, M.; Kumar, M.; Blom, P. W. M.; Wetzelaer, G.-J. A. H.; Asadi, K., Absence of

- ferroelectricity in methylammonium lead iodide perovskite. *Aip Adv* **2017**, 7 (9).
102. Yamada, Y.; Yamada, T.; Phuong le, Q.; Maruyama, N.; Nishimura, H.; Wakamiya, A.; Murata, Y.; Kanemitsu, Y., Dynamic Optical Properties of CH<sub>3</sub>NH<sub>3</sub>PbI<sub>3</sub> Single Crystals As Revealed by One- and Two-Photon Excited Photoluminescence Measurements. *J Am Chem Soc* **2015**, 137 (33), 10456-9.
103. Wang, F. F.; Meng, D. C.; Li, X. N.; Zhu, Z.; Fu, Z. P.; Lu, Y. L., Influence of annealing temperature on the crystallization and ferroelectricity of perovskite CH<sub>3</sub>NH<sub>3</sub>PbI<sub>3</sub> film. *Appl Surf Sci* **2015**, 357, 391-396.
104. Kim, H. S.; Kim, S. K.; Kim, B. J.; Shin, K. S.; Gupta, M. K.; Jung, H. S.; Kim, S. W.; Park, N. G., Ferroelectric Polarization in CH<sub>3</sub>NH<sub>3</sub>PbI<sub>3</sub> Perovskite. *Journal of Physical Chemistry Letters* **2015**, 6 (9), 1729-1735.
105. Zhao, Y.-Q.; Liu, B.; Yu, Z.-L.; Ma, J.; Qiang Wan, Q. W.; He, P.-b.; Cai, M.-Q., Strong ferroelectric polarization of CH<sub>3</sub>NH<sub>3</sub>GeI<sub>3</sub> with high-absorption and mobility transport anisotropy: theoretical study. *J Mater Chem C* **2017**, 5 (22), 5356-5364.
106. Frost, J. M.; Butler, K. T.; Brivio, F.; Hendon, C. H.; van Schilfgaarde, M.; Walsh, A., Atomistic Origins of High-Performance in Hybrid Halide Perovskite Solar Cells. *Nano Letters* **2014**, 14 (5), 2584-2590.
107. Quarti, C.; Mosconi, E.; De Angelis, F., Interplay of Orientational Order and Electronic Structure in Methylammonium Lead Iodide: Implications for Solar Cell Operation. *Chem Mater* **2014**, 26 (22), 6557-6569.
108. Stroppa, A.; Quarti, C.; De Angelis, F.; Picozzi, S., Ferroelectric Polarization of CH<sub>3</sub>NH<sub>3</sub>PbI<sub>3</sub>: A Detailed Study Based on Density Functional Theory and Symmetry Mode Analysis. *Journal of Physical Chemistry Letters* **2015**, 6 (12), 2223-2231.
109. Yan, W. L.; Lu, G. H.; Liu, F., Effect of Chlorine Substitution on Lattice Distortion and Ferroelectricity of CH<sub>3</sub>NH<sub>3</sub>PbI<sub>3</sub>. *J Phys Chem C* **2016**, 120 (32), 17972-17977.
110. Berdiyrov, G. R.; El-Mellouhi, F.; Madjet, M. E.; Alharbi, F. H.; Rashkeev, S. N., Electronic transport in organometallic perovskite CH<sub>3</sub>NH<sub>3</sub>PbI<sub>3</sub>: The role of organic cation orientations. *Appl Phys Lett* **2016**, 108 (5).
111. Solmaz, A.; Huijben, M.; Koster, G.; Egoavil, R.; Gauquelin, N.; Van Tendeloo, G.; Verbeeck, J.; Noheda, B.; Rijnders, G., Domain Selectivity in BiFeO<sub>3</sub> Thin Films by Modified Substrate

- Termination. *Adv Funct Mater* **2016**, 26 (17), 2882-2889.
112. Feng, H. J., Ferroelectric polarization driven optical absorption and charge carrier transport in  $\text{CH}_3\text{NH}_3\text{PbI}_3/\text{TiO}_2$ -based photovoltaic cells. *Journal of Power Sources* **2015**, 291, 58-65.
113. Rashkeev, S. N.; El-Mellouhi, F.; Kais, S.; Alharbi, F. H., Domain Walls Conductivity in Hybrid Organometallic Perovskites and Their Essential Role in  $\text{CH}_3\text{NH}_3\text{PbI}_3$  Solar Cell High Performance. *Sci Rep-Uk* **2015**, 5, 11465.
114. Chen, B.; Zheng, X.; Yang, M.; Zhou, Y.; Kundu, S.; Shi, J.; Zhu, K.; Priya, S., Interface band structure engineering by ferroelectric polarization in perovskite solar cells. *Nano Energy* **2015**, 13, 582-591.
115. Rohm, H.; Leonhard, T.; Hoffmann, M. J.; Colmann, A., Ferroelectric domains in methylammonium lead iodide perovskite thin-films. *Energy & Environmental Science* **2017**, 10 (4), 950-955.
116. Otoničar, M.; Škapin, S. D.; Jančar, B.; Ubic, R.; Suvorov, D., Analysis of the Phase Transition and the Domain Structure in  $\text{K}_{0.5}\text{Bi}_{0.5}\text{TiO}_3$  Perovskite Ceramics by In Situ XRD and TEM. *Journal of the American Ceramic Society* **2010**, 93 (12), 4168-4173.
117. Hermes, I. M.; Bretschneider, S. A.; Bergmann, V. W.; Li, D.; Klasen, A.; Mars, J.; Tremel, W.; Laquai, F.; Butt, H. J.; Mezger, M.; Berger, R.; Rodriguez, B. J.; Weber, S. A. L., Ferroelastic Fingerprints in Methylammonium Lead Iodide Perovskite. *J Phys Chem C* **2016**, 120 (10), 5724-5731.
118. Huang, B.; Kong, G.; Esfahani, E. N.; Chen, S.; Li, Q.; Yu, J.; Xu, N.; Zhang, Y.; Xie, S.; Wen, H.; Gao, P.; Zhao, J.; Li, J., Ferroic domains regulate photocurrent in single-crystalline  $\text{CH}_3\text{NH}_3\text{PbI}_3$  films self-grown on FTO/ $\text{TiO}_2$  substrate. *npj Quantum Materials* **2018**, 3 (1).
119. Yu, M.; Yuan, S.; Wang, H. Y.; Zhao, J. S.; Qin, Y. J.; Fu, L. M.; Zhang, J. P.; Ai, X. C., Characterization of the influences of morphology on the intrinsic properties of perovskite films by temperature-dependent and time-resolved spectroscopies. *Physical Chemistry Chemical Physics* **2018**, 20 (9), 6575-6581.
120. Onoda-Yamamuro, N.; Matsuo, T. & Suga, H., Calorimetric and IR spectroscopic studies of phase transitions in methylammonium trihalogenplumbates (II). *J. Phys. Cem. Solids* **1990**, 51, 1383.
121. Fujishima, A.; Zhang, X.; Tryk, D.,  $\text{TiO}_2$  photocatalysis and related surface phenomena. *Surface Science Reports* **2008**, 63 (12), 515-582.

122. Samadi-maybodi, A.; Abbasi, F.; Akhoondi, R., Aqueous synthesis and characterization of CdS quantum dots capped with some amino acids and investigations of their photocatalytic activities. *Colloids and Surfaces A: Physicochemical and Engineering Aspects* **2014**, *447*, 111-119.
123. Anil Kumar, A. K. J., Photophysics and photochemistry of colloidal CdS–TiO<sub>2</sub> coupled semiconductors — photocatalytic oxidation of indole. *Journal of Molecular Catalysis A: Chemical* **2001**, *165*, 265-273.
124. Nayak, J.; Sahu, S. N.; Kasuya, J.; Nozaki, S., CdS–ZnO composite nanorods: Synthesis, characterization and application for photocatalytic degradation of 3,4-dihydroxy benzoic acid. *Appl Surf Sci* **2008**, *254* (22), 7215-7218.
125. Lou, Q.; Zeng, J.; Man, Z.; Zheng, L.; Park, C.; Li, G., Effect of Ba:Ti on ferroelectric properties of LiF doped BaTiO<sub>3</sub> ceramics. *Journal of Materials Science: Materials in Electronics* **2019**, *30* (7), 6556-6563.
126. Rahman, Q. I.; Ahmad, M.; Misra, S. K.; Lohani, M., Efficient degradation of Methylene Blue dye over highly reactive Cu doped strontium titanate (SrTiO<sub>3</sub>) nanoparticles photocatalyst under visible light. *J Nanosci Nanotechnol* **2012**, *12* (9), 7181-6.
127. Wei, W.; Hu, Y. H., Catalytic role of H<sub>2</sub>O in degradation of inorganic-organic perovskite (CH<sub>3</sub>NH<sub>3</sub>PbI<sub>3</sub>) in air. *International Journal of Energy Research* **2017**, *41* (7), 1063-1069.
128. Wang, C.; Zhang, C.; Huang, Y.; Tong, S.; Wu, H.; Zhang, J.; Gao, Y.; Yang, J., Degradation behavior of planar heterojunction CH<sub>3</sub>NH<sub>3</sub>PbI<sub>3</sub> perovskite solar cells. *Synthetic Metals* **2017**, *227*, 43-51.
129. Chen, Y. S.; Manser, J. S.; Kamat, P. V., All solution-processed lead halide perovskite-BiVO<sub>4</sub> tandem assembly for photolytic solar fuels production. *J Am Chem Soc* **2015**, *137* (2), 974-81.
130. Luo, J.; Im, J. H.; Mayer, M. T.; Schreier, M.; Nazeeruddin, M. K.; Park, N. G.; Tilley, S. D.; Fan, H. J.; Gratzel, M., Water photolysis at 12.3% efficiency via perovskite photovoltaics and Earth-abundant catalysts. *Science* **2014**, *345* (6204), 1593-6.
131. Crespo-Quesada, M.; Pazos-Outon, L. M.; Warnan, J.; Kuehnle, M. F.; Friend, R. H.; Reisner, E., Metal-encapsulated organolead halide perovskite photocathode for solar-driven hydrogen evolution in water. *Nat Commun* **2016**, *7*, 12555.
132. Park, S.; Chang, W. J.; Lee, C. W.; Park, S.; Ahn, H.-Y.; Nam, K. T., Photocatalytic hydrogen generation from hydriodic acid using methylammonium lead iodide in dynamic equilibrium with

- aqueous solution. *Nature Energy* **2016**, 2 (1).
133. Huang, H.; Yuan, H.; Janssen, K. P. F.; Solís-Fernández, G.; Wang, Y.; Tan, C. Y. X.; Jonckheere, D.; Debroye, E.; Long, J.; Hendrix, J.; Hofkens, J.; Steele, J. A.; Roeffaers, M. B. J., Efficient and Selective Photocatalytic Oxidation of Benzylic Alcohols with Hybrid Organic–Inorganic Perovskite Materials. *ACS Energy Letters* **2018**, 3 (4), 755-759.
134. Andrew Mills, S. L. H., An overview of semiconductor photocatalysis. *Journal of Photochemistry and Photobiology A: Chemistry* **1997**, 108, 1-35.
135. Saidaminov, M. I.; Abdelhady, A. L.; Murali, B.; Alarousu, E.; Burlakov, V. M.; Peng, W.; Dursun, I.; Wang, L.; He, Y.; Maculan, G.; Goriely, A.; Wu, T.; Mohammed, O. F.; Bakr, O. M., High-quality bulk hybrid perovskite single crystals within minutes by inverse temperature crystallization. *Nat Commun* **2015**, 6, 7586.
136. Yoshimura, T.; Fujimura, a. N., Polarization Hysteresis Loops of Ferroelectric Gate Capacitors Measured by Sawyer-Tower Circuit. *The Japan Society of Applied Physics* **2003**, 42, 6011-6014.
137. Vasudevan, R. K.; Balke, N.; Maksymovych, P.; Jesse, S.; Kalinin, S. V., Ferroelectric or non-ferroelectric: Why so many materials exhibit “ferroelectricity” on the nanoscale. *Applied Physics Reviews* **2017**, 4 (2), 021302.
138. Wei, J.; Zhao, Y. C.; Li, H.; Li, G. B.; Pan, J. L.; Xu, D. S.; Zhao, Q.; Yu, D. P., Hysteresis Analysis Based on the Ferroelectric Effect in Hybrid Perovskite Solar Cells. *Journal of Physical Chemistry Letters* **2014**, 5 (21), 3937-3945.
139. Lee, J.-W.; Kim, S.-G.; Bae, S.-H.; Lee, D.-K.; Lin, O.; Yang, Y.; Park, N.-G., The Interplay between Trap Density and Hysteresis in Planar Heterojunction Perovskite Solar Cells. *Nano Letters* **2017**, 17 (7), 4270-4276.
140. Meloni, S.; Moehl, T.; Tress, W.; Franckevičius, M.; Saliba, M.; Lee, Y. H.; Gao, P.; Nazeeruddin, M. K.; Zakeeruddin, S. M.; Rothlisberger, U.; Graetzel, M., Ionic polarization-induced current-voltage hysteresis in CH<sub>3</sub>NH<sub>3</sub>PbX<sub>3</sub> perovskite solar cells. *Nat Commun* **2016**, 7 (1), 10334.
141. Gómez, A.; Wang, Q.; Goñi, A. R.; Campoy-Quiles, M.; Abate, A., Ferroelectricity-free lead halide perovskites. *Energy & Environmental Science* **2019**, 12 (8), 2537-2547.
142. Beilsten-Edmands, J.; Eperon, G. E.; Johnson, R. D.; Snaith, H. J.; Radaelli, P. G., Non-ferroelectric nature of the conductance hysteresis in CH<sub>3</sub>NH<sub>3</sub>PbI<sub>3</sub> perovskite-based photovoltaic

devices. *Appl Phys Lett* **2015**, *106* (17), 173502.

143. Dam, T.; Jena, S. S.; Pradhan, D. K., The ionic transport mechanism and coupling between the ion conduction and segmental relaxation processes of PEO<sub>20</sub>-LiCF<sub>3</sub>SO<sub>3</sub> based ion conducting polymer clay composites. *Phys Chem Chem Phys* **2016**, *18* (29), 19955-19965.

144. Jaschin, P. W.; Varma, K. B. R., Lithium ion conductivity and dielectric relaxation in dendritic nanostructured LiTaO<sub>3</sub> glass–nanocrystal composites. *Journal of Applied Physics* **2017**, *121* (9), 094101.

145. Almora, O.; Zarazua, I.; Mas-Marza, E.; Mora-Sero, I.; Bisquert, J.; Garcia-Belmonte, G., Capacitive Dark Currents, Hysteresis, and Electrode Polarization in Lead Halide Perovskite Solar Cells. *J Phys Chem Lett* **2015**, *6* (9), 1645-1652.

146. A. Pimenov , J. U., P. Lunkenheimer , A. Loidl , C.H. Ruscherb, Ionic conductivity and relaxations in ZrO<sub>2</sub>–Y<sub>2</sub>O<sub>3</sub> solid solutions. *Solid State Ionics* **1998**, *109* 111–118.

147. Yamamura, H.; Takeda, S.; Kakinuma, K., Relationship between oxide-ion conductivity and dielectric relaxation in Sm-doped CeO<sub>2</sub>. *Solid State Ionics* **2007**, *178* (13-14), 889-893.

148. Cole, K. S.; Cole, R. H., Dispersion and Absorption in Dielectrics I. Alternating Current Characteristics. *The Journal of Chemical Physics* **1941**, *9* (4), 341-351.

149. Abdelkafi, Z.; Abdelmoula, N.; Khemakhem, H.; Bidault, O.; Maglione, M., Dielectric relaxation in BaTi<sub>0.85</sub>(Fe<sub>1/2</sub>Nb<sub>1/2</sub>)<sub>0.15</sub>O<sub>3</sub> perovskite ceramic. *Journal of Applied Physics* **2006**, *100* (11), 114111.

150. Herz, L. M., How Lattice Dynamics Moderate the Electronic Properties of Metal-Halide Perovskites. *J Phys Chem Lett* **2018**, *9* (23), 6853-6863.

151. Namrata Shukla, Awalendra K. Thakur, Archana Shukla, David T. Marx, Ion Conduction Mechanism in Solid Polymer Electrolyte: An Applicability of Almond-West Formalism. *Int. J. Electrochem. Sci* **2014**, *9*, 7644-7659.

152. Karan, N.; Pradhan, D.; Thomas, R.; Natesan, B.; Katiyar, R., Solid polymer electrolytes based on polyethylene oxide and lithium trifluoro- methane sulfonate (PEO–LiCF<sub>3</sub>SO<sub>3</sub>): Ionic conductivity and dielectric relaxation. *Solid State Ionics* **2008**, *179* (19-20), 689-696.

153. Aakansha; Dekka, B.; Ravi, S.; Pamu, D., Impedance spectroscopy and ac conductivity mechanism in Sm doped Yttrium Iron Garnet. *Ceram Int* **2017**, *43* (13), 10468-10477.

154. Khamzin, A. A.; Popov, II; Nigmatullin, R. R., Correction of the power law of ac conductivity



in ion-conducting materials due to the electrode polarization effect. *Phys Rev E Stat Nonlin Soft Matter Phys* **2014**, *89* (3), 032303.

155. R.H. Chen\*, R. Y. C., S.C. Shern, Dielectric and AC ionic conductivity investigations in  $\text{K}_3\text{H}(\text{SeO}_4)_2$  single crystal. *Journal of Physics and Chemistry of Solids* **2002**, *63*, 2069-2077.

156. Murugave, A. B. a. S., Small polaron hopping conduction mechanism in  $\text{LiFePO}_4$  glass and crystal. *Journal of Applied Physics* **2017**, *121* (5), 045111.

157. Zhang, L.; Tang, Z.-J., Polaron relaxation and variable-range-hopping conductivity in the giant-dielectric-constant material  $\text{CaCu}_3\text{Ti}_4\text{O}_{12}$ . *Phys Rev B* **2004**, *70* (17), 174306.

158. Junichiro MIZUSAKI, K. A. a. K. F., IONIC CONDUCTION OF THE PEROVSKITE-TYPE HALIDES. *Solid State Ionics* **1983**, *11*, 203-211.

159. R.H. Chena, C. S. S., T. Fukamib, Frequency dependence of ionic conductivity and dielectric relaxation studies in  $\text{Na}_3\text{H}(\text{SO}_4)_2$  single crystal. *Journal of Physics and Chemistry of Solids* **2002**, *63* (2), 203-212.

160. Haruyama, J.; Sodeyama, K.; Han, L.; Tateyama, Y., First-Principles Study of Ion Diffusion in Perovskite Solar Cell Sensitizers. *J Am Chem Soc* **2015**, *137* (32), 10048-51.

161. Zhao, Y.-C.; Zhou, W.-K.; Zhou, X.; Liu, K.-H.; Yu, D.-P.; Zhao, Q., Quantification of light-enhanced ionic transport in lead iodide perovskite thin films and its solar cell applications. *Light-Science & Applications* **2017**, *6*.

162. Ong, K. P.; Goh, T. W.; Xu, Q.; Huan, A., Structural Evolution in Methylammonium Lead Iodide  $\text{CH}_3\text{NH}_3\text{PbI}_3$ . *J Phys Chem A* **2015**, *119* (44), 11033-8.

163. Trainer, M., Ferroelectricity: Measurement of the dielectric susceptibility of strontium titanate at low temperatures. *American Journal of Physics* **2001**, *69* (9), 966-969.

164. Onodayamamuro, N.; Matsuo, T.; Suga, H., DIELECTRIC STUDY OF  $\text{CH}_3\text{NH}_3\text{PBX}_3$  (X=CL, BR, I). *Journal of Physics and Chemistry of Solids* **1992**, *53* (7), 935-939.

165. Zheng, F.; Takenaka, H.; Wang, F. G.; Koocher, N. Z.; Rappe, A. M., First-Principles Calculation of the Bulk Photovoltaic Effect in  $\text{CH}_3\text{NH}_3\text{PbI}_3$  and  $\text{CH}_3\text{NH}_3\text{PbI}_{3-x}\text{Cl}_x$ . *Journal of Physical Chemistry Letters* **2015**, *6* (1), 31-37.

166. Sherkar, T. S.; Koster, L. J. A., Can ferroelectric polarization explain the high performance of hybrid halide perovskite solar cells? *Physical Chemistry Chemical Physics* **2016**, *18* (1), 331-338.

167. Liu, S.; Zheng, F.; Koocher, N. Z.; Takenaka, H.; Wang, F.; Rappe, A. M., Ferroelectric Domain

- Wall Induced Band Gap Reduction and Charge Separation in Organometal Halide Perovskites. *J Phys Chem Lett* **2015**, 6 (4), 693-639.
168. Choi, H.; Jeong, J.; Kim, H.-B.; Kim, S.; Walker, B.; Kim, G.-H.; Kim, J. Y., Cesium-doped methylammonium lead iodide perovskite light absorber for hybrid solar cells. *Nano Energy* **2014**, 7, 80-85.
169. Taya, A.; Rani, P.; Thakur, J.; Kashyap, M. K., First principles study of structural, electronic and optical properties of Cs-doped  $\text{CH}_3\text{NH}_3\text{PbI}_3$  for photovoltaic applications. *Vacuum* **2019**, 160, 440-444.
170. Gakhar, R.; Summers, K.; Palaniappan, R.; Pilli, S. K.; Chidambaram, D., Sensitization of  $\text{TiO}_2$  nanotube array photoelectrodes with  $\text{Mn}_x\text{Cd}_y\text{Se}$ . *RSC Adv.* **2014**, 4 (91), 49729-49736.
171. Li, X.; Zhu, H.; Wei, J.; Wang, K.; Xu, E.; Li, Z.; Wu, D., Determination of band gaps of self-assembled carbon nanotube films using Tauc/Davis–Mott model. *Applied Physics A* **2009**, 97 (2), 341-344.
172. Egger, D. A.; Kronik, L., Role of Dispersive Interactions in Determining Structural Properties of Organic-Inorganic Halide Perovskites: Insights from First-Principles Calculations. *J Phys Chem Lett* **2014**, 5 (15), 2728-2733.
173. Arakcheeva, A.; Chernyshov, D.; Spina, M.; Forro, L.; Horvath, E.,  $\text{CH}_3\text{NH}_3\text{PbI}_3$ : precise structural consequences of water absorption at ambient conditions. *Acta Crystallogr B Struct Sci Cryst Eng Mater* **2016**, 72 (Pt 5), 716-722.
174. Zhou, Y.; Garces, H. F.; Padture, N. P., Challenges in the ambient Raman spectroscopy characterization of methylammonium lead triiodide perovskite thin films. *Frontiers of Optoelectronics* **2016**, 9 (1), 81-86.
175. A Gibaudi, T. W. R. a. R. J. N., Critical fluctuations in  $\text{RbCaF}_3$ . I. A high-resolution X-ray scattering study. **1987**, 20, 3833-3848.
176. Segovia, R.; Qu, G. Y.; Peng, M.; Sun, X. D.; Shi, H. Y.; Gao, B., Evolution of Photoluminescence, Raman, and Structure of  $\text{CH}_3\text{NH}_3\text{PbI}_3$  Perovskite Microwires Under Humidity Exposure. *Nanoscale Research Letters* **2018**, 13.
177. Colomban, P.; Slodczyk, A., Raman intensity: An important tool to study the structure and phase transitions of amorphous/crystalline materials. *Optical Materials* **2009**, 31 (12), 1759-1763.
178. Song, Z.; Abate, A.; Wathage, S. C.; Liyanage, G. K.; Phillips, A. B.; Steiner, U.; Graetzel, M.;

- Heben, M. J., Perovskite Solar Cell Stability in Humid Air: Partially Reversible Phase Transitions in the  $\text{PbI}_2\text{-CH}_3\text{NH}_3\text{I-H}_2\text{O}$  System. *Advanced Energy Materials* **2016**, 6 (19).
179. Quarti, C.; Grancini, G.; Mosconi, E.; Bruno, P.; Ball, J. M.; Lee, M. M.; Snaith, H. J.; Petrozza, A.; De Angelis, F., The Raman Spectrum of the  $\text{CH}_3\text{NH}_3\text{PbI}_3$  Hybrid Perovskite: Interplay of Theory and Experiment. *Journal of Physical Chemistry Letters* **2014**, 5 (2), 279-284.
180. Ledinsky, M.; Loper, P.; Niesen, B.; Holovsky, J.; Moon, S. J.; Yum, J. H.; De Wolf, S.; Fejfar, A.; Ballif, C., Raman Spectroscopy of Organic-Inorganic Halide Perovskites. *J Phys Chem Lett* **2015**, 6 (3), 401-6.
181. Nakada, K.; Matsumoto, Y.; Shimoi, Y.; Yamada, K.; Furukawa, Y., Temperature-Dependent Evolution of Raman Spectra of Methylammonium Lead Halide Perovskites,  $\text{CH}_3\text{NH}_3\text{PbX}_3$  ( $\text{X} = \text{I}, \text{Br}$ ). *Molecules* **2019**, 24 (3).
182. Tanja Ivanovska; Claudio Quarti; Grancini, G.; Petrozza, A.; Angelis, F. D.; Alberto Milani; Ruani, G., Vibrational Response of Methylammonium Lead Iodide From Cation Dynamics to Phonon–Phonon Interactions. *ChemSusChem* **2016**, 9, 1-12.
183. Li, W.; Man, Z.; Zeng, J.; Zheng, L.; Li, G.; Kassiba, A., Relationship of Giant Dielectric Constant and Ion Migration in  $\text{CH}_3\text{NH}_3\text{PbI}_3$  Single Crystal Using Dielectric Spectroscopy. *The Journal of Physical Chemistry C* **2020**, 124 (24), 13348-13355.
184. Zhang, Q. M.; Pan, W. Y.; Cross, L. E., Laser interferometer for the study of piezoelectric and electrostrictive strains. *Journal of Applied Physics* **1988**, 63 (8), 2492-2496.
185. Zhang, Q. M.; Jang, S. J.; Cross, L. E., High-frequency strain response in ferroelectrics and its measurement using a modified Mach-Zehnder interferometer. *Journal of Applied Physics* **1989**, 65 (7), 2807-2813.
186. Ushakov, A. D.; Mishuk, E.; Makagon, E.; Alikin, D. O.; Esin, A. A.; Baturin, I. S.; Tselev, A.; Shur, V. Y.; Lubomirsky, I.; Kholkin, A. L., Electromechanical properties of electrostrictive  $\text{CeO}_2\text{:Gd}$  membranes: Effects of frequency and temperature. *Appl Phys Lett* **2017**, 110 (14), 142902.
187. Frohna, K.; Deshpande, T.; Harter, J.; Peng, W.; Barker, B. A.; Neaton, J. B.; Louie, S. G.; Bakr, O. M.; Hsieh, D.; Bernardi, M., Inversion symmetry and bulk Rashba effect in methylammonium lead iodide perovskite single crystals. *Nat Commun* **2018**, 9 (1), 1829.
188. Li, W.; Liu, J.; Bai, F.-Q.; Zhang, H.-X.; Prezhdov, O. V., Hole Trapping by Iodine Interstitial Defects Decreases Free Carrier Losses in Perovskite Solar Cells: A Time-Domain Ab Initio Study.

*Acs Energy Letters* **2017**, 2 (6), 1270-1278.

189. Lu, J.; Klenov, D. O.; Stemmer, S., Influence of strain on the dielectric relaxation of pyrochlore bismuth zinc niobate thin films. *Appl Phys Lett* **2004**, 84 (6), 957-959.

190. Meggiolaro, D.; De Angelis, F., First-Principles Modeling of Defects in Lead Halide Perovskites: Best Practices and Open Issues. *ACS Energy Letters* **2018**, 3 (9), 2206-2222.

191. Jones, J. L.; Pramanick, A.; Nino, J. C.; Maziar Motahari, S.; Üstündag, E.; Daymond, M. R.; Oliver, E. C., 'Time-resolved and orientation-dependent electric-field-induced strains in lead zirconate titanate ceramics. *Appl Phys Lett* **2007**, 90 (17), 172909.

192. R. E. Newnham, V. S., R. Yimnirun, J. Su, and Q. M. Zhang, Electrostriction: Nonlinear Electromechanical Coupling in Solid Dielectrics. **1997**, 101, 10141-10150.

193. Korobko, R.; Patlolla, A.; Kossoy, A.; Wachtel, E.; Tuller, H. L.; Frenkel, A. I.; Lubomirsky, I., Giant electrostriction in Gd-doped ceria. *Adv Mater* **2012**, 24 (43), 5857-61.

194. Kim, J.; Lee, S. H.; Lee, J. H.; Hong, K. H., The Role of Intrinsic Defects in Methylammonium Lead Iodide Perovskite. *J Phys Chem Lett* **2014**, 5 (8), 1312-7.

195. Li, Z.; Xiao, C. X.; Yang, Y.; Harvey, S. P.; Kim, D. H.; Christians, J. A.; Yang, M. J.; Schulz, P.; Nanayakkara, S. U.; Jiang, C. S.; Luther, J. M.; Berry, J. J.; Beard, M. C.; Al-Jassim, M. M.; Zhu, K., Extrinsic ion migration in perovskite solar cells. *Energy & Environmental Science* **2017**, 10 (5), 1234-1242.

196. Steirer, K. X.; Schulz, P.; Teeter, G.; Stevanovic, V.; Yang, M.; Zhu, K.; Berry, J. J., Defect Tolerance in Methylammonium Lead Triiodide Perovskite. *ACS Energy Letters* **2016**, 1 (2), 360-366.

197. Kutes, Y.; Ye, L. H.; Zhou, Y. Y.; Pang, S. P.; Huey, B. D.; Padture, N. P., Direct Observation of Ferroelectric Domains in Solution-Processed CH<sub>3</sub>NH<sub>3</sub>PbI<sub>3</sub> Perovskite Thin Films. *Journal of Physical Chemistry Letters* **2014**, 5 (19), 3335-3339.

198. Chen, Y. F.; Tsai, Y. T.; Bassani, D. M.; Hirsch, L., Experimental evidence of the anti-parallel arrangement of methylammonium ions in perovskites. *Appl Phys Lett* **2016**, 109 (21).

199. Strelcov, E.; Dong, Q.; Li, T.; Chae, J.; Shao, Y.; Deng, Y.; Gruverman, A.; Huang, J.; Centrone, A., CH<sub>3</sub>NH<sub>3</sub>PbI<sub>3</sub> perovskites: Ferroelasticity revealed. *Sci Adv* **2017**, 3 (4), e1602165.

200. Semenova, O. I.; Yudanov, E. S.; Yeryukov, N. A.; Zhivodkov, Y. A.; Shamirzaev, T. S.; Maximovskiy, E. A.; Gromilov, S. A.; Troitskaia, I. B., Perovskite CH<sub>3</sub>NH<sub>3</sub>PbI<sub>3</sub> crystals and films.

Synthesis and characterization. *J Cryst Growth* **2017**, *462*, 45-49.

201. Wang, H.; Lei, J.; Gao, F.; Yang, Z.; Yang, D.; Jiang, J.; Li, J.; Hu, X.; Ren, X.; Liu, B.; Liu, J.; Lei, H.; Liu, Z.; Liu, S. F., Magnetic Field-Assisted Perovskite Film Preparation for Enhanced Performance of Solar Cells. *Acs Appl Mater Inter* **2017**.

202. Zhang, Y.; Lv, H.; Cui, C.; Xu, L.; Wang, P.; Wang, H.; Yu, X.; Xie, J.; Huang, J.; Tang, Z.; Yang, D., Enhanced optoelectronic quality of perovskite films with excess CH<sub>3</sub>NH<sub>3</sub>I for high-efficiency solar cells in ambient air. *Nanotechnology* **2017**, *28* (20), 205401-205401.

203. Jonscher, A. K., Dielectric relaxation in solids. *J. Phys. D: Appl. Phys* **1999**, (32), 57-70.

204. Swainson, I. P.; Hammond, R. P.; Soullière, C.; Knop, O.; Massa, W., Phase transitions in the perovskite methylammonium lead bromide, CH<sub>3</sub>ND<sub>3</sub>PbBr<sub>3</sub>. *J Solid State Chem* **2003**, *176* (1), 97-104.

205. Slonopas, A.; Foley, B. J.; Choi, J. J.; Gupta, M. C., Charge transport in bulk CH<sub>3</sub>NH<sub>3</sub>PbI<sub>3</sub> perovskite. *Journal of Applied Physics* **2016**, *119* (7).

206. Berhe, T. A.; Su, W. N.; Chen, C. H.; Pan, C. J.; Cheng, J. H.; Chen, H. M.; Tsai, M. C.; Chen, L. Y.; Dubale, A. A.; Hwang, B. J., Organometal halide perovskite solar cells: degradation and stability. *Energy & Environmental Science* **2016**, *9* (2), 323-356.

207. Aristidou, N.; Sanchez-Molina, I.; Chotchuangchutchaval, T.; Brown, M.; Martinez, L.; Rath, T.; Haque, S. A., The Role of Oxygen in the Degradation of Methylammonium Lead Trihalide Perovskite Photoactive Layers. *Angew Chem Int Ed Engl* **2015**, *54* (28), 8208-12.



## List of Figures

<b>Figure 1.1</b> The crystal structure of MAPbI <sub>3</sub> .....	2
<b>Figure 1.2</b> Structures of MAPbI <sub>3</sub> at five temperatures based upon refinement of neutron powder diffraction data <sup>[24]</sup> .....	4
<b>Figure 1.3</b> Electronic properties of the cubic phase .....	5
<b>Figure 1.4</b> (a) Migration path of I <sup>-</sup> ions along the I <sup>-</sup> -I <sup>-</sup> edge of the PbI <sub>6</sub> octahedron in the MAPbI <sub>3</sub> crystal calculated from density functional theory (DFT) method. (b) Illustration of the migration paths for I <sup>-</sup> ions (A), Pb <sup>2+</sup> ions (B, C), and MA <sup>+</sup> ions (D). (c) PTIR images of the distribution of MA <sup>+</sup> before and after electrical poling for 100 s and 200 s. (d) Optical images of the lateral MAPbI <sub>3</sub> perovskite solar cell with a mobile PbI <sub>2</sub> thread <sup>[44]</sup> .....	7
<b>Figure 1.5</b> Current–voltage curves of perovskite solar cell, FB-SC represents forward bias to short circuit and SC-FB represents short circuit to forward bias <sup>[43]</sup> .....	8
<b>Figure 1.6</b> Illustration of the frequency dependent dielectric spectrum <sup>[57]</sup> .....	10
<b>Figure 1.7</b> The orientation state at different temperatures <sup>[59]</sup> .....	11
<b>Figure 1.8</b> (a) Scheme of the experimental devices; the arrow indicates light incident side. (b) Tetragonal perovskite, phase at room temperature. (c) Real and (d) imaginary part of dielectric permittivity as a function of frequency under dark and 1 sun illumination conditions, measured at room temperature and 0 V applied bias <sup>[61]</sup> .....	13
<b>Figure 1.9</b> The dielectric constant of the three MA-Pb-halides across a wide frequency spectrum <sup>[54]</sup> .....	14
<b>Figure 1.10</b> Scheme of the electric field induced reorganization of a distorted Ce near neighbor coordination shell containing an oxygen vacancy <sup>[79]</sup> .....	17
<b>Figure 1.11</b> Electrostrictive response of MAPbI <sub>3</sub> single crystal. (a) Schematic illustration of AFM measurement of strain induced by electric field. (b) Electrostrictive strain of a 40 μm MAPbI <sub>3</sub> single crystal under a.c. bias at 10 Hz. (c) Relation between strain and electric field for the MAPbI <sub>3</sub> single crystal. Schematic illustration of setup (e) and experimental result (f) for out-of-plane lattice deformation under in-plane electric field. Δ H is the detected thickness change by AFM <sup>[80]</sup> .....	18
<b>Figure 1.12</b> (a) Deflection versus VAC and (b) coercivity dependence with time for MAPbI <sub>3</sub> films in the dark at room temperature (RT) (black circles), under illumination (pink triangles) and in dark and at 40 °C (blue open circles) <sup>[82]</sup> .....	20

<b>Figure 1.13</b> High-resolution (a) PFM, (b) pc-AFM, (c) topography and (d) KPFM images <sup>[115]</sup> ....	24
<b>Figure 1.14</b> Transition entropy of MAPbI <sub>3</sub> <sup>[120]</sup> .....	25
<b>Figure 1.15</b> The temperature dependence of the rotation angle of the PbI <sub>6</sub> octahedron in the tetragonal phase of MAPbI <sub>3</sub> <sup>[95]</sup> .....	26
<b>Figure 1.16</b> Illustration of the major processes occurring on a semiconductor panicle following electronic excitation. Electron-hole recombination can occur at the surface (reaction (a)) or in the bulk (reaction (b)) of the semiconductor. At the surface of the panicle, photogenerated electrons can reduce an electron acceptor A (reaction (c)) and photogenerated holes can oxidize an electron donor D (reaction (d)) <sup>[134]</sup> .....	28
<b>Figure 2.1</b> Schematic representation of inverse temperature crystallization <sup>[135]</sup> .....	29
<b>Figure 2.2</b> Principle of a dielectric measurement .....	32
<b>Figure 2.3</b> Amplitude and phase relations between voltage and current of a sample for electric measurements .....	33
<b>Figure 2.4</b> The schematic diagram of hysteresis loop <sup>[136]</sup> .....	34
<b>Figure 2.5</b> Schematic of the setup for piezoresponse force microscopy <sup>[137]</sup> .....	35
<b>Figure 3.1</b> The XRD pattern with the inset of photograph of MAPbI <sub>3</sub> single crystal .....	39
<b>Figure 3.2.</b> Real part(a) and imaginary part (b) of dielectric constant as a function of frequencies recorded at various temperatures. The continuous red line corresponds to the best fits from the modified Cole-Cole equation. The inset diagram represents schematically the dielectric setup configuration .....	40
<b>Figure 3.3</b> (a) Logarithmic variation of the Debye model versus 1000/T. (b) static dielectric constant $\epsilon_s$ . (c) real part $\sigma_1$ and (d) the imaginary part $\sigma_2$ of the electrical conductivity thermally activated in MAPbI <sub>3</sub> single crystal. ....	43
<b>Figure 3.4.</b> (a)The real part and imaginary part of dielectric constant as a function of frequency recorded at 193 K with the experimental measurements represented by square symbols (black, blue) and the continuous red lines associated with the simulation model of Debye relaxation. (b) The imaginary part of dielectric constant of high frequencies recorded at different temperature.....	44
<b>Figure 3.5</b> (a) Real and (b) imaginary parts of the complex conductivity spectra at different temperatures in the frequency range 0.01 Hz–1 MHz for MAPbI <sub>3</sub> single crystal. The red solid lines are the best fits to the Eqs. (3.8) and (3.9).....	46



<b>Figure 3.6</b> Representation of $\ln(T\sigma_{dc})$ vs. $1000/T$ (a) and relaxation time $\tau_2$ . (b) in MAPbI <sub>3</sub> single crystal as deduced from dielectric spectroscopy measurements .....	48
<b>Figure 3.7</b> Dielectric constant and ac conductivity as a function of frequency at the temperature (a) 193 K and (b) 283 K.....	49
<b>Figure 3.8</b> (a) Real and (b) imaginary parts of the dielectric constant under light and dark condition, the continuous red line corresponds to the best fits from equation (3.2) .....	50
<b>Figure 3.9</b> Temperature dependence of dielectric constant of MAPbI <sub>3</sub> at different frequency .....	51
<b>Figure 3.10</b> Fitting of the MAPbI <sub>3</sub> single crystal dielectric constant to Kirkwood–Fröhlich–Onsager equation over the temperature range for the tetragonal phase .....	53
<b>Figure 3.11</b> XRD patterns of Cs <sup>+</sup> doped MAPbI <sub>3</sub> .....	54
<b>Figure 3.12</b> (a) Absorbance spectra and (b) band gap of the Cs <sup>+</sup> doped MAPbI <sub>3</sub> .....	55
<b>Figure 3.13</b> The band gap of Cs <sup>+</sup> doped MAPbI <sub>3</sub> .....	55
<b>Figure 3.14</b> Temperature dependent dielectric constant of the Cs <sup>+</sup> doped MAPbI <sub>3</sub> .....	56
<b>Figure 3.15</b> Fitting of the Cs <sup>+</sup> doped MAPbI <sub>3</sub> dielectric constant to Kirkwood–Fröhlich–Onsager equation .....	56
<b>Figure 4.1</b> Powder X-ray diffraction pattern of MAPbI <sub>3</sub> for tetragonal phase (30 °C) and cubic phase (70 °C).....	60
<b>Figure 4.2</b> (a) Color map of XRD as a function of temperature and (b) Rietveld refinements at 30 °C for MAPbI <sub>3</sub> .....	63
<b>Figure 4.3</b> Evolution of lattice parameters versus temperature .....	63
<b>Figure 4.4</b> Evolution of lattice parameters versus temperature during the cooling and heating process .....	63
<b>Figure 4.5</b> The temperature dependence of the rotation angle of the octahedra.....	65
<b>Figure 4.6</b> MAPbI <sub>3</sub> single crystal (a) XRD pattern of (100) plane at room temperature. (b) the intensity of (800) plane at different temperature .....	66
<b>Figure 4.7</b> (a) HRXRD diffractometer. (b) Illustration of the Euler angles and the angles $\Omega$ and $2\theta$ .....	66
<b>Figure 4.8</b> Diffraction intensity of (437) plane at different temperature under omega scan .....	67
<b>Figure 4.9</b> (a) A two-dimensional representation of the cubic-phase lattice. (b) A two-dimensional representation of the tetragonal-phase lattice .....	67

<b>Figure 4.10</b> Raman Spectroscopy of single crystal at different temperature.....	68
<b>Figure 5.1</b> The schematic diagram of the (a) AC poling and (b) DC poling .....	73
<b>Figure 5.2</b> (a)Laser interferometry process and the measured displacement as function of the applied voltage (b) and the excitation frequency (c) in a quartz single crystal. ....	74
<b>Figure 5.3</b> (a) Time-domain and (b) frequency-domain displacement signal under 600 V VPP for the sample .....	75
<b>Figure 5.4.</b> (a) displacement (both piezoelectricity and electrostriction), (b) displacement (filtering the displacement of piezoelectricity) of MAPbI <sub>3</sub> single crystal with a thickness of 3 mm after ac poling at 1 Hz under ac bias at 4 kHz, (c) displacement as a function of electric field due to the first-order piezoelectricity and second-order electrostriction, the inset diagram is the displacement of electrostriction as a function of the square of electric field.(d)The displacement of electrostriction as a function of frequency.....	76
<b>Figure 5.5</b> Electrostrictive strain as a function of the square electric field.....	77
<b>Figure 5.6</b> Displacement induced by piezoelectric effect as a function of the applied voltage .....	79
<b>Figure 5.7</b> Displacement induced by piezoelectric effect as a function of the applied voltage for the non-poled sample .....	79
<b>Figure 5.8</b> (a) Current-voltage curve with different frequencies for the ac poled samples, (b) dielectric constant and loss as a function of the frequency without and with (ac, dc) poling .....	81
<b>Figure 5.9</b> Scheme of the electric field induced reorganization of a distorted lattice .....	81
<b>Figure 5.10</b> (a) Electrostrictive and (b) piezoelectric effect for the samples ac poled at 1 Hz and 100 Hz.....	82
<b>Figure 5.11</b> The dielectric constant as a function of frequency for the samples ac poled at 1 Hz and 100 Hz.....	82
<b>Figure 6.1</b> (a) The XRD pattern of the pellets, (b) The XRD pattern of the film.....	86
<b>Figure 6.2</b> The P-E and I-E loops of pellets for the frequency of 10 Hz and at three different electric field (a) 0.075 kV/cm, (b) 0.15 kV/cm, (c) 1.5 kV/cm.....	87
<b>Figure 6.3</b> Dielectric constant and dielectric loss as a function of temperature at the frequency of 10 kHz 100 kHz and 1 MHz for MAPbI <sub>3</sub> pellets.....	88
<b>Figure 6.4</b> The SEM image of MAPbI <sub>3</sub> (a) top-view (b) cross-sectional SEM images .....	89
<b>Figure 6.5</b> The hysteresis loop of MAPbI <sub>3</sub> films .....	89

<b>Figure 6.6</b> AFM and PFM images of MAPbI <sub>3</sub> thin film (3×3 μm <sup>2</sup> ): (a) AFM topography, (b) PFM amplitude in plane, (c) PFM amplitude out of the plane .....	90
<b>Figure 6.7</b> Hysteresis loops of the MAPbI <sub>3</sub> single crystal. (a) P-E loops. (b) I-E loop .....	91
<b>Figure 6.8</b> (a) AFM topography, (b) PFM amplitude in plane of MAPbI <sub>3</sub> single crystal.....	91
<b>Figure 7.1</b> XRD of TiO <sub>2</sub> , MAPbI <sub>3</sub> and MAPbI <sub>3</sub> /TiO <sub>2</sub> between the 2θ range of 10-60° .....	95
<b>Figure 7.2</b> (a) UV–Vis spectra of MAPbI <sub>3</sub> , TiO <sub>2</sub> , and MAPbI <sub>3</sub> /TiO <sub>2</sub> with (b) the corresponding bandgaps.....	96
<b>Figure 7.3</b> The SEM of (a) MAPbI <sub>3</sub> and (b) 15%MAPbI <sub>3</sub> /TiO <sub>2</sub> .....	96
<b>Figure 7.4</b> The EDS of 15% MAPbI <sub>3</sub> /TiO <sub>2</sub> .....	97
<b>Figure 7.5</b> The peak position of benzyl alcohol and benzaldehyde measured by gas chromatography .....	97
<b>Figure 7.6</b> Color change of solution before (left) and after (right) catalysis with MAPbI <sub>3</sub> as catalyst .....	99
<b>Figure 7.7</b> Color change of solution before (left) and after (right) catalysis with MAPbI <sub>3</sub> /TiO <sub>2</sub> as catalyst.....	100